

Photoplethysmography-Based Biomedical Signal Processing

Vom Fachbereich 18
Elektrotechnik und Informationstechnik
der Technischen Universität Darmstadt
zur Erlangung der Würde eines
Doktor-Ingenieurs (Dr.-Ing.)
genehmigte Dissertation

von
Dipl.-Ing. Tim Schäck
geboren am 19.11.1986 in Offenbach am Main

Referent:	Prof. Dr.-Ing. Abdelhak M. Zoubir
Korreferent:	Prof. Dr. D. Robert Iskander
Korreferent:	Dr.-Ing. Michael Muma
Tag der Einreichung:	30.10.2018
Tag der mündlichen Prüfung:	21.01.2019

D 17
Darmstadt, 2019

Schäck, Tim: Photoplethysmography-Based Biomedical Signal Processing
Darmstadt, Technische Universität Darmstadt,
Jahr der Veröffentlichung der Dissertation auf TUpriints: 2019
Tag der mündlichen Prüfung: 21.01.2019

Veröffentlicht unter CC BY-NC-SA 4.0 International
<https://creativecommons.org/licenses/>

“You can, you should, and if you’re brave enough to start, you will.”

Stephen King (2000)

To my Family and Friends.

Acknowledgments

I would like to thank all the people who helped, inspired and supported me during my doctoral studies and who contributed to this thesis in various ways.

First, I would like to thank Prof. Dr.-Ing. Abdelhak Zoubir for giving me the opportunity of accomplishing my Ph.D. studies in an excellent research group. I am very grateful for his support and for the freedom he gave me for my research.

I thank Dr.-Ing. Michael Muma wholeheartedly for his supervision, about which I consider myself fortunate since my student research project in 2011. His outstanding enthusiasm and motivation helped me throughout my doctoral studies to accomplish achievements that I would not have accomplished without him. I remember especially the extraordinary time during the IEEE Signal Processing Cup 2015 together in Darmstadt and Australia. I am deeply grateful to him for all his advice and guidance.

I would like to thank Prof. Dr. D. Robert Iskander for his co-supervision and his valuable scientific comments. My gratitude goes to my examiners Prof. Dr. Thomas P. Burg and Prof. Dr.-Ing. Jürgen Adamy, as well as Prof. Dr. Heinz Koepl as the chairperson.

It was a wonderful, almost never-ending time for me in the Signal Processing Group and I am thankful for the great atmosphere, team spirit and support in any form. In particular, I thank my roommates Patricia Binder, Dr.-Ing. Gökhan Gül, Dr.-Ing. Michael Leigsnering, Ann-Kathrin Seifert and Freweyni Teklehaymanot for the countless conversations and wonderful moments we had together. I really enjoyed going to a conference or summer school with Dr.-Ing. Mouhammad Alhumaidi, Dr.-Ing. Stefano Fortunati, Dr.-Ing. Jürgen Hahn, Dr.-Ing. Khadidja Hamaidi, Di Jin, Dr.-Ing. Sahar Khawatmi, Michael Lang and Sergey Sukhanov. It was a pleasure working with Dr.-Ing. Sara Al-Sayed, Jack Dagdagan, Dr.-Ing. Christian Debes, Dr.-Ing. Nevine Demitri, Dr.-Ing. Michael Fauß, Prof. em. Dr.-Ing. Eberhard Hänsler, Dr. Roy Howard, Huiping Huang, Amare Kassaw, Dr.-Ing. Stefan Leier, Mark Leonard, Toufik Mouchini, Afief Pambudi, Dr. Ivana Perna, Prof. Dr.-Ing. Henning Puder, Dominik Reinhard, Dr.-Ing. Simon Rosenkranz, Dr.-Ing. Adrian Šošić, Dr.-Ing. Wassim Suleiman, Dr.-Ing. Fiky Suratman, Dr.-Ing. Gebremichael Teame, Dr.-Ing. Christian Weiß and Dr.-Ing. Feng Yin.

I am sincerely grateful to Renate Koschella and Hauke Fath for taking care of any administrative and technical problem. Both always had an open door to listen to my

wishes and problems. You have always been a constant for me to rely on and to ask for help or advice.

Furthermore, I sincerely want to thank the people I had the opportunity to collaborate with. Especially, I thank Yosef Safi Harb from Happitech and Dr. J.S.S.G. de Jong and Dr. Robert Riezebos from the Onze Lieve Vrouwe Gasthuis (OLVG) in Amsterdam for the constructive collaboration, joint research and for your valuable practical insights. I really enjoyed working with you in Darmstadt and in Amsterdam.

I also thank the co-authors Prof. Dr. Mengling Feng, Prof. Dr. Cuntai Guan and Dr.-Ing. Weaam Alkhalidi for their contributions to our joint research. Special thanks go to Dr.-Ing. Christian Steffens and Prof. Marius Pesavento for their contributions to our paper in the IEEE Signal Processing Magazine.

During my doctoral studies, I was happy to supervise and work with some brilliant students. My sincere thanks go to Björn Achenbach, Frederik Bous, Burak Celik, Nikola Geneshki, Lisa Hesse, Thomas Kübert, Marc Meißner, Felicia Ruppel, Christian Sledz and Sarun Thongaram.

I would also like to thank those dedicated students with whom I won the IEEE Signal Processing Cup 2015 together in Brisbane, Australia: Alaa Alameer, Bastian Alt, Maximilian Hüttenrauch, Hauke Radtke and Patrick Wenzel. Guys, you did a great job!

Special thanks go to my friends who accompanied me during my doctoral studies: Bettina Freier, Sebastian Jörg, Dennis Noll, Yvonne Späck-Leigsnering and Benjamin Surges for listening to my concerns, for your support and above all for your friendship. I would also like to thank Thorsten Kempermann for proofreading and all his useful comments.

Finally, I wish to express my gratitude to my family: my mother Heidi and her husband Bernd, my father Uwe and his wife Gabi, my sisters Carolin, Franzi, Jenny, Julia, Nele, and their partners, my niece Emilia, my cousin Martin, and my sweetheart Anna Korff. Without your unconditional love, patience and trust, this work would not have been possible.

Darmstadt, 21.01.2019

Kurzfassung

In dieser Dissertation werden biomedizinische Signalverarbeitungsverfahren auf Basis der Photoplethysmografie entwickelt und analysiert. Die entwickelten Methoden lösen Probleme der Herzratenschätzung bei körperlicher Betätigung und der Beobachtung der kardiovaskulären Gesundheit. Für die Schätzung der Herzrate während körperlicher Betätigung werden zwei verschiedene Methoden vorgestellt, die die momentane Herzrate am Handgelenk sehr genau schätzen können und gleichzeitig rechnerisch effizient in Wearables integriert werden könnten. Im Rahmen der Beobachtung der kardiovaskulären Gesundheit wird eine Methode für die Erkennung von Vorhofflimmern mit der Videokamera eines Smartphones vorgeschlagen, die eine hohe Erkennungsrate von Vorhofflimmern auf einem klinischen Vorstudien-Datensatz erzielt. Die weitere Beobachtung der kardiovaskulären Parameter beinhaltet die Schätzung von Blutdruck, Pulswellengeschwindigkeit und vaskulären Altersindex, für die ein Verfahren vorgestellt wird, das nur ein einziges photoplethysmografisches Signal benötigt.

Die Schätzung der Herzrate während einer körperlichen Betätigung mit Hilfe von photoplethysmografischen Signalen stellt einen wichtigen Forschungsschwerpunkt dieser Dissertation dar. In dieser Arbeit werden zwei effizient rechnende Algorithmen vorgestellt, die die Herzrate aus zwei photoplethysmografischen Signalen mit einem dreiachsigen Beschleunigungssensorsignal schätzen. Im ersten Algorithmus werden adaptive Filter benutzt, um die Artefakte zu schätzen, die durch die Bewegung verursacht wurden und die die Signalqualität stark beeinträchtigen. Hierzu wird der nichtstationäre Zusammenhang zwischen den gemessenen Beschleunigungen und den Artefakten als lineares System modelliert. Die Ausgänge der adaptiven Filter werden kombiniert, um die Signalqualität weiter zu verbessern. Die Herzrate wird im Spektralbereich so verfolgt, dass sie entlang der wahrscheinlichsten kontinuierlichen Linie mit hoher Energie verläuft. Der zweite Algorithmus weist eine geringe Berechnungskomplexität auf und ist im Vergleich zu anderen Ansätzen sehr schnell in der Ausführung. Er nutzt korrelationsbasierte Indikatorfunktionen und Kombinationen der Signalspektren, um das korrelierte Nutzsignal zu verbessern und unkorrelierte Störungen zu unterdrücken. Durch die zusätzliche Dämpfung harmonischer Rauschanteile werden die Auswirkungen starker Bewegungsartefakte auf die Herzratenschätzung reduziert. Das spektrale Schätzverfahren verwendet eine lineare Vorhersage mithilfe der Methode der kleinsten Quadrate. Beide Algorithmen sind sehr genügsam in der benötigten Rechenleistung. Insbesondere der zweite Algorithmus ist sehr schnell in seiner Ausführung, was an einem weitverbreiteten Vergleichsdatensatz gezeigt wird, an dem beide Algorithmen mit anderen aktuellen Methoden verglichen werden.

Der zweite Forschungsschwerpunkt und ein weiterer wichtiger Beitrag dieser Dissertation liegt in der Beobachtung der kardiovaskulären Gesundheit mittels eines einzelnen photoplethysmografischen Signals. Es werden zwei Methoden vorgestellt, von der die eine zur Erkennung von Vorhofflimmern und die andere zur Schätzung des Blutdrucks, der Pulswellengeschwindigkeit und des vaskulären Alters dient.

Die erste Methode ist in der Lage, Vorhofflimmern anhand eines Smartphones zu erkennen, das einen auf der Videokamera aufgelegten Finger filmt. Der Algorithmus wandelt das Video in ein photoplethysmografisches Signal um und extrahiert Signalmerkmale, die dann zur Unterscheidung zwischen Vorhofflimmern und einem normalen, regelmäßigen Herzschlag verwendet werden. Eine fehlerfreie Erkennung von Vorhofflimmern kann für einen klinischen Datensatz, der 326 Messungen (davon 20 mit Vorhofflimmern) enthält, bereits durch zwei Merkmale und anhand einer einfachen linearen Entscheidungsgleichung erreicht werden.

Die zweite Methode zielt darauf ab, kardiovaskuläre Parameter aus einem einzigen photoplethysmografischen Signal ohne die sonst übliche Verwendung eines zusätzlichen Elektrokardiogramms zu schätzen. Das vorgeschlagene Verfahren extrahiert eine große Anzahl von Merkmalen aus dem photoplethysmografischen Signal und seiner Differenzreihe erster und zweiter Ordnung und rekonstruiert fehlende Merkmale durch Anwendung eines „Matrix Completion“-Ansatzes. Die Schätzung kardiovaskulärer Parameter basiert auf einer nichtlinearen Erweiterung der „Support Vector Regression“ und wird mit einkanaligen photoplethysmografisch-basierten Schätzern, die lineare Regressionsmodelle nutzen, sowie einer auf der Pulsankunftszeit basierten Methode verglichen. Wenn der Trainingsdatensatz bereits die Person enthält, für die die kardiovaskulären Parameter bestimmt werden sollen, kann mit der vorgeschlagenen Methode eine akkurate Schätzung ohne weitere Kalibrierung erfolgen.

Alle vorgeschlagenen Algorithmen werden auf reale Daten angewendet, die wir entweder selbst in unserem biomedizinischen Labor erfasst haben, die von einem klinischen Forschungspartner erfasst wurden oder die als Benchmark-Datensatz frei verfügbar sind.

Abstract

In this dissertation, photoplethysmography-based biomedical signal processing methods are developed and analyzed. The developed methods solve problems concerning the estimation of the heart rate during physical activity and the monitoring of cardiovascular health. For the estimation of heart rate during physical activity, two methods are presented that are very accurate in estimating the instantaneous heart rate at the wrist and, at the same time, are computationally efficient so that they can easily be integrated into wearables. In the context of cardiovascular health monitoring, a method for the detection of atrial fibrillation using the video camera of a smartphone is proposed that achieves a high detection rate of atrial fibrillation (AF) on a clinical pre-study data set. Further monitoring of cardiovascular parameters includes the estimation of blood pressure (BP), pulse wave velocity (PWV), and vascular age index (VAI), for which an approach is presented that requires only a single photoplethysmographic (PPG) signal.

Heart rate estimation during physical activity using PPG signals constitutes an important research focus of this thesis. In this work, two computationally efficient algorithms are presented that estimate the heart rate from two PPG signals using a three axis accelerometer. In the first approach, adaptive filters are applied to estimate motion artifacts that severely deteriorate the signal quality. The non-stationary relationship between the measured acceleration signals and the artifacts is modeled as a linear system. The outputs of the adaptive filters are combined to further enhance the signal quality and a constrained heart rate tracker follows the most probable high energy continuous line in the spectral domain. The second approach is modest in computational complexity and very fast in execution compared to existing approaches. It combines correlation-based fundamental frequency indicating functions and spectral combination to enhance the correlated useful signal and suppress uncorrelated noise. Additional harmonic noise damping further reduces the impact of strong motion artifacts and a spectral tracking procedure uses a linear least squares prediction. Both approaches are modest in computational complexity and especially the second approach is very fast in execution, as it is shown on a widely used benchmark data set and compared to state-of-the-art methods.

The second research focus and a further major contribution of this thesis lies in the monitoring of the cardiovascular health with a single PPG signal. Two methods are presented, one for detection of AF and one for the estimation of BP, PWV, and VAI. The first method is able to detect AF based on a smartphone filming the finger placed on the video camera. The algorithm transforms the video into a PPG signal and extracts features which are then used to discriminate between AF and normal sinus rhythm

(NSR). Perfect detection of AF is already achieved on a data set of 326 measurements (including 20 with AF) that were taken at a clinical pre-study using an appropriate pair of features whereby a decision is formed through a simple linear decision equation. The second method aims at estimating cardiovascular parameters from a single PPG signal without the conventional use of an additional electrocardiogram (ECG). The proposed method extracts a large number of features from the PPG signal and its first and second order difference series, and reconstructs missing features by the use of matrix completion. The estimation of cardiovascular parameters is based on a nonlinear support vector regression (SVR) estimator and compared to single channel PPG based estimators using a linear regression model and a pulse arrival time (PAT) based method. If the training data set contains the person for whom the cardiovascular parameters are to be determined, the proposed method can provide an accurate estimate without further calibration.

All proposed algorithms are applied to real data that we have either recorded ourselves in our biomedical laboratory, that have been recorded by a clinical research partner, or that are freely available as benchmark data sets.

Contents

1	Introduction	1
1.1	Motivation	1
1.2	Aims of this Doctoral Project	2
1.3	Summary of the Contributions	2
1.3.1	Heart Rate Estimation During Physical Activity	3
1.3.2	Cardiovascular Health Monitoring	3
1.4	Publications	4
1.4.1	Photoplethysmography-Related Publications	4
1.4.2	Other Publications	5
1.5	Organization of the Thesis	6
2	Photoplethysmographic Signals	9
2.1	Preliminaries	9
2.1.1	Signal	9
2.1.2	Relation to Electrocardiography	10
2.2	Areas of Application	11
2.3	Acquisition	12
2.3.1	Sensor Systems of the Experimental Data	14
2.4	Signal Model	15
2.4.1	Signal Segmentation and Difference Series	15
2.5	Summary	18
3	Heart Rate Estimation During Physical Activity	19
3.1	Introduction and Motivation	19
3.2	State of the Art	22
3.3	Contributions	24
3.4	Adaptive Filter Based Heart Rate Estimation	25
3.4.1	Preprocessing	25
3.4.2	Noise Reduction by Adaptive Filtering	25
3.4.3	Signal Enhancement by Combination	27
3.4.4	Heart Rate Tracking	28
3.5	Computationally Efficient Heart Rate Estimation	29
3.5.1	Preprocessing	29
3.5.2	Signal Enhancement by Sample Correlation Functions	30
3.5.3	Fourier Transformation	30
3.5.4	Harmonic Noise Damping	31
3.5.5	Heart Rate Tracking	31

3.6	Experimental Results	32
3.6.1	Real Data Set	32
3.6.2	Evaluation Metrics	33
3.6.3	Heart Rate Estimation Accuracy	33
3.6.4	Computational Complexity	34
3.7	Discussion	39
3.8	Summary and Conclusions	40
4	Cardiovascular Health Monitoring	41
4.1	Introduction	42
4.2	Contributions	43
4.3	State of the Art	43
4.4	Atrial Fibrillation Detection	45
4.4.1	PPG Signal Acquisition and Preprocessing	45
4.4.2	Statistical Feature Extraction	46
4.4.2.1	Time-Domain Features	47
4.4.2.2	Frequency-Domain Features	49
4.4.2.3	Acceleration Features	50
4.4.3	Feature Selection and Classification	51
4.4.3.1	Sequential Forward Selection (SFS)	51
4.4.3.2	Support Vector Machine (SVM)	52
4.4.4	Real Data Results	52
4.4.4.1	Experimental Setup and Performance Metrics	52
4.4.4.2	Classification Results	53
4.4.5	Discussion	54
4.5	Estimation of Blood Pressure and Arterial Stiffness	56
4.5.1	Preprocessing	56
4.5.2	Feature Extraction	57
4.5.2.1	Features from the PPG Waveform	57
4.5.2.2	Features from the VPG Waveform	60
4.5.2.3	Features from the APG Waveform	60
4.5.3	Feature Matrix Completion	60
4.5.4	Cardiovascular Parameter Estimation	62
4.5.4.1	Least Squares Linear Regression	63
4.5.4.2	Robust Linear Regression	63
4.5.4.3	Support Vector Regression (SVR) with Linear Kernel	64
4.5.4.4	Support Vector Regression (SVR) with Nonlinear Kernel	65
4.5.5	Experimental Results	66
4.5.5.1	Subjects	66

4.5.5.2	Study Protocol	67
4.5.5.3	Evaluation Metrics	69
4.5.5.4	Feature Selection	70
4.5.5.5	Comparison between Feature Extraction Methods . . .	70
4.5.5.6	Static Parameter Estimation	71
4.5.5.7	Continuous Parameter Estimation	72
4.5.5.8	Training the Regression Model	73
4.5.6	Discussion	75
4.6	Summary and Conclusions	79
5	Conclusions and Future Work	83
5.1	Conclusions	84
5.1.1	Heart Rate Estimation	84
5.1.2	Cardiovascular Health Monitoring	84
5.2	Challenges and Future Work	85
5.2.1	Heart Rate Estimation	85
5.2.2	Cardiovascular Health Monitoring	86
	Appendix	89
A.1	Summaries of Other Publications	89
A.1.1	Robust Nonlinear Causality Analysis	89
A.1.1.1	State of the Art	89
A.1.1.2	Contributions	91
A.1.2	Eyelid Localization in Videokeratoscopic Images	91
A.1.2.1	State of the Art	93
A.1.2.2	Contributions	94
A.1.3	Signal Processing Projects at TU Darmstadt	94
A.1.3.1	Contributions	95
	List of Acronyms	97
	List of Symbols	103
	References	106
	Curriculum Vitae	121

Chapter 1

Introduction

This chapter gives an introduction to the topic of this thesis, states our research aims, summarizes our original contributions, lists the publications that have been produced during the period of doctoral candidacy, and gives an overview of the structure of this thesis.

1.1 Motivation

With the advent of wearables, which are electronics that can be worn on the body, such as smartwatches, fitness wristbands, or data glasses, health monitoring has become increasingly popular in the recent years. While in 2014 only 28.8 million wearables were sold worldwide, sales rose up to 115.5 million wearables in 2017 and are expected to exceed the 200 million mark for the first time in 2020 [1]. A huge market has grown, especially in the sports sector, where the consumer can choose a suitable product from a large number of devices. In addition to communicative benefits, wearables enable the wearer to track training progress, observe health conditions, and gain new insights into physical condition. But also in the area of smartphones there are more and more apps that aim at being beneficial to the health of the user, for example by motivating to walk more steps that are counted by the inbuilt pedometer.

The use of wearables is also becoming increasingly popular in the health sector. To give a recent example, many German health insurances offer the possibility of having the steps counted with a wearable or smartphone credited to bonus points in their bonus plans. These in turn can be exchanged for monetary or other rewards. And yet, these non-medical devices often fall short of identifying actionable health insights, although their sensors would be able to, and algorithms already exist to detect cardiac arrhythmias, sleep disorders, or other risk factors. For example, an accelerated heart rate can be a sign of an imminent heart attack and an irregular heartbeat can indicate a variety of concerning conditions.

Almost all health and fitness companies use optical sensors in their wearable devices for non-invasive measurements of fitness parameters. These optical sensors use the principle of photoplethysmography, which has become the standard for portable heart

rate sensors and which is able to replace uncomfortable electrocardiogram (ECG) chest straps for many physical activities. In contrast to ECG, which is typically measured by multiple electrodes at the chest, a photoplethysmographic (PPG) sensor can be placed at a single site on the body with good blood circulation, such as the earlobe, fingertip, or wrist, making it easy to wear and collect measurement data throughout the day. In addition, a PPG sensor can be cost-effectively integrated into a wearable, and any video camera of a smartphone can be transformed into a PPG sensor.

In summary, photoplethysmography has great potential to provide new health insights, to measure additional physiological parameters of the body, and to reveal health risks that have not yet been observed. However, further research on the algorithms is needed to improve the accuracy and reliability of the measurements and to develop new estimation methods for further physiological parameters.

1.2 Aims of this Doctoral Project

The aim of this doctoral project is to introduce photoplethysmography-based methods to solve current biomedical signal processing problems. The major research objectives which have been identified as highly relevant to the biomedical signal processing community and are therefore addressed in this project concern

- the estimation of heart rate during physical activity using multiple PPG and three-channel acceleration signals at the wrist with high accuracy, low computational complexity, and low memory requirements,
- the detection of atrial fibrillation (AF) using the PPG signal recorded from a video camera of a smartphone with high reliability and low computational complexity,
- and the estimation of blood pressure (BP), pulse wave velocity (PWV), and vascular age index (VAI) from a single PPG signal.

1.3 Summary of the Contributions

The original contributions of this doctoral thesis are as follows.

1.3.1 Heart Rate Estimation During Physical Activity

An adaptive filter based framework for efficient estimation of a person's heart rate using PPG and acceleration signals is presented. The original contributions in the context of this framework are constituted by:

- the development of a motion artifact suppression in PPG signals by use of adaptive normalized least mean squares (NLMS) filters and acceleration signals,
- the development of a signal enhancement method in the frequency domain,
- and the development of a constrained spectrogram-based heart rate tracker.

As the computational power and memory size of wearables are limited, a second, computationally efficient framework for accurate heart rate estimation is presented that is designed to be implemented on wearables. The original contributions in the context of this framework are constituted by:

- the development of a correlation-based method to enhance periodic components and suppress wideband noise that is caused by motion-induced artifacts or sensor and amplifier noise,
- the development of a Gaussian bandstop filter based method to damp harmonic noise,
- and the development of a constrained frequency-domain-based heart rate tracker using linear prediction.

1.3.2 Cardiovascular Health Monitoring

A photoplethysmography-based algorithm for the reliable detection of AF using smart-phones is presented that has low computational cost and low memory requirements. Our original contributions in the context of this research area are summarized as follows:

- the development of an enhanced PPG signal acquisition procedure for smart-phones,

- the exploration and extraction of new statistical discriminating features in the time and frequency domain for AF,
- and the development of a classification procedure that selects the most significant features for AF detection and that yields a simple classification equation for the discrimination between AF and normal sinus rhythm (NSR).

For monitoring a person's cardiovascular health, a framework for the estimation of BP, PWV, and VAI from a single PPG signal is proposed. The original contributions in the context of this framework are constituted by:

- the development of signal processing methods for extracting a large set of features from a PPG signal,
- the application of a matrix completion method for the recovery of missing feature values to ensure continuous estimation,
- the application of feature selection methods and the identification of features that are particularly significant for the estimation of cardiovascular parameters,
- the conduct of a study to monitor BP, PWV, and VAI with 18 persons and 42 measurements,
- the fitting of a nonlinear regression model and the comparison with linear and robust linear regression models to estimate cardiovascular parameters from a PPG signal.

1.4 Publications

The period of doctoral candidacy has culminated in the following publications.

1.4.1 Photoplethysmography-Related Publications

The following publications have been produced during the period of doctoral candidacy on photoplethysmography.

Internationally Refereed Journal Articles:

- T. Schäck, M. Muma, and A. M. Zoubir, “Estimation of blood pressure, pulse wave velocity and vascular age index from a single PPG signal”, submitted to *IEEE Journal of Biomedical and Health Informatics*.

Internationally Refereed Conference Papers:

- T. Schäck, M. Muma, and A. M. Zoubir, “Computationally efficient heart rate estimation during physical exercise using photoplethysmographic signals”, in *Proceedings of the 25th European Signal Processing Conference (EUSIPCO)*, Aug. 2017, pp. 2478–2481, in Kos, Greece.
- T. Schäck, Y. Safi Harb, M. Muma, and A. M. Zoubir, “Computationally efficient algorithm for photoplethysmography-based atrial fibrillation detection using smartphones”, in *Proceedings of the 39th Annual International Conference of the IEEE Engineering in Medicine and Biology Society (EMBC)*, July 2017, pp. 104–108, on Jeju Island, Korea.
- T. Schäck, M. Muma, and A. M. Zoubir, “A new method for heart rate monitoring during physical exercise using photoplethysmographic signals”, in *Proceedings of the European Signal Processing Conference (EUSIPCO)*, Sept. 2015, pp. 2666–2670, in Nice, France.

Patents:

- T. Schäck, M. Muma, A. M. Zoubir, R. Lizio, and S. Liébana Viñas, “Methods to estimate the blood pressure and the arterial stiffness based on photoplethysmographic (PPG) signals”, submitted to the *European Patent Office*.
- R. Lizio, S. Liébana Viñas, T. Schäck, M. Muma, and A. M. Zoubir, “Preparations containing anthocyanins for use in the influence of cardiovascular conditions”, submitted to the *European Patent Office*.

1.4.2 Other Publications

The following publications have been produced during the period of doctoral candidacy on other topics. Summaries of these publications can be found in Appendix A.1.

Internationally Refereed Journal Articles:

- T. Schäck, M. Muma, M. Feng, C. Guan and A. M. Zoubir, “Robust nonlinear causality analysis of nonstationary multivariate physiological time series”, *IEEE Transactions on Biomedical Engineering*, vol. 65, no. 6, pp. 1213–1225, June 2018.
- T. Schäck, M. Muma and A. M. Zoubir, “Signal processing projects at Technische Universität Darmstadt: How to engage undergraduate students in signal processing practice”, *IEEE Signal Processing Magazine*, vol. 34, no. 1, pp. 16–30, Jan. 2017.
- T. Schäck, M. Muma, W. Alkhaldi and A. M. Zoubir, “A procedure to locate the eyelid position in noisy videokeratoscopic images”, *EURASIP Journal on Advances in Signal Processing: Nonlinear Signal and Image Processing - A Special Issue in Honour of Giovanni L. Sicuranza on his Seventy-Fifth Birthday*, vol. 2016, no. 1, pp. 136 (13 pages), Dez. 2016.

Internationally Refereed Conference Papers:

- T. Schäck, M. Muma, and A. M. Zoubir, “Hands-on in signal processing education at Technische Universität Darmstadt”, in *Proceedings of the IEEE International Conference on Acoustics, Speech and Signal Processing (ICASSP)*, Apr. 2018, pp. 7011–7015, in Calgary, Canada.

1.5 Organization of the Thesis

Following this introduction, the thesis is structured as follows:

Chapter 2 introduces the basic concept of photoplethysmography, describes the characteristics of PPG signals and the relation to electrocardiography. The areas of applications as well as the acquisition of PPG signals and the applied sensor systems in this thesis are detailed. This chapter also introduces the notation that is used throughout this thesis.

In **Chapter 3**, two developed frameworks for heart rate estimation during physical activity using PPG and acceleration signals are introduced. First, an adaptive filter based approach is presented that reduces the impact of motion artifacts on the PPG signal and enhances the signal through a combination step before a tracker that takes

physical constraints into account estimates the heart rate. The second framework emphasizes computationally efficient heart rate estimation using basic signal processing operations only. Signal enhancement is performed by applying sample correlation functions as fundamental frequency indicators. Spectral noise damping using a Gaussian bandstop filter exploits information of the accelerometer spectrum. A simple linear least squares based tracking approach recursively estimates the heart rate. Experimental results obtained on a real-data benchmark data set confirm the performance of the developed approaches.

Chapter 4 is dedicated to cardiovascular health monitoring and presents two methods using PPG signals. First, a detection algorithm for AF using commercial off-the-shelf smartphones with a video camera is developed. For this, an intelligent acquisition method to extract a PPG signal from a smartphone video is described. Sequential feature selection is applied to find the best feature combination that discriminates between AF and NSR, using support vector machines (SVMs) as the classification algorithm. The experimental results on real-data that was recorded at a hospital in Amsterdam validate the performance of the presented method. Further, this chapter introduces a method for the estimation of BP, PWV, and VAI based on a single PPG signal. A set of 83 features is extracted from the PPG signal and its first and second order difference series. The estimation of cardiovascular parameters is performed by nonlinear support vector regression (SVR) and compared to different linear regression estimators, including a state-of-the-art method. The proposed method is evaluated on a self-recorded real data set.

Finally, in **Chapter 5**, conclusions are drawn and an outlook for future work is presented.

Chapter 2

Photoplethysmographic Signals

The purpose of this chapter is to introduce the basic concept of photoplethysmography and the notations that are used throughout the dissertation.

2.1 Preliminaries

Photoplethysmography refers to an almost 150 years old optical, noninvasive indirect measurement of blood flow changes in the microvascular bed of the tissue. The word plethysmograph is a combination of two ancient Greek words 'plethysmos', which means increase, and 'graph', which is the word for write [2]. The sensor system consists of a light source, that illuminates the skin along with underlying blood vessels via light-emitting diodes (LEDs), and a light detector to measure intensity changes of the reflected or transmitted light that is absorbed by a photo diode. The changes in light intensity are associated with variations in blood flow of the tissue and can provide information on the cardiovascular system. The light that travels through biological tissue can be absorbed by the skin, bone, and arterial or venous blood. Most changes in blood flow occur mainly in the arteries and arterioles, as they are responsible for the transport of oxygen-rich blood and nutrients.

2.1.1 Signal

The photoplethysmographic (PPG) waveform consists of a slowly varying trend, the low frequency (LF) component, which depends on the structure of the tissue, the average blood volume and the arterial blood oxygen saturation (SpO_2), and a pulsatile high frequency (HF) component, which indicates blood volume changes that occur between the systolic and diastolic phases of the cardiac cycle [3]. While the LF component slowly varies with respiration and provides information about the respiration rate, the fundamental frequency of the HF component is directly related to the heart rate, see Fig. 2.1.

The pulsatile HF component is commonly divided into two phases: the systolic phase with the systolic (direct) wave and the diastolic phase with the diastolic (reflected)

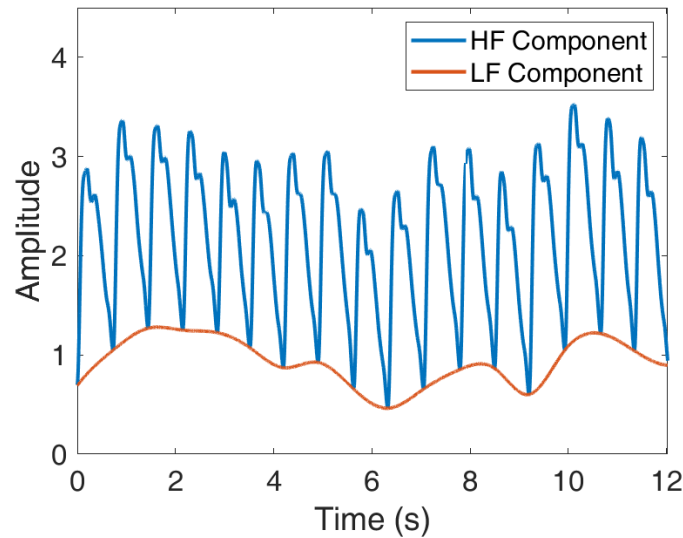


Figure 2.1. An example of a PPG signal consisting of a LF and a HF component.

wave [4], see Fig. 2.2. The diastolic wave is formed as a result of pressure transmission along a direct path from the aortic root to the measurement location, e.g. a finger. The diastolic wave is created by wave reflections from the periphery.

2.1.2 Relation to Electrocardiography

Photoplethysmography is directly related to electrocardiography which measures the electrical activity of the heart by using electrodes placed on the skin. The electrical signals can be measured using two or more electrodes placed in various positions on the chest resulting in the electrocardiogram (ECG). The most prominent feature of the ECG is the QRS complex, which indicates the main pumping contractions of the heart. Within the QRS complex, the most prominent component is the R-peak, which is typically used to estimate the heart rate by calculating the time difference between consecutive heartbeats. With each contraction of the heart, blood is pumped through the body and blood flow changes can be measured by the PPG sensor. There is a time difference between the contraction of the heart and the onset of PPG waveform, the so-called pulse arrival time (PAT), see Fig. 2.3. Commonly, the PAT is calculated by the time difference between the R-peak of the QRS complex and the onset of the systolic wave of the PPG signal. In this case, the PAT is a combination of the pulse transit time (PTT), which describes the time a pressure wave takes to travel between two arterial sites, and the pre-ejection period (PEP), which is the time between the

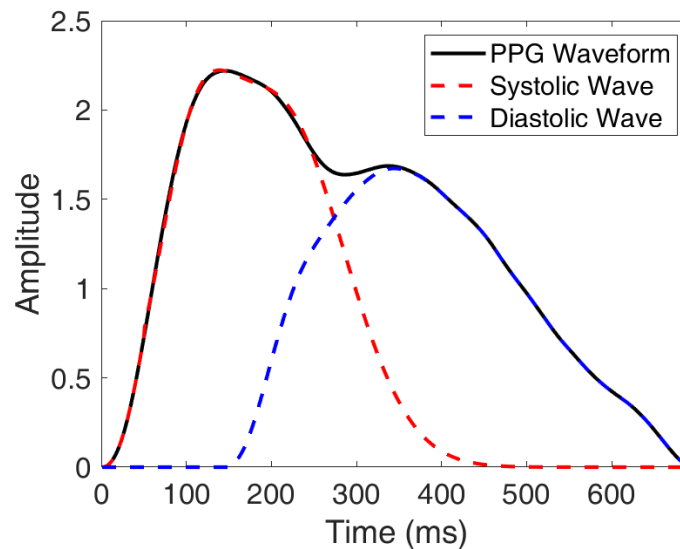


Figure 2.2. A PPG waveform which is separated into two phases: the systolic phase with the systolic (direct) wave and the diastolic phase with the diastolic (reflected) wave.

beginning of electrical stimulation of the left ventricle and the opening of the aortic valve.

2.2 Areas of Application

Photoplethysmography has been applied for decades in many different clinical areas, for example in clinical physiological monitoring to measure heart rate, SpO_2 , blood pressure, cardiac output, and respiration, but also for vascular assessment, i.e. arterial disease or venous assessment [5]. Especially pulse oximetry, which uses photoplethysmography to measure the SpO_2 and heart rate, is said to represent one of the most significant technological advances in clinical patient monitoring over the last few decades [6] and became a mandated international standard for monitoring during anaesthesia in the early 1990s.

Due to the increasingly large number of wearables, such as fitness trackers or smartwatches, heart rate estimation in particular is more and more used in non-medical areas, for example by athletes to replace a bothersome ECG chest strap. The main advantage of a fitness tracker or a smartwatch is the possibility to permanently record measurements that can provide new health-related insights.

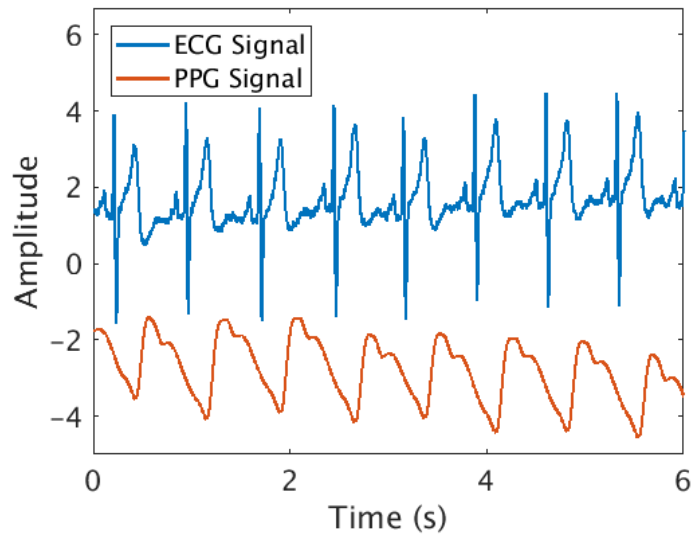


Figure 2.3. An example of a synchronously recorded ECG and PPG signal.

The largest number of PPG sensors can, however, be found in your pocket or hand-bag: your smartphone. By placing the forefinger on the video camera and using its flash, a smartphone can easily be transformed into a PPG sensor. A variety of applications already exist that can estimate heart rate, heart rate variability, or even detect arrhythmia [7–12].

2.3 Acquisition

A PPG sensor consists of a light source and a light detector, also called photodetector (PD) or photosensor. The light source illuminates the tissue of the skin and is typically realized by an LED. The PD receives the spectrum and intensity of the reflected or transmitted light and additional stray light that incides on the sensor from the environment. A PD is typically realized by a photodiode, but can also be a mobile phone camera.

There are basically two operating modes of a PPG sensor: the reflectance mode, in which the light source and the detector are side by side, and the transmission mode, in which the tissue is between the two components. The use of the transmission mode is naturally limited to a few body parts, e.g. fingers or earlobes. Fig. 2.4 shows both operating modes on a finger.

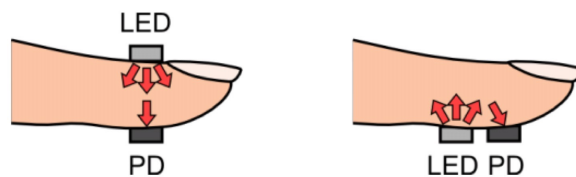


Figure 2.4. Two basic operating modes: The PD detects the transmitted light from the LED in the transmission mode (left) and in the reflectance mode (right), the PD receives the light that is back-scattered from the tissue, bone, or blood vessels. The image was taken from [3].

For the light source of a PPG sensor, the choice of the wavelength of the LED is important. Anderson and Parrish examined the optical characteristics and the penetration depth of light in human skin [13]. Melanin is the major absorber of radiation in the epidermis, especially at shorter wavelengths in the ultraviolet (UV) range with a wavelength of less than 300 nm. In this range also epidermal thickness and several acids are important factors. The strongest absorption corresponds to the blue region (400–500 nm).

As an optical “window” exists in skin and most other soft tissue in the red and near infrared (IR) region between 600–1300 nm, LEDs with near IR wavelengths have been used as a light source in PPG sensors, especially in medical devices. The penetration depth of near IR light with, for example, 1000 nm wavelength corresponds to approximately 1600 μm , making the sensor able to examine larger tissue beds located at a lower levels in the body and to obtain more biometric information, such as, hydration, muscle saturation, hemoglobin, etc. Red light is also much less affected by skin color differences, tattoos, freckle patterns, or other physiological variations compared to green light. However, red light PPG sensors are more susceptible to motion artifacts and require advanced and robust signal processing to achieve a high signal-to-noise ratio (SNR) [14].

In contrast, green light with a wavelength of 560 nm, for example, can only penetrate to a depth of about 420 μm and only examine the superficial blood vessels, which can lead to significant problems near the wrist, where blood circulation is limited. Although they do not penetrate deep, PPG sensors with green LEDs have a higher SNR and better resistance to motion artifacts. Many manufacturers of photoplethysmography-based fitness devices use green LEDs because this choice requires less signal processing and there is a wealth of knowledge from existing products to build on. For monitoring the heart rate in the daily life, green LEDs are most suitable, but for further bio-

metric information extraction, such as SpO_2 , deeper penetrating red or IR LEDs are recommended.

2.3.1 Sensor Systems of the Experimental Data

Our experimental data for Chapter 3 was initially provided by [15]. The data sets are also the training sets of the Institute of Electrical and Electronics Engineers (IEEE) Signal Processing Cup 2015. The two-channel PPG signal was recorded from the subject's wrist using a pulse oximeter with green LEDs (wavelength: 515 nm).

In Chapter 4, the experimental data for atrial fibrillation (AF) detection was recorded using the video cameras of an iPhone 5s, iPhone 6 Plus, and iPhone 6s Plus as a PD. The forefinger was placed on the mobile phone camera in such a way that it completely covered the camera image. Then, the white camera flash LED light acts as a light source and illuminates the finger. Only the red channel of each video frame was considered in the generation of the PPG signal.

For the estimation of cardiovascular parameters in Chapter 4, we recorded our own PPG data using the IR Plethysmograph Finger Clip and IR Plethysmograph Velcro Strap from ADInstruments with a wavelength of 950 nm, see Fig. 2.5.



Figure 2.5. The IR Plethysmograph Finger Clip from ADInstruments with a wavelength of 950 nm that has been used for PPG data collection in our biomedical laboratory.

2.4 Signal Model

We propose the following measurement model to describe a PPG signal:

$$p(n) = s(n) + m(n) + v(n). \quad (2.1)$$

Here, $p(n)$ is the measured PPG signal, $s(n)$ is the original non-stationary PPG signal without motion artifacts which is sought for, $m(n)$ is the non-stationary motion artifact signal and $v(n) \sim \mathcal{N}(0, \sigma^2)$ represents the sensor and amplifier noise.

We model the effects of the motion artifacts $m(n)$ in dependence of the measured three-channel acceleration signal vector $\mathbf{a}(n)$ by introducing a time-varying system with impulse response $h(n, \alpha_{\text{acc}}, \omega, \psi)$ and rewrite the model using vector-matrix notation:

$$p(n) = s(n) + \mathbf{h}^\top(n, \alpha_{\text{acc}}, \omega, \psi)\mathbf{a}(n) + v(n). \quad (2.2)$$

The impulse response $\mathbf{h}(n, \alpha_{\text{acc}}, \omega, \psi)$ is assumed to be non-stationary, i.e., it depends on the time index n . Additionally, it also depends on the variable α_{acc} , which is the acceleration that acts on the sensor, the angular velocity for rotational movements ω , and the actual position of the sensor ψ .

As in practice the angular velocity ω and the actual position ψ is not always available, we restrict the model for the impulse response to the acceleration α_{acc} . Hence, the system model equation simplifies to

$$p(n) = s(n) + \mathbf{h}^\top(n, \alpha_{\text{acc}})\mathbf{a}(n) + v(n). \quad (2.3)$$

2.4.1 Signal Segmentation and Difference Series

Let

$$\mathbf{p} = [p(1), p(2), \dots, p(N_{\text{ppg}})] \quad (2.4)$$

denote the measurement vector, where N_{ppg} is the length of the PPG signal.

Frequency-domain analysis of the PPG signal, as required in the feature extraction step that is detailed in Section 4.4.2.2, requires dividing the PPG signal into segments of fixed length N_{seg} , i.e.,

$$\mathbf{p}_m^{\text{seg}} = [p_m^{\text{seg}}(1), \dots, p_m^{\text{seg}}(N_{\text{seg}})]^\top, \quad m = 1, \dots, M_{\text{seg}}, \quad (2.5)$$

where m is the segment index, M_{seg} is the total number of segments and $p_m^{\text{seg}}(i)$ is the i -th sample of the m -th segment of the PPG signal.

PPG signals may also be segmented into segments of unequal length that are associated to the cardiac cycles. For example, as detailed in Section 4.5, feature extraction for cardiovascular parameter estimation is based on analyzing individual heartbeat signals.

Therefore, we divide \mathbf{p} into N_{beat} waveforms that are associated with the individual heartbeats, i.e.,

$$\mathbf{p} = \{\mathbf{p}_1, \mathbf{p}_2, \dots, \mathbf{p}_{N_{\text{beat}}}\}, \quad (2.6)$$

where each heartbeat

$$\mathbf{p}_n = [p_n(1), p_n(2), \dots, p_n(l_n)]^\top, \quad n = 1, \dots, N_{\text{beat}}, \quad (2.7)$$

contains l_n samples. As exemplarily shown in Fig. 2.6, the most prominent point in the PPG signal is the systolic notch which is also equal to the starting point of a heartbeat or the onset wave.

To find the systolic notches, we apply a simple search algorithm that finds prominent minima, subject to the condition that subsequent systolic notches have a minimal distance of 500 ms, as we do not expect resting heart rates to exceed 120 beats per minute (BPM). With

$$m_n = \frac{p_{n+1}(1) - p_n(1)}{l_n} \quad (2.8)$$

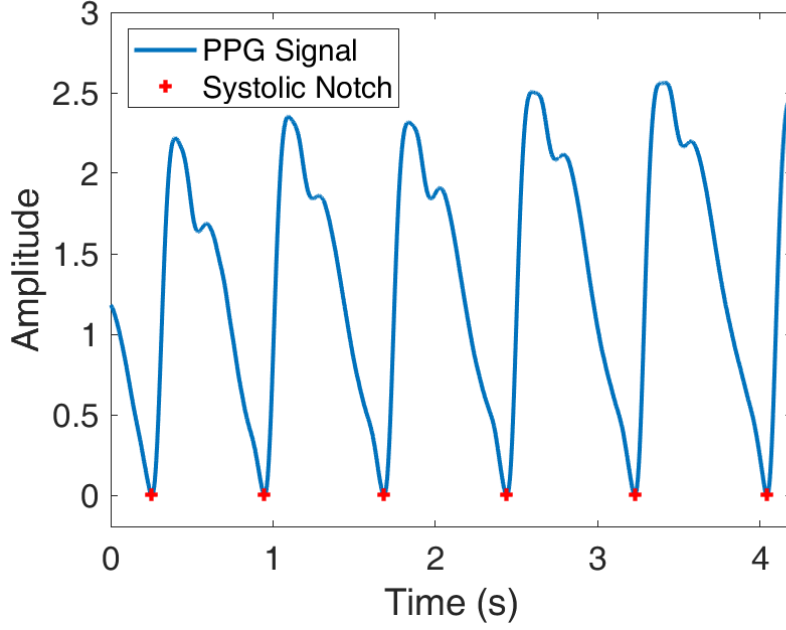


Figure 2.6. A PPG signal which is separated into individual heartbeats by the systolic notch.

denoting the slope between two subsequent systolic notches, we then subtract a line with slope m_n and intercept $p_n(1)$ for each heartbeat $n = 1, \dots, N_{\text{beat}} - 1$ of the PPG signal. An example is shown in Fig. 2.6.

Based on (2.7), we calculate the first and second order difference series of the PPG signal. The first order difference series of the PPG waveforms represents the velocity of the blood flow and is abbreviated as velocity of PPG (VPG) [4]. The VPG waveforms that are associated with the individual heartbeats are computed as

$$\mathbf{p}'_n = [p'_n(1), p'_n(2), \dots, p'_n(l_n - 1)]^\top, \quad n = 1, \dots, N_{\text{beat}}, \quad (2.9)$$

where $p'_n(i) = p_n(i + 1) - p_n(i)$.

The second order difference series of the PPG waveforms represents the acceleration of blood flow and is denoted as acceleration plethysmogram (APG)

$$\mathbf{p}''_n = [p''_n(1), p''_n(2), \dots, p''_n(l_n - 2)]^\top, \quad n = 1, \dots, N_{\text{beat}}, \quad (2.10)$$

where $p''_n(i) = p'_n(i + 1) - p'_n(i)$.

2.5 Summary

This chapter has introduced the concept of PPG signals. The characteristics of the PPG signal have been presented and the PPG waveform has been discussed. Subsequently, this chapter has highlighted possible areas of application and has reviewed the acquisition of PPG signals, including the physical setup of PPG sensors and the sensor systems used in this thesis.

Finally, the signal model and notation of PPG signals has been presented. In this context, the segmentation of the PPG signal and the calculation of difference series of the PPG signal has been described, which are necessary for the proposed algorithms in the subsequent chapters.

Chapter 3

Heart Rate Estimation During Physical Activity

In this chapter, we investigate two algorithms for heart rate estimation during physical activity using PPG signals obtained from wrist-worn optical heart rate monitors such as the ones described in Section 2.3.

We give an introduction into heart rate estimation during physical activity using PPG signals and motivate the proposed approaches in Section 3.1. An overview of the state of the art in heart rate estimation using PPG signals is given in Section 3.2. Our contributions are highlighted in Section 3.3. We provide two heart rate estimation algorithms using PPG signals in Section 3.4 and Section 3.5. In Section 3.6, we show the performance of the proposed methods and provide real data results. We summarize and conclude this chapter in Section 3.8.

The main contributions in this chapter have been published in [16, 17].

3.1 Introduction and Motivation

With the growing interest and the associated need for health and fitness, there is an increasing trend to monitor heart rate to avoid heart problems, to monitor physiological conditions during daily activities, and to control the training load during physical exercises, as heart rate is an important index for evaluating training intensity. A superelevated heart rate could indicate an excessive training load and as a consequence an associated health hazard. Therefore, it is important to continuously monitor the heart rate during physical activity in order to optimally adjust the training intensity to individual needs.

On the emerging market of wearable devices for healthcare and fitness, it is becoming common practice to monitor the user's heart rate with the help of photoplethysmography. Unlike conventional ECG-based heart rate monitors, which require multiple electrodes attached to the body to capture electrical signals, usually achieved by wearing an additional and inconvenient chest strap, depicted in Fig. 3.1, photoplethysmography can easily be recorded with wrist worn devices, see Fig. 3.2 for an exemplary



Figure 3.1. An ECG chest belt [18] which can be used to monitor the heart rate during physical activity.



Figure 3.2. A commercially available heart rate tracker [19] from 2015 with a photoplethysmography-based optical heart rate sensor and three green LEDs.

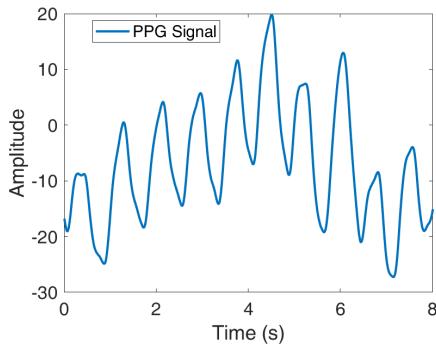


Figure 3.3. An example of a clean PPG signal. Slow variations in the baseline are due to respiration.

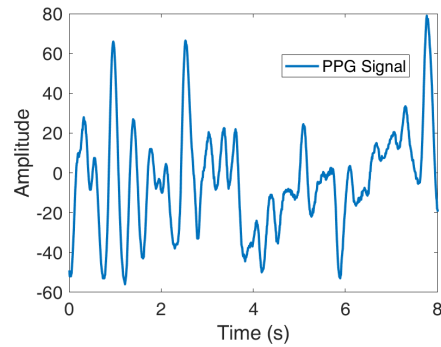


Figure 3.4. An example of a deteriorated PPG signal with motion artifacts while running on a treadmill.

commercially available fitness tracker. Optical heart rate monitors benefit from simpler hardware implementation and lower costs compared to ECG based devices. Due to their higher usability and use in modern portable devices such as smartwatches and fitness wristbands, optical heart rate monitors are widely used.

However, photoplethysmography-based heart rate estimation is challenging, especially during intense physical exercise, as the PPG measurement is susceptible to motion artifacts, which inevitably occur during physical exercises. Depending on the type of physical activity of the user, motion-induced artifacts can strongly deteriorate the quality of a PPG signal, e.g., the arm movements while running can cause strong periodic components that overlap with the desired heartbeat related PPG component. Fig. 3.3 shows a clean PPG signal and Fig. 3.4 shows a deteriorated PPG signal with motion artifacts while running on a treadmill, both recordings are 8 s long.

In the following, some challenging scenarios for heart rate estimation from motion-corrupted PPG signals are described: First, intensive hand movements (e.g. while running) change the distance between wrist and pulse oximeter so that the measured intensity of the PPG signal varies. This variation is often correlated with the frequency of hand movements. In addition, due to extensive movements, the sensors can sometimes be so far away from the skin that there is no peak corresponding to the heart rate in the frequency domain. For some cases, when the frequency of the motion artifact is close to the frequency of the heart rate, both can no longer be distinguished for a given frequency resolution. Increasing the data length would not avoid the problem, as this would require the heart rate to be stationary for a longer period of time, which is rarely the case in practice. In addition, even harmonics and subharmonics of periodic motion artifacts can mask the heart rate in the frequency domain. Another challenge is that intense movements such as boxing or jumping can cause so much acceleration

in the blood in the arteries that even the correct intensity in the PPG signal might not correspond to actual heart rate.

Most heart rate estimation algorithms take also the acceleration information into account in order to obtain information on the type and intensity of the movement and thus to draw conclusions about the motion artifacts. Also, the important *a priori* information that the actual heart rate cannot show any sudden discontinuity for healthy subjects helps to develop a useful tracking mechanism. However, if a motion artifact peak in the frequency domain is close to the heart rate peak and has a high intensity, the tracking mechanism could erroneously follow the motion artifact peak and lead to large estimation errors, even if the intensity of the heart rate peak increases again over time.

Thus, signal processing techniques are required to remove motion artifacts and noise from the PPG signal prior to estimating the heart rate.

3.2 State of the Art

The basic steps involved in heart rate estimation using PPG signals and the accelerometer information is shown in the block diagram in Fig. 3.5. Typically, the PPG and acceleration signals are preprocessed, i.e., band-pass filtered and downsampled to the desired frequency range. Motion artifact removal methods are applied to clean the signals from motion-induced artifacts and enhance the signal quality before a spectral peak tracker looks for the heart rate component in the frequency domain and outputs the estimated heart rate.

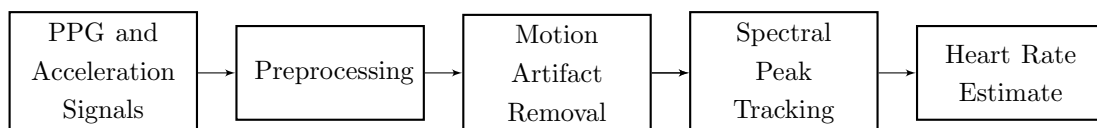


Figure 3.5. Basic steps for heart rate estimation algorithms using PPG and accelerometer signals.

In recent years, numerous techniques have been proposed to estimate the heart rate from PPG signals. However, some of these methods [20–26] do not consider strong motion of the subjects or the PPG sensors were placed at the finger ring or forehead and not at the wearer’s wrist, and thus, are not suited for heart rate estimation during

physical activity. Among the algorithms that can also handle motion artifacts, there are various approaches to clean PPG signals from motion artifacts or to reduce the impact of motion artifacts on the heart rate estimation. Frequently, adaptive filter algorithms are applied to model the influence of motion that is recorded by the acceleration sensor to the PPG signal [22, 23, 27].

In [26, 28], three synthetic noise reference signals are generated internally from the artifact contaminated PPG signal itself. The reference signals were constructed from singular value decomposition (SVD), fast Fourier transform (FFT), and independent component analysis (ICA) and are applied to the adaptive step-size least mean squares (AS-LMS) filter for artifact removal. However, these methods are limited by the sensitivity to the reference signal, which is not able to represent all real-world characteristics, especially during various forms of physical activity.

ICA was also used in [21], where Kim and Yoo exploit the quasi-periodicity of PPG signals and the independence of the PPG and the motion artifacts via a combination of ICA and block interleaving. Krishnan *et al.* [24] propose a frequency domain ICA routine that is more effective in artifact removal than time-domain ICA. However, ICA based approaches rely on the assumption of statistical independence of motion artifacts and arterial volume variations, which could not be confirmed by Yao and Warren [20].

In 2015, Zhang *et al.* [15] proposed a framework for handling strong motion artifacts and, at the same time, provided a data set that is commonly used as a performance benchmark and also served as training data set for the Institute of Electrical and Electronics Engineers (IEEE) Signal Processing Cup 2015 [29, 30]. The framework is based on signal decomposition for denoising, sparse signal Reconstruction for high-resolution spectrum estimation, and spectral peak tracking with verification (TROIKA). However, TROIKA is very computational demanding, as we will see in Section 3.5, and therefore may not be suitable for wearable devices or may consume too much battery power.

A subsequent publication by Zhang [31] is based on joint sparse spectrum reconstruction (JOSS). It jointly estimates the spectra of the PPG and acceleration signals, utilizing the multiple measurement vector model in sparse signal recovery. JOSS achieves highly accurate results but is still computationally complex [32]. Both TROIKA and JOSS rely on large matrices which cannot be stored on embedded systems with constrained internal memory.

Khan *et al.* proposes a two-stage method for heart rate monitoring based on ensemble empirical mode decomposition (EEMD) [32]. The algorithm consists of an

EEMD-based PPG mode extraction, adaptive filter based denoising and some heuristic approaches for decision making. The accuracy of the method is very high and its computation time is faster than TROIKA and JOSS, but still significantly slower than the presented methods in this chapter.

Recently, hybrid motion artifact removal methods were proposed, which combines nonlinear adaptive filtering and signal decomposition. In [33], the PPG and acceleration signals were filtered by a second order recursive least squares (RLS) Volterra-based nonlinear adaptive filter to perform adaptive noise cancellation. A binary decision algorithm based on Pearson's correlation coefficient (CC) then decides whether or not to adopt singular spectrum analysis (SSA) to further reduce motion artifacts. However, the CC can only reveal linear relationships between the denoised PPG signal and the acceleration signal and would not indicate a strong nonlinear correlation, which would affect the denoising performance. To overcome this issue, Ye *et al.* revised their method and proposed a random forest-based binary decision algorithm that also exploits nonlinear features and obtains higher accuracy [34].

A recent overview of heart rate estimation algorithms using PPG signals and accelerometer signals during physical exercise is given in [35].

3.3 Contributions

Our contributions lie in proposing two distinct heart rate estimation methods using PPG and acceleration signals during physical activity.

The first heart rate estimation method is both highly accurate and low in computational cost. Its motion artifact removal is based on a set of adaptive filters that estimate the effects of motion on the PPG signal. By combining all filter outputs in the time-frequency domain, the algorithm is able to track the heart rate in the artifact-reduced signal. The proposed method outperforms previous work on a reference data set.

Furthermore, we present a new method that provides highly accurate heart rate estimates during physical exercise using extremely low computational cost and memory requirements. To achieve this, only fundamental signal processing functions are used that are easily implementable on hardware and allow for very rapid execution. Numerical results based on current benchmark data are provided, which show that the proposed approach outperforms state-of-the-art methods considerably in terms of computational time, while achieving similar accuracy.

3.4 Adaptive Filter Based Heart Rate Estimation

The proposed approach is based on three consecutive steps: First, the non-stationary impulse response $\mathbf{h}(n, \alpha_{acc})$ is estimated and the linear influence of the acceleration, which acts on the PPG sensor, on the noise-free PPG signal is removed. This estimation process is accomplished by an adaptive filter that minimizes the difference between the measured PPG and acceleration signal. Second, a signal enhancement is performed based on the adaptive filter outputs, where non-coherent noise components are suppressed by element-wise multiplication of the resulting spectra. Finally, a heart rate tracker follows the most probable high energy continuous line in the spectrum over time. An overview of the proposed algorithm is provided in Fig. 3.6.

3.4.1 Preprocessing

The PPG and acceleration signals with sampling frequency $f_s = 125$ Hz are band-pass filtered with a finite impulse response (FIR) filter using cut-off frequencies $f_{c1} = 0.6875$ Hz and $f_{c2} = 10$ Hz, and are downsampled by a factor $D = 6$ to 20.83 Hz. The choice of the cut-off frequencies f_{c1} and f_{c2} are physiologically motivated by the range of the heart rate of about 45 to 200 beats per minute (BPM), which corresponds to a frequency range of 0.75 to 3.33 Hz, and its first and second harmonic.

3.4.2 Noise Reduction by Adaptive Filtering

In the first part, the motion artifact suppression by use of adaptive filters is explained. First, a general topology for artifact suppression via adaptive filters is derived and the optimization criterion is defined. Then, the applied adaptive normalized least mean squares (NLMS) filter is described.

General Topology

The adaptive filter minimizes the power of acceleration signal components in the PPG signal, i.e., it maximizes the signal-to-motion artifact ratio (SMR). Based on this approach, we derive the difference equation

$$e(n) = p(n) - \hat{m}(n), \quad (3.1)$$

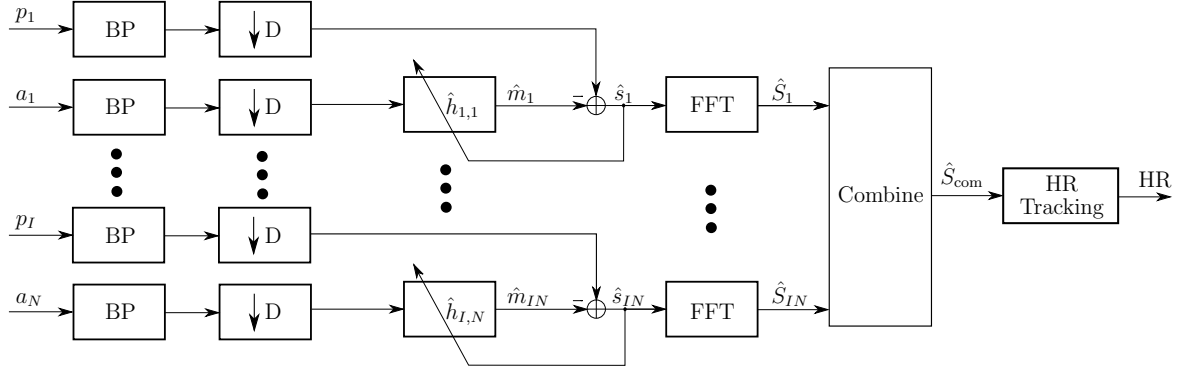


Figure 3.6. Overview of the proposed algorithm with $I = 2$ PPG signals and $N = 3$ acceleration signals, which results in $I \cdot N = 6$ adaptive filters. The inputs of the adaptive filters are band-pass filtered and downsampled by a factor D to reduce computational cost. The weighted combination is performed on the spectra which are efficiently computed by means of the FFT. Based on the combination of the spectra, the heart rate can be estimated and tracked in the final step. In this figure, the time and frequency indices are left out for the sake of clarity.

where $e(n)$ is the error signal, $p(n)$ is the measured PPG signal and $\hat{m}(n)$ is the estimated motion artifact caused by the acceleration. The adaptive filter structure is visualized in Fig. 3.7.

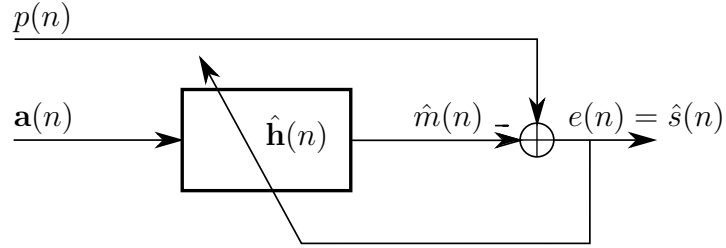


Figure 3.7. Adaptive filter structure for the removal of motion artifacts.

We can now transform (3.1) by replacing the estimated motion artifact $\hat{m}(n)$ by the product of the estimated impulse response $\hat{\mathbf{h}}(n, \alpha_{\text{acc}})$ and the measured acceleration vector $\mathbf{a}(n)$:

$$e(n) = p(n) - \hat{\mathbf{h}}^\top(n, \alpha_{\text{acc}})\mathbf{a}(n). \quad (3.2)$$

Here, the error signal $e(n)$ is, in fact, an estimate of the desired original PPG signal

$\hat{s}(n)$ without motion artifacts. In our approach, each PPG signal is combined with every dimension of the three-axis acceleration signal, yielding six adaptive filters that operate in parallel, see Fig. 3.6.

In our work, we applied different kinds of adaptive filters, such as, e.g., the Kalman filter [36], the Kalman smoother [25], the least mean squares (LMS) [22, 37], the NLMS filter [25], or the AS-LMS filter [28]. The Kalman filter achieved similar results as the NLMS filter but required more than double of the computational time. The standard formulation of the Kalman smoother can be used only after data acquisition is complete but not for real-time processing. Based on the normalization, the step-size value $\mu \in [0, 1]$ within the NLMS filter can be formulated much easier compared to the LMS filter. Finally, due to the low computational complexity $\mathcal{O}(N)$ and the requirement of a fast adaptive algorithm for real-time purposes, we decided to use the NLMS.

Normalized Least Mean Square (NLMS) Filter

The objective of the LMS filter is to minimize the mean squared error (MSE) $\min \mathbf{E}[|e(n)|^2]$. For a better control of the step-size μ , we compute the filter weights of the NLMS filter as follows:

$$\hat{\mathbf{h}}(n+1) = \hat{\mathbf{h}}(n, \alpha_{\text{acc}}) + \frac{\mu}{\mathbf{a}^\top(n)\mathbf{a}(n) + \delta} \mathbf{a}(n)e(n) \quad (3.3)$$

The value $\delta = 10^{-12}$ is added in practice for numerical stability reasons. Based on the experimental data, we have determined the optimal choice in terms of mean absolute error (MAE) to the reference for the step size to be $\mu = 0.1$ and for the NLMS filter order to be 9.

3.4.3 Signal Enhancement by Combination

The adaptive filtering provides estimates $\hat{s}_i(n)$, $i = 1, \dots, 6$ of the desired original PPG signal with reduced motion artifacts. At this point, the estimates need to be combined in a reasonable manner. This is done in order to remove all incoherent components, such as, e.g., the high noise floor, and enhance coherent components like those related to the heart rate.

For all six estimates of $s(n)$, the time-varying spectrum is estimated via the short-term Fourier transform (STFT). The combination of the six time-varying spectra is done by a computationally efficient and simple element-wise multiplication of the spectra. This multiplication leads to a lower noise floor level which is useful in order to extract the heart rate signal. We can formulate this as

$$\hat{S}_{\text{com}}(n, f) = \sqrt[6]{\prod_{i=1}^6 \hat{S}_i(n, f)}, \quad (3.4)$$

where $\hat{S}_{\text{com}}(n, f)$ is the combined spectrum dependent on the time index n and the frequency band index f . The variable $\hat{S}_i(n, f)$ corresponds to the channel i . In our simulations, we have fixed the frequency resolution of the FFT to 4096 bins.

3.4.4 Heart Rate Tracking

The last step in the proposed algorithm is the actual heart rate estimation. This estimation is based on an extremely simple tracker that follows the most probable high energy continuous line in the enhanced spectrum $\hat{S}_{\text{com}}(n, f)$. The frequency region, in which the highest energy is to be found, lies in an interval of ± 14 BPM of the preceding heart rate estimate. As an initialization for the first few estimates, the highest energy in the frequency region from 40 to 170 BPM is selected.

To avoid inaccurate estimates, we developed and introduced a simple heuristic tracking rule based on extensive heart rate data analysis similar to [15]: We assume that the heart rate will rarely increase or decrease more than 6 BPM within two successive time frames and in case of occurrence, a regularization is performed to shift the frequency region under observation for the next estimate by ± 6 BPM.

To prevent the tracking algorithm from losing the heart rate over a long time, the ratio between the highest peak in the observed frequency region and the highest peak in an interval of ± 100 BPM of the preceding heart rate estimate is calculated and compared to a predefined threshold T ,

$$\frac{\max\{\hat{S}_{\text{com}}(n, \Delta f_{100})\}}{\max\{\hat{S}_{\text{com}}(n, \Delta f_{14})\}} > T. \quad (3.5)$$

where Δf_k denotes the frequencies $-k \leq \hat{f}_{\text{HR}}(n-1) \leq k$, and $\hat{f}_{\text{HR}}(n-1)$ is the preceding heart rate estimate in BPM.

If the threshold T is exceeded, for example, because the algorithm had mistakenly tracked a non-stationary high power transient noise that lost its energy, it switches to the alternative high energy value in the frequency neighborhood. Based on the experimental data, we have determined the optimal ratio threshold in terms of MAE to the reference to be $T = 5,000$.

3.5 Computationally Efficient Heart Rate Estimation

The aim of this approach is to keep the computational complexity as low as possible and yet, present a reliable heart rate estimator for PPG signals. In contrast to the preceding approach, this method does not require the use of adaptive NLMS filters, which greatly reduces the computational complexity. Instead, we apply correlation functions to enhance periodic components and suppress wideband noise that is caused by motion-induced artifacts, or sensor and amplifier noise. The results for this method are based on using two PPG and three acceleration channels. However, the method is also applicable to other configurations. The summation of squared spectra further enhances common components between the PPG channels and suppresses remaining artifacts and noise. Motion artifacts are reduced by taking into account the estimated periodic components from the acceleration spectra. The heart rate estimation picks the maximal value in a weighted spectrum using a linear prediction. All steps are detailed in the subsequent sections.

3.5.1 Preprocessing

First, PPG and acceleration signals with sampling frequency $f_s = 125$ Hz are band-pass filtered with a FIR filter using cut-off frequencies $f_{c1} = 0.5$ Hz and $f_{c2} = 6$ Hz, and are downsampled by a factor of 5 to 25 Hz. Again, the choice of the cut-off frequencies f_{c1} and f_{c2} are physiologically motivated by the range of the heart rate of about 45 to 200 BPM, which corresponds to a frequency range of 0.75 to 3.33 Hz.

3.5.2 Signal Enhancement by Sample Correlation Functions

To enhance periodic components, we next calculate the sample correlation functions of the two measured PPG signals $p^i(n)$, $i = 1, 2$,

$$r_{p_i p_j}(\kappa) = \frac{1}{2N-1} \sum_{n=-N+1}^{N-1} p^i(n+\kappa)p^j(n), \quad i, j = 1, 2 \quad (3.6)$$

and normalize them

$$r_{p_i p_j}^{\text{norm}}(\kappa) = \frac{r_{p_i p_j}(\kappa) - \mu_{p_i p_j}}{\sigma_{p_i p_j}}, \quad i, j = 1, 2. \quad (3.7)$$

Here,

$$\mu_{p_i p_j} = \frac{1}{2N-1} \sum_{\nu=1}^{2N-1} r_{p_i p_j}(\nu), \quad i, j = 1, 2 \quad (3.8)$$

and

$$\sigma_{p_i p_j} = \sqrt{\frac{1}{2N-1} \sum_{\nu=1}^{2N-1} (r_{p_i p_j}(\nu) - \mu_{p_i p_j})^2}, \quad i, j = 1, 2. \quad (3.9)$$

Collecting the elements of (3.7) into vectors $\mathbf{r}_{p_i p_j}^{\text{norm}}$ results in three unique vectors $\mathbf{r}_{p_1 p_1}^{\text{norm}}$, $\mathbf{r}_{p_1 p_2}^{\text{norm}}$ and $\mathbf{r}_{p_2 p_2}^{\text{norm}}$.

3.5.3 Fourier Transformation

Finally, the FFT is applied to all three unique vectors. Each spectrum with 2048 bins and a resolution of 0.37 BPM is again normalized by subtracting its mean and dividing by the standard deviation, resulting in $\hat{S}_{11}(n, f)$, $\hat{S}_{12}(n, f)$ and $\hat{S}_{22}(n, f)$, respectively.

Next, we compute

$$\hat{S}_{\text{sum}}(n, f) = \hat{S}_{11}^2(n, f) + \hat{S}_{12}^2(n, f) + \hat{S}_{22}^2(n, f), \quad (3.10)$$

to further enhance common components between the channels and suppress uncorrelated background noise in the spectrum.

3.5.4 Harmonic Noise Damping

The spectrum resulting from (3.10) is multiplied element-wise with a Gaussian band-stop filter defined by the window function

$$w_{\text{acc}}(n, f) = 1 - \sum_{q=1}^2 e^{-\frac{1}{2} \left(\frac{f - \hat{f}_q(n)}{\sigma_{\text{win,acc}}} \right)^2}, \quad f = 1, \dots, F, \quad (3.11)$$

whose parameters $\hat{f}_1(n)$ and $\hat{f}_2(n) = \hat{f}_1(n)/2$ are estimated by tracking the frequencies $\hat{f}_q(n)$ that are associated with the maximal energy values of the accelerometer spectrum. Here, F is the number of frequency bins and the value of $\sigma_{\text{win,acc}} = 0.31$ Hz, which is about 19 BPM, is determined empirically.

3.5.5 Heart Rate Tracking

The heart rate is recursively obtained by evaluating

$$\hat{f}_{\text{HR}}(n) = \arg \max_f \hat{S}_{\text{sum}}(n, f) \cdot e^{-\frac{1}{2} \left(\frac{f - \hat{f}_{\text{HR}}^{\text{pred}}(n)}{\sigma_{\text{win,HR}}} \right)^2}, \quad (3.12)$$

where $\sigma_{\text{win,HR}} = 4$ BPM is the physiologically motivated width of the Gaussian window and $\hat{f}_{\text{HR}}^{\text{pred}}(n)$ is the predicted heart rate, which is the estimate of a linear least squares fit of the preceding three heart rate estimates

$$\hat{f}_{\text{HR}}^{\text{pred}}(n) = \alpha(n) + 2 \cdot \beta(n) \quad (3.13)$$

with

$$\beta(n) = \frac{\hat{f}_{\text{HR}}(n-1) - \hat{f}_{\text{HR}}(n-3)}{2} \quad (3.14)$$

and

$$\alpha(n) = \frac{1}{3} \sum_{i=1}^3 \hat{f}_{\text{HR}}(n-i). \quad (3.15)$$

If the frequency of the maximal energy in the accelerometer spectrum overlaps with the predicted heart rate, the heart rate is tracked either based on $\hat{S}_{11}(n, f)$ or $\hat{S}_{22}(n, f)$. The choice is made based on the maximal energy in the frequency bins of the last 5 estimated heart rates $\hat{f}_{\text{HR}}(n-i)$ with $i = 1, \dots, 5$. Finally, to smooth the heart rate estimate sequence, we restrict the tracker to maximally jump ± 4 BPM in relation to the last estimate.

3.6 Experimental Results

3.6.1 Real Data Set

For evaluation, we consider the training data set recorded by Zhang *et al.* [15] for the IEEE Signal Processing Cup 2015 [29, 30]. The training data set consists of twelve 5-min recordings that were collected from 12 healthy male subjects with age ranging from 18 to 35 years while running on a treadmill. Each recording includes a two-channel PPG signal, a three-axis acceleration signal, and a reference heart rate for evaluation, obtained from a simultaneously measured ECG signal.

The PPG signals were recorded from the subjects' wrist using a pulse oximeter with green LEDs (wavelength: 515 nm). The acceleration signals were recorded at the same position. Both the PPG sensors and the accelerometer were embedded in a comfortable wristband. The ECG was simultaneously recorded from the chest using wet ECG electrodes. All signals were acquired with a sampling rate of 125 Hz and were sent to a nearby computer via Bluetooth.

During data recording, the subjects walked or ran on a treadmill with the following speeds in order: the speed of 1-2 km/h for 0.5 min, the speed of 6-8 km/h for 1 min, the speed of 12-15 km/h for 1 min, the speed of 6-8 km/h for 1 min, the speed of 12-15 km/h for 1 min, and the speed of 1-2 km/h for 0.5 min.

We adapt the framework of the IEEE Signal Processing Cup 2015 and estimate the heart rate every 2 s based on overlapping time windows of 8 s length. This way, the algorithm is able to monitor the heart rate in real-time which is a common requirement for many applications, such as, e.g., for athletes to adjust their training program during the exercise.

3.6.2 Evaluation Metrics

The performance of the proposed approaches is evaluated and compared to state-of-the-art methods by two established evaluation metrics: the average absolute error (AAE) and the average absolute error percentage (AAEP).

The AAE is defined as

$$\text{AAE} = \frac{1}{N} \sum_{i=1}^N |\hat{f}_{\text{HR}}(n) - f_{\text{HR}}(n)|, \quad (3.16)$$

where N is the total number of estimates, $f_{\text{HR}}(n)$ denotes the ground truth of the heart rate value in the n -th time window in terms of BPM, and $\hat{f}_{\text{HR}}(n)$ denotes the corresponding heart rate estimate in BPM.

Analogously, the AAEP is defined as

$$\text{AAEP} = \frac{1}{N} \sum_{i=1}^N \frac{|\hat{f}_{\text{HR}}(n) - f_{\text{HR}}(n)|}{f_{\text{HR}}(n)}. \quad (3.17)$$

3.6.3 Heart Rate Estimation Accuracy

We compare our two proposed methods with frequently cited state-of-the-art methods, which were also evaluated on the same, widely used data set of the IEEE Signal Processing Cup 2015. However, note that TROIKA and JOSS excluded multiple segments

(in total 32 s) with strong motion artifacts in their performance evaluation because both algorithms did not output heart rate estimates. The strong motion artifacts are probably due to device adjustment after the recording system turned on. The exclusion of strongly disturbed signal sections must be taken into account when comparing these results with our proposed methods.

Tables 3.2 and 3.3 list the heart rate estimation results of both the adaptive filter (AD) and the computationally efficient (CE) approach and state-of-the-art methods in terms of the AAE and the AAEP, respectively, for each subjects' recording and gives an overall average AAE. The average AAE over all 12 subjects of both proposed methods, 1.66 BPM for the AD and 1.32 BPM for the CE approach, is comparable to the state-of-the-art methods, whereas the standard deviation (STD) is significantly lower for our methods with 0.88 BPM and 1.24 BPM, respectively. The most difficult recording for all methods comes from subject 10, which was due to very low signal quality and strong motion artifacts in the PPG signals. The best evaluation performances were achieved for subject 8 with an AAE of around 0.5 to 1 BPM.

The best and worst heart rate estimation results of our methods including the ECG-based ground truth is exemplarily shown in Fig. 3.8 and Fig. 3.9, superimposed on the artifact-reduced spectrograms. The intensities of the spectrograms differ, since the algorithms have different signal and noise power levels due to their respective motion artifact removal and their calculation of the spectra.

It can be stated that a sufficient accuracy of the heart rate estimation has already been achieved. An average deviation of 1-2 BPM is reasonable for the application during physical activity. A further accuracy optimization on this data set has been reported in [32, 38–40], but is not of practical interest. This is especially the case because the reference values from the ECG may contain inaccuracies or may not be perfectly measured. It is also difficult to average a heart rate over a period of 8 s as the heart rate could change dramatically within those 8 s.

In addition to the accuracy, in the next subsection we look at the computational complexity of the algorithms.

3.6.4 Computational Complexity

While all methods achieve a comparable and sufficiently high accuracy for the considered use-case, they strongly differ in their computational complexity. The total

duration of the computation times is shown in Table 3.1. As reported in [32], the heart rate estimation of the training set takes several hours for TROIKA [15] and 300 s for JOSS [31], which is of a similar magnitude (402 s) as for our own implementation of JOSS.

Our first presented adaptive-filter based method [16] needs about 51 s. In comparison, our second, the computationally efficient approach spends only 3.73 s to run the complete training set, which is roughly 80 times faster than JOSS and almost 14 times faster than the first proposed approach. The computation time for our methods was evaluated on a 2.8 GHz Intel[®] Core[™] i5-760 CPU with 8 GB RAM and MATLAB R2016a. Please note that the most complex operation is the FFT, which is an $\mathcal{O}(N \log N)$ operation. For each time window of 8 s, the FFT is executed six times to transform the two time-domain PPG signals, their cross-correlation as well as three accelerometer signals into the frequency domain. Those six vectors with 2048 bins are the biggest variables in the storage.

	Total Duration (12 Data Sets)
CE Method	3.73 seconds
AF Method	51.46 seconds
EEMD [32]	199 seconds
JOSS [31][†]	300 seconds
TROIKA [15][†]	3.5 hours

[†] The computation time for this method are obtained from [32] using the M-FOCUSS algorithm [41], which is by far the most complex operation in TROIKA and JOSS. Our own implementation of JOSS using [42] achieved similar computation times.

Table 3.1. Total computation times for the training data [15]. Both the adaptive filter (AF) and the computationally efficient (CE) method considerably outperform state-of-the-art methods.

	S 1	S 2	S 3	S 4	S 5	S 6	S 7	S 8	S 9	S 10	S 11	S 12	Mean \pm STD
AD Method	2.52	1.42	2.22	1.18	1.08	1.49	1.32	0.90	0.74	3.91	1.73	1.34	1.66 \pm 0.88 BPM
CE Method	1.45	1.29	0.58	1.52	0.78	0.86	1.02	0.65	0.39	5.07	0.79	1.46	1.32 \pm 1.24 BPM
EEMD [32]	1.64	0.81	0.57	1.44	0.77	1.06	0.63	0.47	0.52	2.94	1.05	0.91	1.07 \pm 2.17 BPM
JOSS [31]	1.33	1.75	1.47	1.48	0.69	1.32	0.71	0.56	0.49	3.81	0.78	1.04	1.28 \pm 2.61 BPM
TROIKA [15]*	2.87	2.75	1.91	2.25	1.69	3.16	1.72	1.83	1.58	4.00	1.96	3.33	2.42 \pm 2.47 BPM

* The results for this method are obtained from [31].

Table 3.2. Average absolute error (AAE) for the proposed adaptive filter (AD) based approach and the computationally efficient (CE) approach over all 12 data sets from the training data [15] in BPM.

	S 1	S 2	S 3	S 4	S 5	S 6	S 7	S 8	S 9	S 10	S 11	S 12	Mean \pm STD
AD Method	2.16	1.36	2.07	1.05	0.84	1.16	0.99	0.77	0.61	2.57	1.14	0.98	1.31 \pm 0.62 %
CE Method	1.20	1.27	0.48	1.44	0.63	0.68	0.76	0.56	0.31	3.22	0.51	1.04	1.01 \pm 0.78 %
JOSS [31]	1.19	1.66	1.27	1.41	0.51	1.09	0.54	0.47	0.41	2.43	0.51	0.81	1.01 \pm 2.29 %
TROIKA [15]*	2.18	2.37	1.50	2.00	1.22	2.51	1.27	1.47	1.28	2.49	1.29	2.30	1.82 \pm 2.07 %

* The results for this method are obtained from [31].

Table 3.3. Average absolute error percentage (AAEP) for the proposed adaptive filter (AD) based approach and the computationally efficient (CE) approach over all 12 data sets from the training data [15] in %.

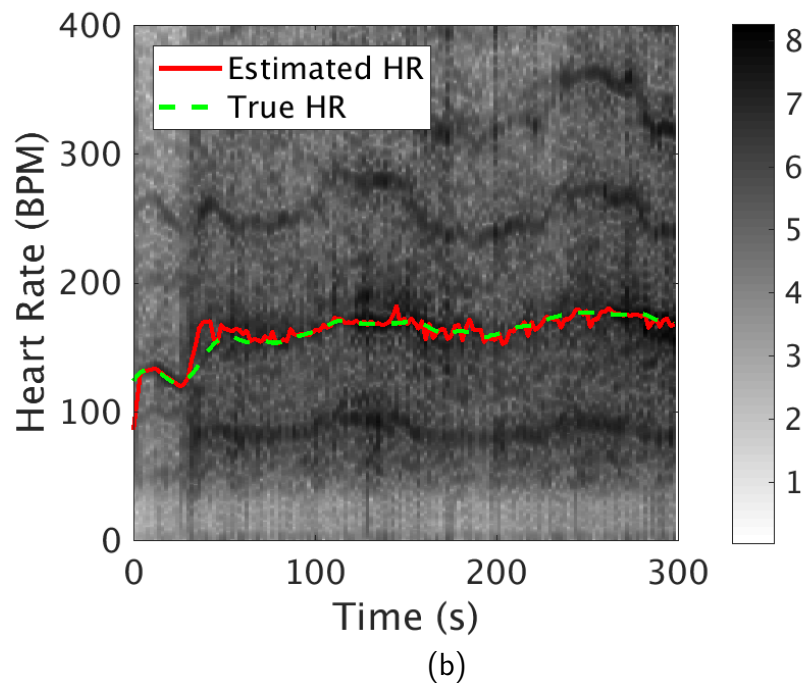
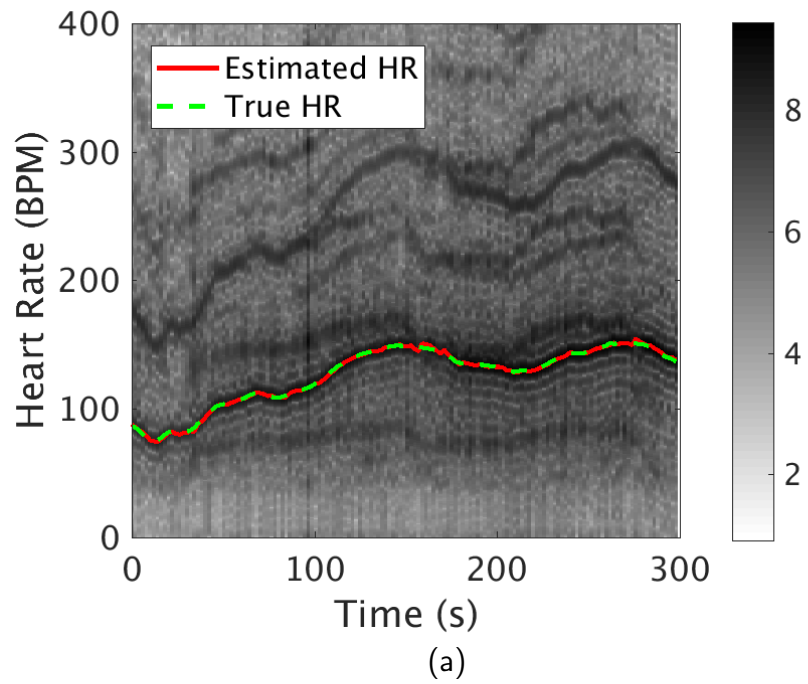
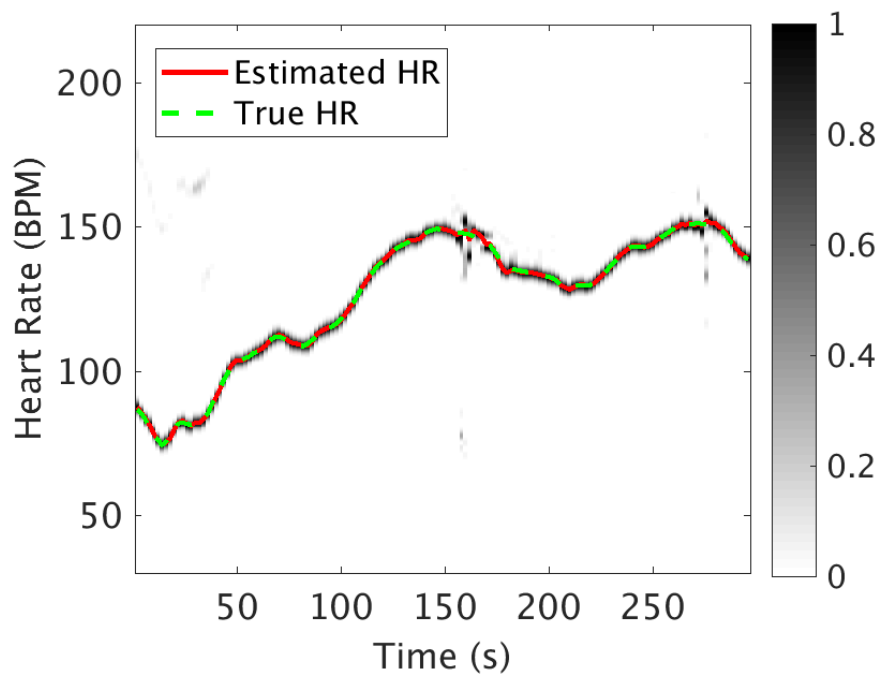
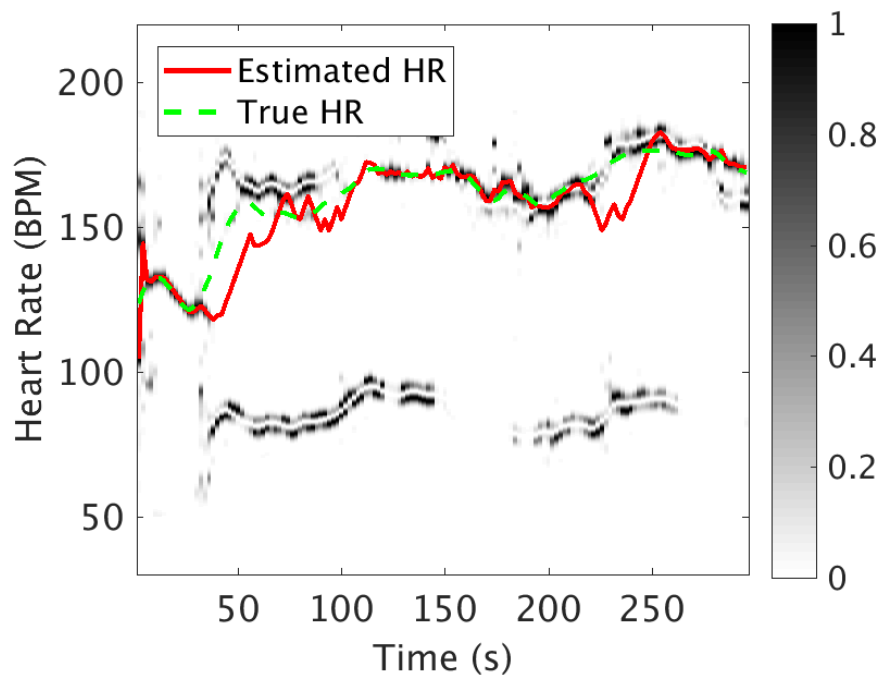


Figure 3.8. Heart rate (HR) estimates of the adaptive filter (AD) based approach depicted together with the true heart rate on the combined spectrogram of all six adaptive filter outputs for (a) the best result (S 9) and (b) the worst result (S 10).



(a)



(b)

Figure 3.9. Heart rate (HR) estimates of the computationally efficient (CE) approach depicted together with the true heart rate on the spectrogram, on which harmonic noise damping and background noise reduction was applied, for (a) the best result (S 9) and (b) the worst result (S 10).

3.7 Discussion

Real-time heart rate estimation from PPG signals has become a very active field of research and is a key step in developing wearable devices that can monitor the heart rate in a non-invasive way. The IEEE Signal Processing Cup in 2015 and the associated publication of Zhang *et al.* [15], in which they published the widely used dataset for heart rate estimation using PPG signals, initiated the begin of this active research field. In addition to universities and research institutions, many leading high-tech companies are actively working on heart rate monitoring, as it is an important feature in modern wearable devices such as fitness trackers or smartwatches. A large number of algorithms have since been published and evaluated on the benchmark data set of Zhang *et al.*. However, some of the published methods have been described in such a way that reproduction is either impossible or very difficult. Our methods are based on simple functions and techniques and are therefore easy to understand, reproduce, and implement.

Since the average error of our methods is around 1.5 BPM and, thus, clinically acceptable, PPG sensors have the potential to replace ECG for heart rate estimation, which is inconvenient and has to be collected from a minimum of three electrodes. A further improvement of the algorithms should therefore no longer be based on pure accuracy, especially since the heart rate is averaged over a data block of 8 s and compared with the reference value of an ECG, which itself can be erroneous under certain conditions. Within these 8 s, the heart rate can change by several tens of digits, e.g., at the start of an exercise, at a shock moment, or at a sudden rest after a hard exertion.

Hence, our proposal for future research would be to include and publish a new, far more comprehensive data set with measurements from a large number of subjects during a variety of activities, so that algorithms can be tested for more realistic situations. The evaluation should then not only focus on the accuracy of the estimation, but also on other aspects such as speed, implementability, and reliability. If it is advantageous for the accuracy to adapt the estimation method to the respective physical activity, as many manufacturers of fitness trackers and smartwatches seem to already do, the automatic recognition of the activity and the speed with which the algorithm adjusts to it should be investigated as well. For a long battery life and easy implementation in embedded devices, it is also important to develop algorithms with low computational complexity, as we have already achieved with our second proposed method.

3.8 Summary and Conclusions

In this chapter, we have presented two approaches to monitor a subject's heart rate in real-time during physical activity using PPG and acceleration signals. In the first approach, we reduced the influence of motion artifacts in the PPG signal by using adaptive filters that estimate the effects of motion on the signal. We combined the outputs of the adaptive filters to enhance the spectral quality and finally presented a constrained heart rate tracker that follows the most probable high energy continuous line in the spectrum over time. Real data experiments showed very accurate results on a widely used benchmark dataset. Further, we have presented a very computationally efficient algorithm to monitor a subject's heart rate in real-time during physical activity. This approach combined correlation-based fundamental frequency indicating functions, spectral combination, harmonic noise damping, and frequency domain tracking. The low computational complexity allows for running the algorithm in real time on a wearable device while keeping the battery consumption as low as possible. Despite its low computational complexity and memory requirements, the proposed method is comparable in terms of accuracy to computationally intensive state-of-the-art methods on the benchmark data set.

Chapter 4

Cardiovascular Health Monitoring

In this chapter, we present two methods for monitoring the cardiovascular health, i.e., for detecting atrial fibrillation (AF) and estimating blood pressure (BP), pulse wave velocity (PWV), and vascular age index (VAI) from PPG signals.

In the first part of this chapter, we present a framework for the detection of AF with a smartphone by utilizing the video camera as a PPG sensor, as described in Section 2.3.1. The proposed algorithm transforms the video signal into an enhanced PPG signal and extracts statistical discriminating features. Through sequential forward selection (SFS) and support vector machine (SVM), simple classification equations can be applied to distinguish between normal sinus rhythm (NSR) and AF. The presented algorithm has a low computational cost and low memory requirements.

In the second part, we present an approach to estimate cardiovascular parameters from a single PPG signal. The method extracts a large set of features from the PPG signal and recovers missing values by matrix completion. Based on feature selection, the most significant features for each cardiovascular parameter are presented. Finally, we apply support vector regression (SVR) with a nonlinear Gaussian kernel and present our results on a self-recorded data set. We compare our results with linear and robust linear regression methods and show that the proposed method is capable of accurately estimating the cardiovascular parameters of a new measurement using only ten features, given training data of the subject. The results are promising, because they indicate the possibility of designing single PPG approaches, that achieve accurate results for a subject, given only a single reference measurement of that subject and sufficient training data from other subjects.

In Section 4.1, we start with an introduction to cardiovascular diseases (CVDs) and motivate monitoring cardiovascular health parameters, such as, e.g. BP or PWV. The contributions of this chapter are summarized in Section 4.2. Before describing both methods, the state of the art in AF detection and cardiovascular parameter estimation using PPG signals is given in Section 4.3. Our method for the detection of AF is presented in Section 4.4 and the framework for the estimation of BP, PWV, and VAI is explained in Section 4.5. Finally, a conclusion is drawn in Section 4.6.

The main contributions in this chapter have been published in [43] and have served in parts as basis for [44].

4.1 Introduction

CVDs are the most common cause of death worldwide [45]. Almost 18 million people die of CVDs every year. That is an estimated 31 % of all deaths. 80 % of all CVD deaths are due to heart attacks and strokes. AF is the most common type of arrhythmia and one of the major causes of stroke, heart failure, sudden death, and cardiovascular morbidity in the world [46]. In 2010, it was estimated that 33.5 million people worldwide have AF [47] and, according to [48], almost one in four middle-aged adults in the USA and Europe will develop AF. However, undiagnosed AF is common, especially in older populations and for patients with heart failure [49]. Effective AF treatments could reduce risk for complications from AF. Thus, a major challenge is the early and reliable detection of AF, which would be possible based on permanently monitoring the heartbeat patterns.

High blood pressure or hypertension is the most common risk factor for AF, a common condition leading to CVDs, and an important indicator of cardiovascular health [50]. Increased arterial stiffness, which reflects structural arterial wall modifications and characterizes vascular aging, is associated with several factors including hypertension [51]. Arterial stiffness is a cardiovascular risk factor and can be an independent predictor of CVDs [52]. A permanent monitoring of the blood pressure and vascular stiffness values would be helpful in order to be able to detect and prevent negative developments at an early stage.

The noninvasive gold standard for evaluating arterial stiffness is the carotid-femoral (aortic) PWV [53], which is the velocity at which the arterial pulse wave propagates through the arteries. The PWV is directly related to arterial stiffness by the Moens-Kortweg equation [54] and an indicator for arteriosclerosis. The European Society of Hypertension (ESH) recognizes PWV as a useful additional test in the investigation of hypertension [55]. In recent years, more and more devices that directly or indirectly estimate the stiffness of the aorta have started to model the vascular age based on stiffness estimation [56] and calculate a VAI, a single parameter for quantifying arterial stiffness and indicating a person's vascular age. The comparison of the VAI with the chronological age of a person contributes to a better understanding and awareness among non-medical experts. If the VAI is older than the chronological age, there is an increased risk of CVDs. The key risk factors for CVDs are unhealthy diet, physical inactivity, obesity, tobacco use, and harmful use of alcohol. In addition to reducing these risk factors, monitoring the heart rate, BP, PWV, and VAI can help with the prevention, detection, and recovery of CVDs.

4.2 Contributions

In this chapter, we present two methods for monitoring the cardiovascular health using PPG signals.

First, we propose a practically realizable photoplethysmography-based method that detects AF using smartphones at a low computational cost and with low memory requirements. We propose an approach to acquire PPG signals from the video camera of a smartphone and calculate a set of features to discriminate AF from NSR and to automatically exclude measurements with strong hand movements. With the use of feature selection and SVM we achieve perfect detection of AF on a clinically recorded data set.

Our second contribution is to propose a novel approach for estimating BP, PWV, and VAI from a single PPG signal. First, we address the challenge of accurately extracting features from the PPG signal and its first and second order difference series, and describe signal processing methods how to find the features. In case of missing feature values, we propose a method based on matrix completion to ensure a continuous estimation. We apply feature selection and demonstrate which features are particularly significant for the estimation of the individual cardiovascular parameters. We conduct a study consisting of 18 subjects and 42 measurements of BP, PWV, and VAI. We evaluate different regression models including robust linear regression and nonlinear SVR. Additionally, we investigate the influence of subject calibration on the estimation accuracy. We validate our approach and compare it with a state-of-the-art method using pulse arrival time (PAT).

4.3 State of the Art

Currently, AF diagnosis requires heart rhythm monitoring with an electrocardiogram (ECG) to reveal irregular heartbeat patterns. Considering the availability of recording devices and the effort of recording an ECG, the photoplethysmogram, which is typically measured from fingertips, wrists, or earlobes, offers a readily accessible, inexpensive and simple to operate alternative. The acquisition of PPG signals from smartphones has been examined by many researchers [57–59]. Lee *et al.* has first demonstrated the feasibility of AF detection based on an iPhone 4s [7] and related works have followed [8, 9, 11]. However, we observed that state-of-the-art methods mostly rely on the peak-to-peak intervals (PPI) and that there is a lack of investigation on features

that take other specific characteristics of the PPG signal into account. Furthermore, to classify AF, often fixed thresholds are set for single features instead of using more sophisticated classification algorithms or combining the features. Moreover, measurements with strong hand movement are not automatically detected and removed from analysis, and ECG-based classification performance is not achieved.

The measurement of BP can be performed with several techniques. Traditionally, the gold standard of accuracy for noninvasive BP measurements has been the sphygmomanometer, which consists of an inflatable cuff, a measuring unit, and a mechanism for inflation, either a manually operated bulb or an electrically operated pump. Nowadays, one of the most common automated measurement methods for BP is oscillometry [60], as it does not require medical personnel and can be easily used at home. However, this technique cannot perform continuous measurements, unlike methods based on arterial tonometry [61], which is a technique in which an array of pressure sensors is pressed against the skin over an artery. The volume-clamp method (Finapres) is based on the principle of dynamic unloading of the arteries in the finger and measures the finger arterial pressure using a finger cuff and an inflatable bladder in combination with an infrared plethysmograph [62]. Although this method can provide continuous estimates of blood pressure, a cuff wrapped around the arm or finger is still required, which is cumbersome, non-portable, and impractical for daily or long-term uses [63]. An alternative cuffless method is based on continuous wave radar [64], but needs placement of a transmitter and receiver antenna at the sternum and four electrodes for the bioimpedance (BImp) and ECG across the shoulder.

The current noninvasive methods to measure the PWV can be divided into three main groups: imaging, non-imaging, and optical methods [65]. Imaging methods that are routinely used in clinical environments, such as ultrasound or magnetic resonance imaging (MRI), have the advantage of a direct measurement of the path length and high accuracy but are very expensive and difficult to operate. More affordable and validated technologies are non-imaging methods such as the Complior[®], SphygmoCor[®], Arteriograph[®], or Mobil-O-Graph[®] [66]. Many manufactures of these devices have launched models into their devices to calculate the VAI based on their PWV estimation and background factors, e.g., age, sex, or body mass index (BMI). However, these devices are mainly used in clinical environments, require a cuff and professional medical training. Although optical methods, such as photoplethysmography, can only be used at peripheral sites and are still in the early stages of validation, they show promising results, are low-cost, and enable simple, cuffless, and continuous estimation.

The underlying principle of existing photoplethysmography-based methods to estimate BP, PWV, or VAI is the pulse transit time (PTT), which describes the time a pressure

wave takes to travel between two arterial sites [63, 67–71]. Commonly, the PAT is calculated by the time difference between the R-peak of the QRS complex from an ECG and a characteristic point of the PPG signal. Here, the PAT is a combination of the PTT and the pre-ejection period (PEP) which is the time between the beginning of electrical stimulation of the left ventricle and the opening of the aortic valve. A challenge for PAT-based methods is the individual calibration for each user before the monitoring to calculate model parameters required for accurate BP estimation. Some papers extract numerous features from the PPG signal or its first and second order difference series but remain short on the details of how to find the information from a signal processing point of view [71–73]. There is also a discussion whether linear or nonlinear regression models are necessary for BP and PWV. Miao *et al.* recently demonstrated that nonlinear SVR slightly outperforms linear regression, indicating a nonlinear relation between the features and cardiovascular parameters. However, they still recommend linear regression over SVR due to its low-power and low-complexity requirements [71].

4.4 Atrial Fibrillation Detection

In this section, we introduce a new method to detect AF with a PPG signal recorded with the video camera of smartphones, such as iPhone 5s, iPhone 6 Plus and iPhone 6s Plus. Fig. 4.1 summarizes the general principle of the algorithm.

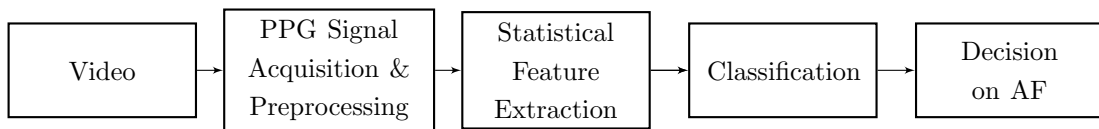


Figure 4.1. General principle of the algorithm to detect AF with a PPG signal recorded with the video camera of smartphones.

4.4.1 PPG Signal Acquisition and Preprocessing

The PPG signals are acquired from the smartphones by using their camera and flash. The method requires a static position of a finger on the camera. In contrast to other studies [7, 8, 59] that simply average 50×50 pixels of each video frame, we propose a novel method to better capture the variations of the pulsatile signal while reducing the computational cost and memory requirements.

The first step of our method is to take a subset on an equidistant grid of 50×50 pixels from the first 5 s of the captured video. Following the findings of [10, 58, 74], we choose to generate the signal solely based on the red channel of each video frame and do not consider the green or blue channel. We calculate the variance of each pixel $b_k(n)$, $k \in \{1, \dots, 2500\}$ over $N_{\text{init}} = 150$ frames (the frame rate is 30 frames per second (fps))

$$\sigma_k^2 = \frac{1}{N_{\text{init}} - 1} \sum_{n=1}^{N_{\text{init}}} (b_k(n) - \mu_k)^2, \quad (4.1)$$

with

$$\mu_k = \frac{1}{N_{\text{init}}} \sum_{n=1}^{N_{\text{init}}} b_k(n), \quad (4.2)$$

and select the N_{var} pixels $b_{\tilde{k}}(n)$ with the highest variance, i.e., $\sigma_{\tilde{k}=1}^2 > \sigma_{\tilde{k}=2}^2 > \dots > \sigma_{\tilde{k}=N_{\text{var}}}^2$, where \tilde{k} denotes the index of the ordered set of variances. Finally, we obtain the PPG signal of the entire measurement by averaging only the selected pixels in each of the remaining frames of the video

$$p(n) = \frac{1}{N_{\text{var}}} \sum_{\tilde{k}=1}^{N_{\text{var}}} b_{\tilde{k}}(n). \quad (4.3)$$

Fig. 4.2 compares a PPG signal that is acquired by randomly averaging 50×50 red channel pixels per frame and our proposed method that averages only over the N_{var} most variant pixels in the red channel, showing higher signal energy. The resulting PPG signal is filtered with a 4th order Butterworth band-pass filter with cut-off frequencies $f_{c_1} = 0.5$ Hz and $f_{c_2} = 4$ Hz.

4.4.2 Statistical Feature Extraction

Similar to other studies [7, 8, 11, 75] we calculate statistical features from the PPG signal to distinguish between AF and NSR. In addition, we also make use of the features to detect strong hand movement during the measurement and label them as vibration (Vib). Implemented in a smartphone application, the user can be immediately informed that the measurement should be repeated. The statistical features are divided into two categories that are associated with the time domain and the frequency domain of the PPG signal.

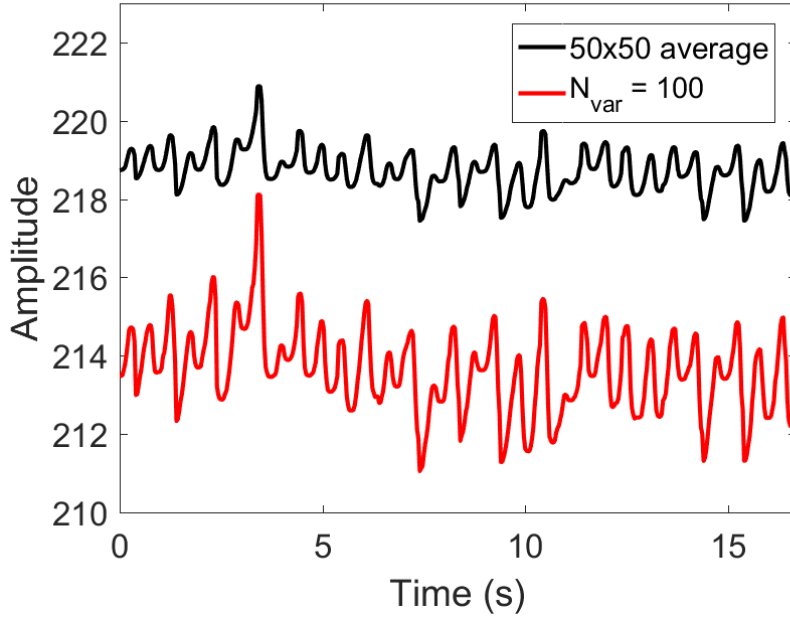


Figure 4.2. Comparison of an acquired PPG signal example before band-pass filtering using the conventional method that averages over a subset of 50×50 pixels, and our method that averages only over the $N_{\text{var}} = 100$ most variant pixels of the 50×50 pixel grid and has higher signal energy.

4.4.2.1 Time-Domain Features

As the irregular heartbeat sequence during AF results in an increased heart rate variability (HRV), we calculate typical HRV parameters [76] for time windows of 20 s. Thanks to the steps described in Section 4.4.1, we are able to use a simple peak detection algorithm that detects a local peak when a data sample is larger than its two neighboring samples. From the peak location differences, we calculate the root mean square of successive differences (RMSSD)

$$\text{RMSSD} = \sqrt{\frac{1}{N_{\text{diff}} - 1} \sum_{l=1}^{N_{\text{diff}}-1} (\Delta_{l+1} - \Delta_l)^2}, \quad (4.4)$$

which captures the variation of the N_{diff} adjacent peak location differences $\Delta_l = t_{l+1} - t_l$, where t_l is the l -th peak location in the PPG signal. In general, RMSSD is expected to be higher for patients with AF.

The normalized root mean square of successive differences (nRMSSD)

$$\text{nRMSSD} = \frac{\text{RMSSD}}{\frac{1}{N_{\text{diff}}} \sum_{l=1}^{N_{\text{diff}}} \Delta_l}, \quad (4.5)$$

adjusts for the effect of heart rate.

A further highly discriminating time-domain feature is the Shannon entropy

$$\text{ShE} = - \sum_{l=1}^{N_{\text{diff}}} \Delta_l^2 \log(\Delta_l^2). \quad (4.6)$$

In general, Shannon entropy is expected to be higher for patients with AF since it quantifies the uncertainty in the distribution of the peak location differences. Further features are computed from the statistics of the successive peak location differences, such as, the mean, median, standard deviation (STD) and the mean absolute deviation (MAD).

In addition to these commonly used features, we take into account the variation of the pulse waveform and determine the mean, median, STD and MAD of the following parameters: the crest time [2], which is the time from the foot of the PPG waveform to its peak, the peak rise height (PRH), the fall height and the waveform width as shown in Fig. 4.3, as well as the cross-correlation of consecutive pulse segments [77].

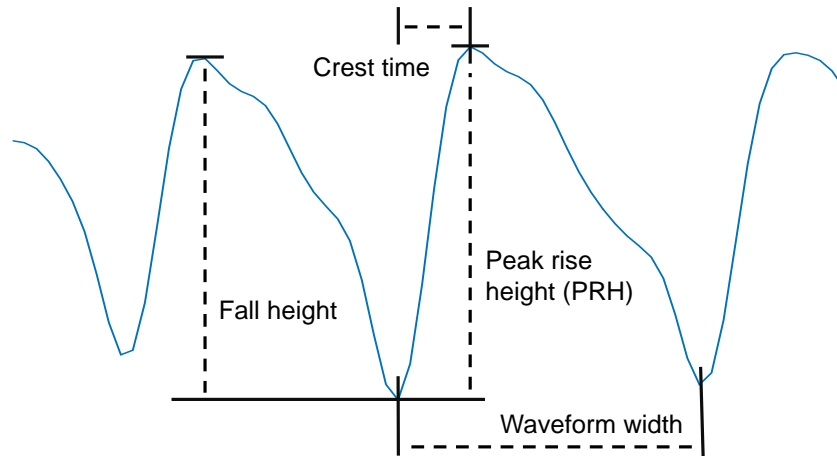


Figure 4.3. Time-domain features extracted from the PPG waveform: the crest time [2], the peak rise height (PRH), the fall height, and the waveform width.

4.4.2.2 Frequency-Domain Features

We also incorporate frequency-domain HRV features, which provide additional evidence to distinguish an AF measurement from an NSR measurement [76]. For this, we interpolate the sequence of peak location differences Δ_l , $l \in \{1, \dots, N_{\text{diff}}\}$ to a regular grid using an equidistant grid interval of 0.25 s. Stacking the resulting series into the vector $\tilde{\Delta} \triangleq (\tilde{\Delta}_1, \dots, \tilde{\Delta}_{\tilde{N}_{\text{diff}}})^\top$ and applying the fast Fourier transform (FFT) yields

$$\tilde{\Delta}(f_j) = \mathcal{F}\{\tilde{\Delta}\}, \quad f_j = 0, \dots, F_\Delta \quad (4.7)$$

with $F_\Delta = 2$ Hz.

From (4.7), features are formed by extracting the spectral powers in the very low frequency (VLF) range from 0 Hz to 0.04 Hz, in the low frequency (LF) range from 0.04 Hz to 0.15 Hz and in the high frequency (HF) range from 0.15 Hz to 0.4 Hz, as well as the quotients of these spectral powers.

In contrast to previous studies [7, 8, 11, 75], we expand the set of statistical features by incorporating frequency-domain features of the PPG signal. For this, we first divide the PPG signal into segments of 5 s with an overlap of 80 % and normalize them by subtracting their mean and dividing by their standard deviation. Let these segments, for $m = 1, \dots, M_{\text{seg}}$, be represented by $\mathbf{p}_m^{\text{seg}} = [p_m^{\text{seg}}(1), \dots, p_m^{\text{seg}}(N_{\text{seg}})]^\top$, where M_{seg} is the total number of segments and N_{seg} denotes the segment length. Then applying the FFT

$$P(f_i, m) = \mathcal{F}\{\mathbf{p}_m^{\text{seg}}\}, \quad f_i = 0, \dots, F_p \quad (4.8)$$

with $F_p = 3.33$ Hz at a spectral resolution of 0.015 Hz allows for computing a variety of features, such as: maximal spectral peak, differences of the maximal spectral peak positions, summed spectral energy, peak to sum ratio, spectral entropy, and kurtosis of the spectrum

$$\text{Kurt}_m = \frac{\frac{1}{F_p} \sum_{i=0}^{F_p} (P(f_i, m) - \mu_P(m))^4}{\left(\frac{1}{F_p} \sum_{i=0}^{F_p} (P(f_i, m) - \mu_P(m))^2\right)^2}, \quad (4.9)$$

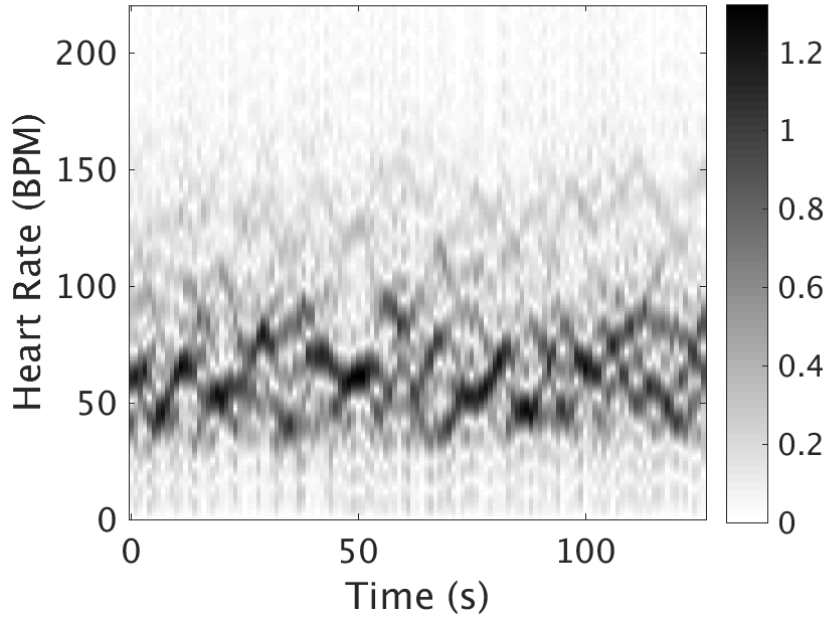


Figure 4.4. Spectrogram for an exemplary recording of a patient with AF. The chaotic spectral power distribution indicates irregular heart beating in the presence of AF.

where $\mu_P(m) = \frac{1}{F_p} \sum_{i=0}^{F_p} P(f_i, m)$. To perform classification, we have to be consistent with the time-domain features, which provide one feature vector every 20 s. Therefore, we calculate the mean, median, STD and MAD of the frequency-domain features. This reduces the multiple feature vector from the overlapping 5 s segments to a single value each 20 s. Two exemplary spectrograms for a patient with AF and a patient with NSR for a measurement of 2 min are shown in Fig. 4.4 and Fig. 4.5, respectively.

4.4.2.3 Acceleration Features

Strong movement of the patient can deteriorate the quality of a PPG measurement. To avoid manual data screening by trained staff, we propose to consider acceleration features to automatically detect strong movement of a patient. In a mobile phone application, when strong movement has been detected, e.g., the patient can be asked to repeat the recording. After subtracting the mean of in each direction the of acceleration, we calculate the mean, median, MAD and STD of the time- and frequency-domain energy in each direction and in total.

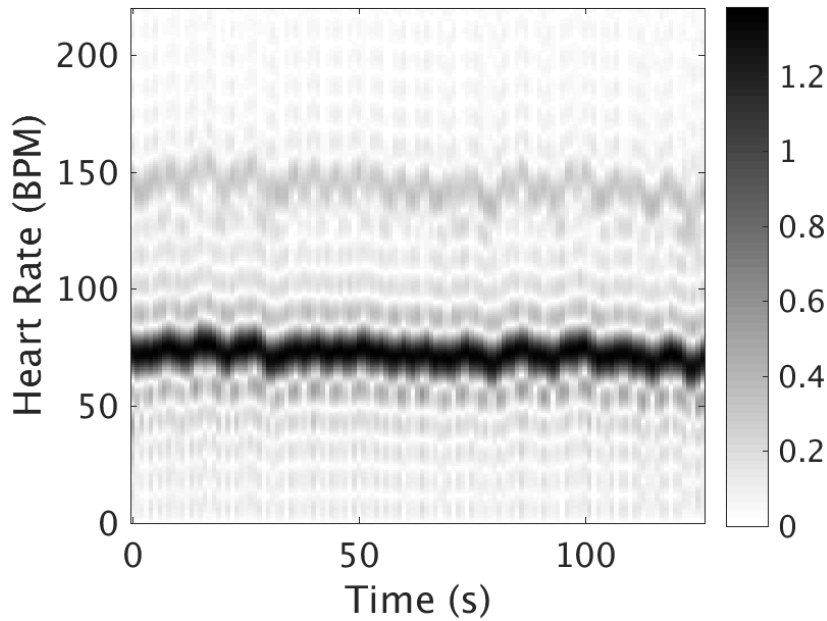


Figure 4.5. Spectrogram for an exemplary recording of a patient with NSR. The spectral power distribution indicates a nearly constant sinusoidal heart rate at around 75 BPM.

4.4.3 Feature Selection and Classification

We divide the classification procedure into two different stages: wrapper type feature selection and classification via SVM. Both stages are computationally demanding but are not intended to be implemented in smartphone applications, which only need the resulting classifications rules. First, the feature selection aims at finding the best feature combination of the presented set of features to distinguish between the classes. Feature selection reduces the computational cost and reveals the different levels of the features' significance. Then, the SVM is applied to find the optimal decision equation to separate the classes. Finally, only the features of the best combination need to be calculated in the smartphone application and classification can be performed based on decision lines for pairs of features or hyperplanes in case of multiple features.

4.4.3.1 Sequential Forward Selection (SFS)

We apply SFS to find the best feature combinations heuristically [78]. SFS sequentially adds features to an empty candidate set until the addition of further features does not decrease the misclassification rate. We use a 5-fold stratified cross-validation with

100 Monte-Carlo repetitions to minimize the misclassification rate and reduce the total number of 85 features.

4.4.3.2 Support Vector Machine (SVM)

In this work, we apply SVM for finding the optimal hyperplane that separates the feature classes in the feature space [79].

First, we select the support vectors and find two parallel hyperplanes that separate the classes NSR and AF, such that the distance, also referred to as margin, between the hyperplanes is as large as possible. Then, the maximum-margin hyperplane

$$\mathbf{w}^\top \mathbf{x} = 0 \quad (4.10)$$

is the hyperplane that lies halfway between the classes, where \mathbf{w} is the normal vector to the hyperplane and \mathbf{x} is the point in the feature space.

The optimization problem is given by

$$\min_{\mathbf{w}, \xi_q} \left(\|\mathbf{w}\|^2 + C \sum_q^{N_{\text{feat}}} \xi_q \right) \quad (4.11)$$

subject to $y_q^{\text{cl}}(\mathbf{w}^\top \mathbf{x}_q) \geq 1 - \xi_q$ for $q = 1, \dots, N_{\text{feat}}$, where y_q^{cl} is the class label and $\xi_q > 0$ corresponds to the slack variable for the q -th data point in the feature space, and C is the cost of misclassifying. To solve (4.11), we perform a 5-fold cross-validation using the machine learning toolbox LIBSVM [80].

4.4.4 Real Data Results

4.4.4.1 Experimental Setup and Performance Metrics

The data was recorded as a pre-study to a larger data collection at the Onze Lieve Vrouwe Gasthuis (OLVG) in Amsterdam, Netherlands, using the video camera of an iPhone 5s, iPhone 6 Plus, and iPhone 6s Plus at a frame rate of 30 fps. The ethical

approval to conduct this pre-study was obtained from our collaboration partner. The duration of a measurement is 2 min and the sampling rate of the acquired PPG signal is 30 Hz. The measurements were visually checked and labeled by trained study staff as AF, NSR, or vibration (Vib) in the case of strong hand movement of the patient. We collected 20 measurements of AF, 294 of NSR, and 12 of Vib.

The time-domain features are computed over time windows of 20 s and the frequency-domain features are calculated for every 5 s segments with 80 % overlap and averaged over the same 20 s time windows. The classification is performed based on the features that are extracted from these time windows of 20 s duration.

We calculate the accuracy, sensitivity, specificity, and receiver operating characteristic (ROC) curve to evaluate the performance of the proposed method for each individual feature as well as for combinations of features.

4.4.4.2 Classification Results

The feature selection, indicates that using only two features are sufficient for AF detection. Table 4.1 shows the results of the best feature pairs in terms of sensitivity, specificity, and accuracy. The best single feature is the Shannon entropy (ShE) of peak location differences, which when combined with the median of peak rise height (mPRH) achieves a perfect classification accuracy of 100 %. Fig. 4.6 shows the ROC curve for the listed feature combinations.

Fig. 4.7 displays the feature space of the best feature pair and the separating line $\mathbf{w}_1^\top \mathbf{x}$ with decision equation

$$\mathbf{w}_1^\top \mathbf{x} = \begin{pmatrix} -0.54 \\ 0.045 \\ 1 \end{pmatrix}^\top \begin{pmatrix} 1 \\ \text{ShE} \\ \text{mPRH} \end{pmatrix} \underset{\text{NSR}}{\overset{\text{AF}}{\geq}} 0. \quad (4.12)$$

It also shows the separating line with decision equation

$$\mathbf{w}_2^\top \mathbf{x} = \begin{pmatrix} -3.83 \\ 0.267 \\ 1 \end{pmatrix}^\top \begin{pmatrix} 1 \\ \text{ShE} \\ \text{mPRH} \end{pmatrix} \underset{\text{Vib}}{\overset{\text{AF/NSR}}{\geq}} 0 \quad (4.13)$$

Table 4.1. Analysis of the classification performance of feature combinations (Comb) in terms of sensitivity, specificity, accuracy and the AUC of the ROC curve based on classified 20 s segments.

Feature Comb	Sensitivity	Specificity	Accuracy	ROC AUC
ShE+mPRH	1.000	1.000	1.000	1.000
LF+mPRH	0.850	1.000	0.991	0.998
ShE+nRMSSD	0.650	0.990	0.969	0.927

for the discrimination between AF, NSR and Vib. In this feature space, all three classes are linearly separable which implies perfect classification between AF and NSR.

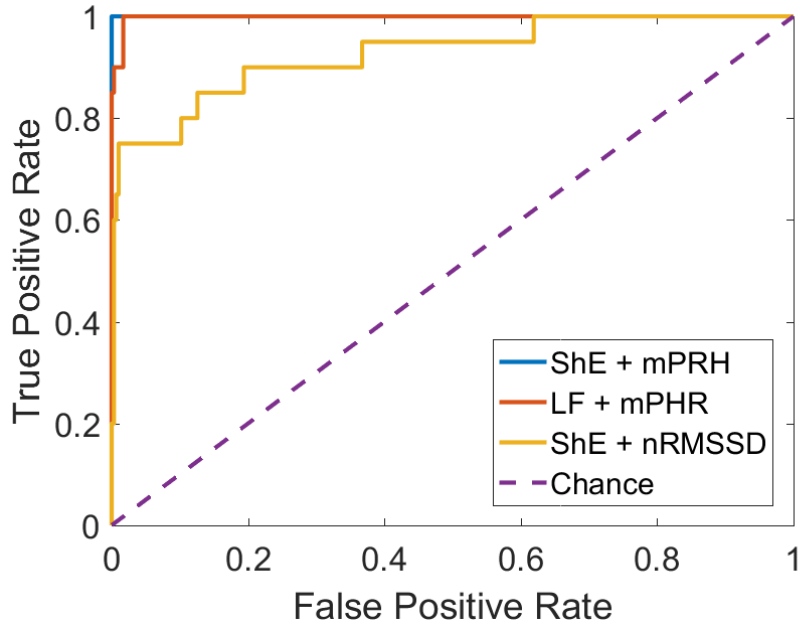


Figure 4.6. Receiver operating characteristic (ROC) curve of the best three feature pairs.

4.4.5 Discussion

The proposed method is applied to data from a pre-study and will be further evaluated on a larger number of measurements, which might alter our findings of the best feature combination. Hopefully, in future, this will lead to sufficiently large benchmark datasets for photoplethysmography-based AF detection.

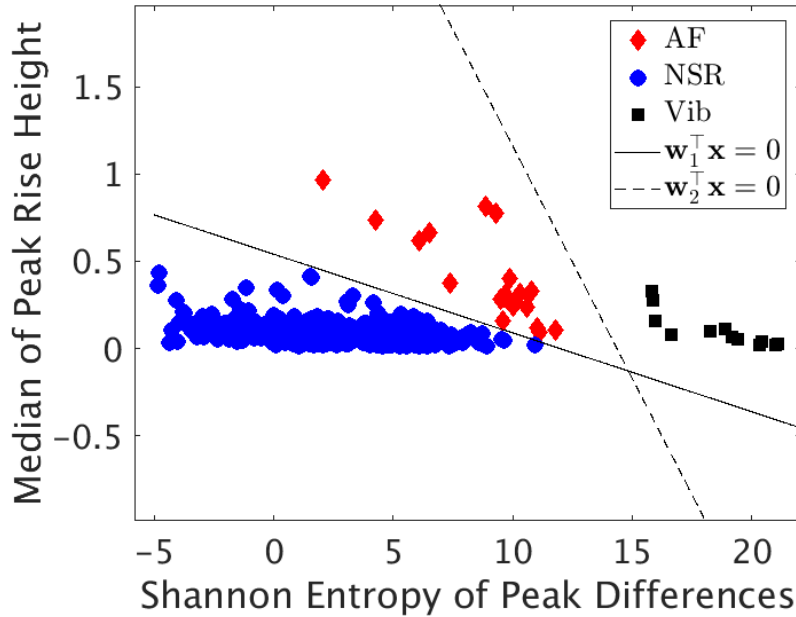


Figure 4.7. Feature space of the Shannon entropy of peak location differences and the median of peak rise height. The two lines separate AF from NSR and vibration-corrupted samples from good samples, respectively.

Variation in peak rise height in AF patients results from the variation in diastolic lengths that is present during AF. Longer diastolic time frames allow for more blood accumulation in the left ventricle which results in larger ejected blood volumes. The continuous variation in stroke volumes during AF is reflected by an increased variation in the peripheral pulse including small and relatively large peaks which can be detected by PPG.

We notice that the detection of AF should not solely be based on Shannon entropy and nRMSSD but can be improved by accompanying new features, such as the median of peak rise height or low-frequency energy of the peak location differences. Besides Shannon entropy and nRMSSD, the classic features to discriminate between AF and NSR, also kurtosis of the PPG signal spectrum has been recognized as a promising feature, especially in case of measurements with high signal-to-noise ratio (SNR). We suggest to investigate its potential on a larger dataset.

We assume that, for a larger amount of data, it may provide useful to combine more than two features and to calculate decision hyperplanes instead of lines. The proposed framework can easily be extended in this case. So far, we restricted ourselves to linear SVM for the simple reason that optimal classification was already possible. If the perfect separation of AF and NSR in the feature space is not given for a larger number

of measurements, we would suggest to perform a non-linear classification using what is called the kernel trick to map the features into high-dimensional spaces, which we successfully apply in Chapter 4.5.4.4 using SVR.

As a result of this work, a mobile application with extremely low computational costs could be implemented. Applying the proposed PPG acquisition, the application simply needs to calculate the presented subset of features, that best classifies AF and NSR, and form decisions based on (4.12) and (4.13).

Finally, a future extension of our work concerns recordings with bad finger placement. If the finger is moved on the camera lens during the measurement, the algorithm should reinitialize the most variant pixels that are used to acquire the PPG signal. Such a movement can be detected when the PPG signal abruptly jumps or is decaying.

4.5 Estimation of Blood Pressure and Arterial Stiffness

A method for the estimation of BP, PWV, and VAI based on a single PPG signal is presented in this section. Please note that the PPG signal for this method is acquired from a PPG sensor and not from the video camera of a smartphone. Fig. 4.8 summarizes the general principle of the algorithm. All stages of the algorithm are detailed in what is to follow.

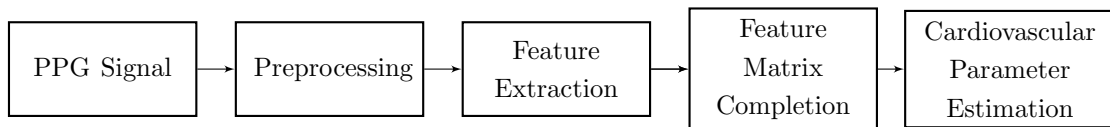


Figure 4.8. General principle of the algorithm to estimate cardiovascular parameters based on a single PPG signal.

4.5.1 Preprocessing

We acquire a PPG signal at a sampling frequency of 1 kHz and reduce high frequency noise by applying a finite impulse response (FIR) low-pass filter with a cut-off frequency $f_{c_1} = 30$ Hz and 15 filter coefficients. The PPG signals are standardized (z-score) by subtracting their mean and dividing by their standard deviation.

4.5.2 Feature Extraction

In total, a set of 83 features is extracted from the PPG, velocity of PPG (VPG), and acceleration plethysmogram (APG) waveforms as detailed in this section.

4.5.2.1 Features from the PPG Waveform

For each of the $n = 1, \dots, N_{\text{beat}}$ heartbeats, we calculate its energy,

$$E_n = \sum_{i=1}^{l_n} |p_n(i)|^2, \quad (4.14)$$

its Shannon entropy,

$$\text{Sh}E_n = - \sum_{i=1}^{l_n} p_n(i)^2 \log(p_n(i)^2), \quad (4.15)$$

as well as its kurtosis,

$$\text{Kurt}_n = \frac{\frac{1}{l_n} \sum_{i=1}^{l_n} (p_n(i) - \hat{\mu}_{p_n})^4}{\left(\frac{1}{l_n} \sum_{i=1}^{l_n} (p_n(i) - \hat{\mu}_{p_n})^2 \right)^2}, \quad (4.16)$$

where $\hat{\mu}_{p_n} = \frac{1}{l_n} \sum_{i=1}^{l_n} p_n(i)$.

To calculate further features based on characteristic points in the PPG waveform, we propose four different methods to find these characteristic points, three of which are based on Gaussian mixture models (GMMs) while the fourth uses the difference series. The modeling strategy exploits the well-known fact that the PPG waveform consists of two waves: the systolic and diastolic wave [4].

Method 1 models the systolic wave with a one-dimensional GMM with two components. The first component is centered at the maximal value of the PPG waveform corresponding to the systolic peak. An exemplary result is shown in Fig. 4.9.

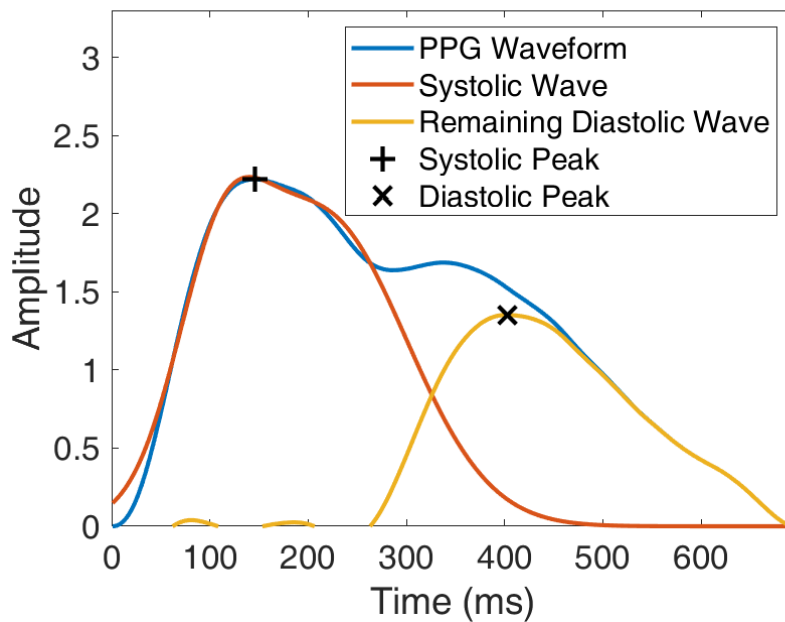


Figure 4.9. An example of a preprocessed PPG waveform with successful detection of the systolic and diastolic peak where the systolic wave is modeled by a one-dimensional GMM with two components and the diastolic wave is found as the difference to the PPG waveform (*Method 1*).

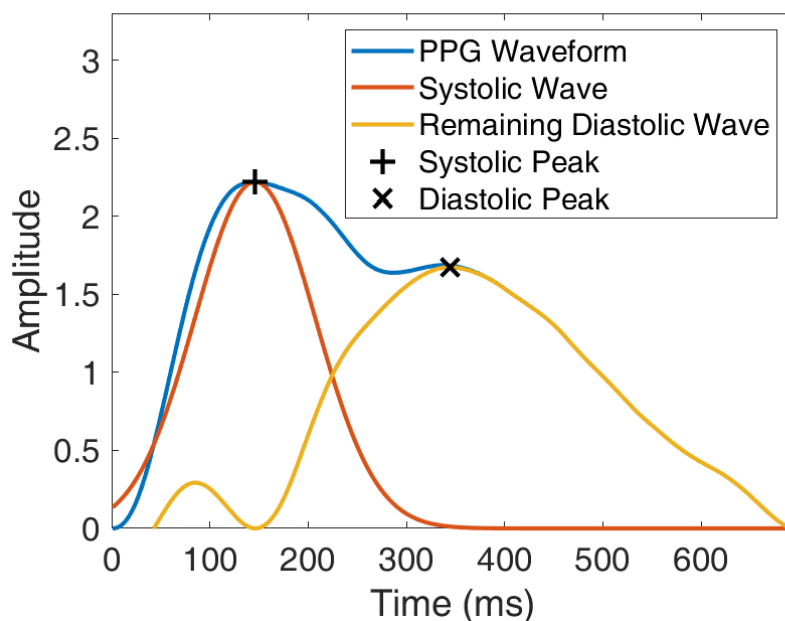


Figure 4.10. An example of a preprocessed PPG waveform with successful detection of the systolic and diastolic peak where the systolic wave is modeled by a one-dimensional GMM with two components but described only using the variance of the first component and the diastolic wave is found as the difference to the PPG waveform (*Method 2*).

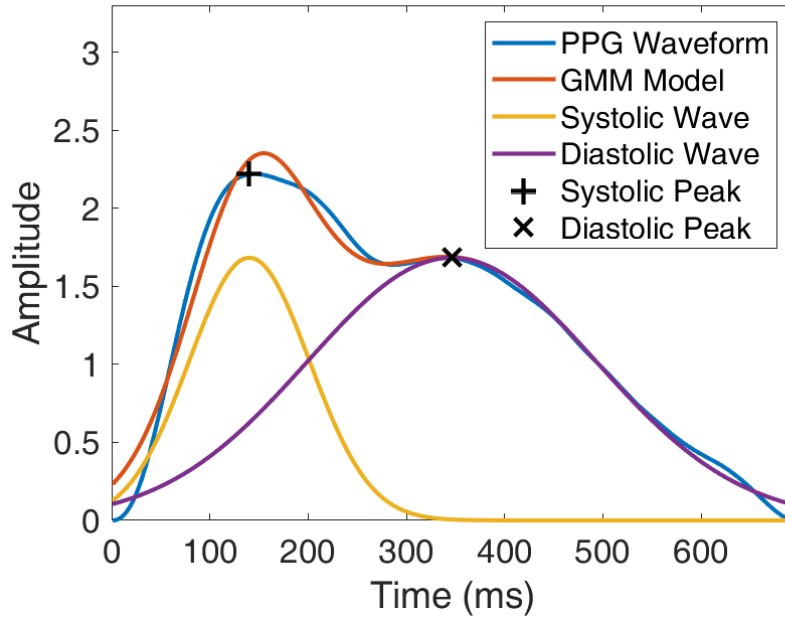


Figure 4.11. An example of a preprocessed PPG waveform with successful detection of the systolic and diastolic peak where both systolic and diastolic wave are modeled by a one-dimensional GMM with two components (*Method 3*).

Method 2 similarly fits a one-dimensional GMM with two components, where the first component is centered at the maximal value of the PPG waveform and corresponds to the systolic peak. Only the first component of the GMM is subtracted, and similarly to *Method 1*, the diastolic peak is defined as the maximal value of the residual waveform.

Method 3 directly models the systolic wave and diastolic wave as a one-dimensional GMM with two components. Here, the systolic peak and diastolic peak times are determined by location parameters of each component and their amplitudes are associated amplitudes in the original PPG waveform, see Fig. 4.11 for an example.

Method 4 analyzes the VPG and APG waveforms without using a GMM. The systolic peak is determined by the location of the first zero-crossing of the VPG, and the diastolic notch and diastolic peak are determined by the locations of the subsequent zero-crossings with a positive and negative value in the APG, respectively.

The locations and amplitudes of the estimated characteristic points serve as features. Further, for *Methods 1-3*, energy, Shannon entropy, and kurtosis are computed, analogously to (4.14)–(4.16), for the extracted systolic and diastolic waves.

4.5.2.2 Features from the VPG Waveform

From the VPG waveform we find four additional characteristic points termed according to the suggestion of Elgendi *et al.* [4] as the maximum slope peak in the systolic wave, the local minima slope in the systolic wave, the global minima slope in the systolic wave and the maximum slope peak in the diastolic wave. An example of a VPG waveform with successful detection of the characteristic points is shown in Fig. 4.12. Further features are obtained by computing the energy of the VPG waveform, its Shannon entropy, and kurtosis.

4.5.2.3 Features from the APG Waveform

The APG signal consists of five well-known characteristic points: a , b , c , d , and e , which are illustrated in Fig. 4.13. The points a to d can be attributed to the systolic wave, whereas point e describes the onset of the diastolic wave. Upon various tested heuristics, we report the most successful strategy, which searches for the largest extrema of the APG waveform and arrives at the correct order of points by exploiting the temporal structure that both minima must occur between the three respective maxima. An example of an APG waveform with successful detection of the characteristic points is shown in Fig. 4.13. Besides the location and amplitude of the characteristic points, we calculate the ratios b/a and $(b-c-d-e)/a$, the energy, Shannon entropy, and kurtosis of the APG waveform.

4.5.3 Feature Matrix Completion

In total, in this study, we extract $N_{\text{feat}} = 83$ features from a total number of $N_{\text{obs}} = 5202$ heartbeats and store the data in a large feature matrix. However, some features cannot be extracted for every heartbeat. For example, not all characteristic points in the PPG, VPG, or APG waveform can be found when the signal quality is too low or motion artifacts lead to large signal distortions. Overall, the amount of missing data is about 9 % with at least 65 % of the observations being available for each feature.

To overcome the problem of missing data, we propose to apply matrix completion methods to recover the missing entries of the feature matrix. As proven in Candès and Recht [81], for our setting the missing entries can be recovered, given that the feature matrix is sufficiently low rank. The low-rank assumption is well-justified in our case, because many features are highly correlated.

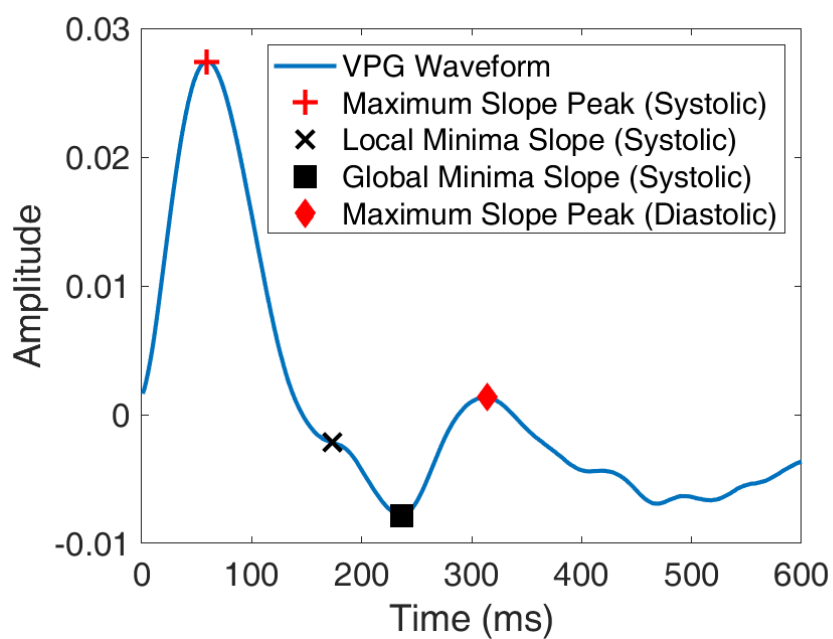


Figure 4.12. A VPG waveform with its four characteristic points.

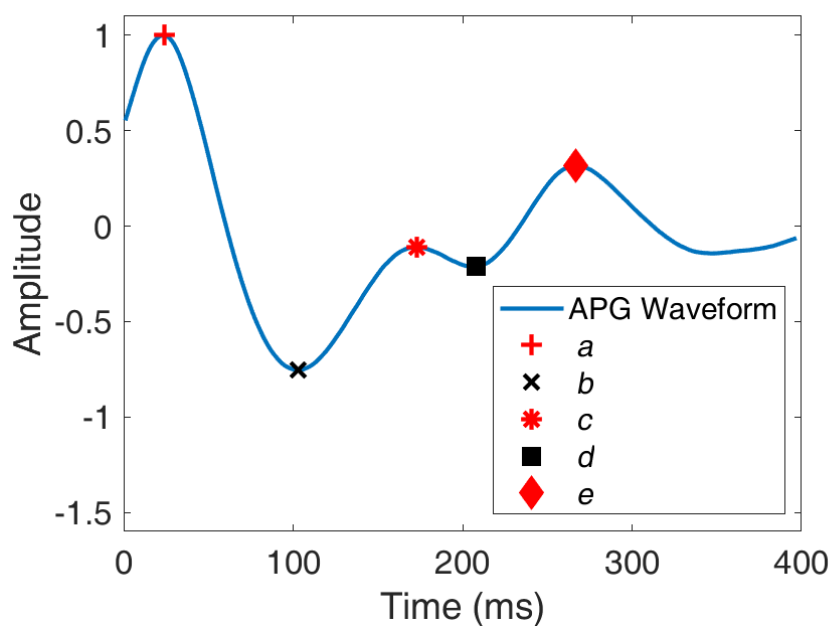


Figure 4.13. An APG waveform with its four characteristic points: *a*, *b*, *c*, *d*, and *e*.

To further investigate low-rank properties of the feature matrix \mathbf{X} , we apply principal component analysis (PCA) which shows that 24 principal components already describe 90 % of the variance, 31 components describe 95 %, and 40 components describe 99 %, see Fig. 4.14.

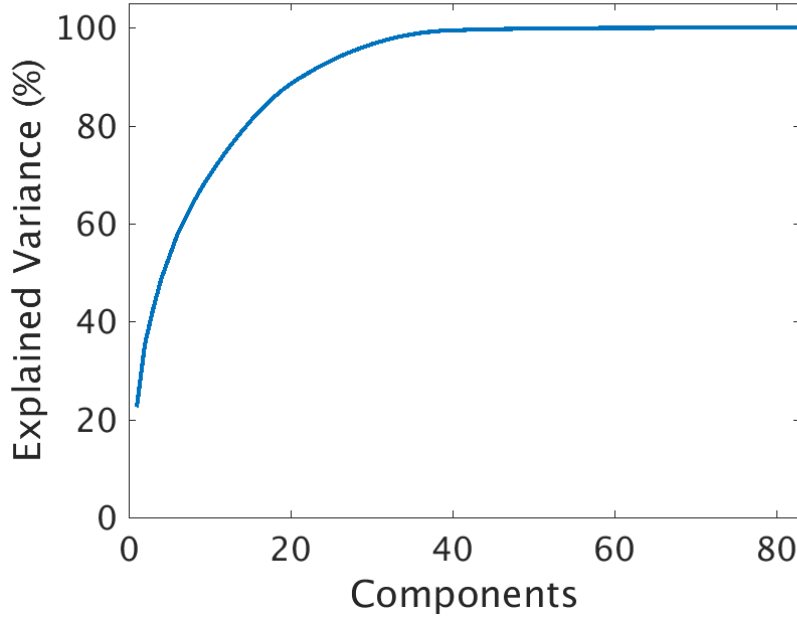


Figure 4.14. The explained variance (%) depending on the number of principal components of the feature matrix.

For matrix completion, we use the iterative hard-thresholded singular value decomposition (IHT-SVD), provided by Candès and Becker for non-commercial use [82], and recover the standardized feature matrix \mathbf{X} with N_{obs} rows (observations) and N_{feat} columns (features) by solving the following optimization problem:

$$\begin{aligned} & \text{minimize} && \text{rank}(\mathbf{X}) \\ & \text{subject to} && \|\tilde{\mathbf{x}} - M(\mathbf{x})\|_2 \end{aligned} \quad (4.17)$$

Here, $M(\mathbf{x})$ is a masking operator applied to the vectorized feature matrix $\mathbf{x} = \text{vec}(\mathbf{X})$, and $\tilde{\mathbf{x}}$ contains the successfully extracted features, see [82] for details.

4.5.4 Cardiovascular Parameter Estimation

The ultimate aim of this method is to accurately estimate cardiovascular parameters (dependent variables) based on a set of extracted features (independent variables).

Accordingly, in general, we model the dependent variable

$$\mathbf{y} = f(\mathbf{X}, \boldsymbol{\beta}) + \mathbf{v} \quad (4.18)$$

as a function of the independent variables $\mathbf{X} \in \mathbb{R}^{N_{\text{obs}} \times N_{\text{feat}}}$ and unknown parameters $\boldsymbol{\beta} \in \mathbb{R}^{N_{\text{feat}}}$. Model uncertainty is captured in \mathbf{v} , which is an independently distributed random variable.

In the case of linear regression, (4.18) reduces to

$$\mathbf{y} = \mathbf{X}\boldsymbol{\beta} + \mathbf{v}. \quad (4.19)$$

4.5.4.1 Least Squares Linear Regression

The most commonly used estimator is the ordinary least squares (OLS) that minimizes the sum of squared residuals. Its closed-form expression for the estimate of the unknown parameters $\boldsymbol{\beta}$ is¹

$$\hat{\boldsymbol{\beta}}_{\text{LSE}} = (\mathbf{X}^\top \mathbf{X})^{-1} \mathbf{X}^\top \mathbf{y}. \quad (4.20)$$

4.5.4.2 Robust Linear Regression

Robust M-estimators of the regression parameters can account for a certain amount of outliers by downweighting them in the objective function [84–86]. Joint M-Huber estimators [86] minimize Huber’s criterion,

$$\underset{\boldsymbol{\beta} \in \mathbb{R}^{N_{\text{feat}}}, \sigma \geq 0}{\text{minimize}} L_{\text{hub}}(\boldsymbol{\beta}, \sigma) = \frac{\alpha\sigma}{2N_{\text{obs}}} + \sum_{i=1}^{N_{\text{obs}}} \rho_{\text{hub}}\left(\frac{y_i - \mathbf{x}_i^\top \boldsymbol{\beta}}{\sigma}\right) \sigma \quad (4.21)$$

where

¹Since inverting $\mathbf{X}^\top \mathbf{X}$ can lead to undesirably large rounding errors, we use orthogonal-triangular (QR) decomposition and pivoting to obtain a stable solution [83].

$$\mathbf{x}_i = [x_i(1), x_i(2), \dots, x_i(N_{\text{feat}})]^\top \quad (4.22)$$

is the transposed i -th row (observation) of the standardized feature matrix \mathbf{X} , y_i is the corresponding reference value of the cardiovascular parameter, $\alpha > 0$ is a fixed scaling factor to obtain Fisher consistency when the error terms are independent and identically distributed (i.i.d.) Gaussian distributed, and ρ_{hub} is Huber's convex and differentiable loss function, defined as

$$\rho_{\text{hub}}(x) = \begin{cases} |x|^2, & \text{for } |x| \leq c_{\text{tune}} \\ 2c_{\text{tune}}|x| - c_{\text{tune}}^2, & \text{for } |x| > c_{\text{tune}} \end{cases}, \quad x \in \mathbb{R}, \quad (4.23)$$

where c_{tune} is a tuning parameter that trades off robustness and efficiency at a nominal Gaussian distribution. To compute Huber's M-estimates, we use the Minimization-Majorization-based algorithm, as implemented in the MATLAB function `hubreg.m` of the Robust Signal Processing Toolbox [86].

4.5.4.3 Support Vector Regression (SVR) with Linear Kernel

The basic idea of SVR [87] is to find a function $f(\mathbf{x}_i)$,

$$f(\mathbf{x}_i) = \mathbf{x}_i^\top \boldsymbol{\beta} + b_{\text{bias}} \quad \text{with } \boldsymbol{\beta} \in \mathbb{R}^{N_{\text{feat}}}, b_{\text{bias}} \in \mathbb{R}, \quad (4.24)$$

that has at most ε deviation from the observations y_i for all of the training data, and, at the same time, is as flat as possible [88]. Here, b_{bias} accounts for the bias. The flatness is obtained for small $\boldsymbol{\beta}$, and the convex optimization problem of the linear SVR is given by

$$\begin{aligned} & \text{minimize} && \frac{1}{2} \|\boldsymbol{\beta}\|^2 \\ & \text{subject to} && \begin{cases} y_i - \mathbf{x}_i^\top \boldsymbol{\beta} - b_{\text{bias}} \leq \varepsilon \\ \mathbf{x}_i^\top \boldsymbol{\beta} + b_{\text{bias}} - y_i \leq \varepsilon \end{cases} \end{aligned} \quad (4.25)$$

4.5.4.4 Support Vector Regression (SVR) with Nonlinear Kernel

As described in (4.18), in general, the cardiovascular parameters can have a nonlinear dependency on the extracted features, we make use of the kernel trick to approximate the nonlinear regression model $f(\mathbf{X}, \boldsymbol{\beta})$.

Using the dual problem form of the optimization problem

$$f(\mathbf{x}_i) = \mathbf{x}_i^\top \boldsymbol{\beta} + b = \sum_{j=1}^{N_{\text{obs}}} (\alpha_j - \alpha_j^*) \mathbf{x}_i^\top \mathbf{x}_j + b_{\text{bias}} \quad (4.26)$$

with

$$\boldsymbol{\beta} = \sum_{j=1}^{N_{\text{obs}}} (\alpha_j - \alpha_j^*) \mathbf{x}_j, \quad (4.27)$$

where α_i and α_i^* are Lagrangian multipliers, we can replace $\mathbf{x}_i^\top \mathbf{x}_j$ by the dot product of the transformed data points using a positively defined kernel function:

$$K(\mathbf{x}_i, \mathbf{x}_j) = \phi(\mathbf{x}_i)^\top \phi(\mathbf{x}_j). \quad (4.28)$$

Among different possible kernels, best performance was obtained for the radial basis function (RBF) or Gaussian kernel function

$$K(\mathbf{x}_i, \mathbf{x}_j) = \exp\left(-\frac{\|\mathbf{x}_i - \mathbf{x}_j\|^2}{2\sigma_K^2}\right), \quad (4.29)$$

where σ_K is the kernel scale, resulting in

$$f(\mathbf{x}_i) = \sum_{j=1}^{N_{\text{obs}}} (\alpha_j - \alpha_j^*) \exp\left(-\frac{\|\mathbf{x}_i - \mathbf{x}_j\|^2}{2\sigma_K^2}\right) + b_{\text{bias}} \quad (4.30)$$

in (4.24).

4.5.5 Experimental Results

4.5.5.1 Subjects

Eighteen subjects (13 males and 5 females) with no reported history of cardiovascular or cardiopulmonary disorders were recruited for this study. An informed consent was obtained from each subject after a detailed explanation of the investigation objective and the measurement procedure. The statistical characteristics of the study population and of the cardiovascular parameters are summarized in Table 4.2. For each cardiovascular parameter, the mean, STD, median, and range across all subjects are listed.

Table 4.2. Statistical characteristics of the study population

Characteristic		Value
Number of Subjects		18
Number of Measurements		42
Measurements per Subject		1–5
Sex [Total Measurements]	Female	5 [14]
	Male	13 [28]
Age (years)	Mean \pm STD	31.2 \pm 7.8
	Median, Range	28.5, 21–59
BMI (kg/m ²)	Mean \pm STD	22.1 \pm 2.4
	Median, Range	22.0, 18.4–27.5
Cardiovascular Parameter		Value
DBP (mmHg)	Mean \pm STD	81.8 \pm 10.8
	Median, Range	80, 58–115
SBP (mmHg)	Mean \pm STD	124.5 \pm 11.3
	Median, Range	124, 92–152
PWV (m/s)	Mean \pm STD	5.6 \pm 0.7
	Median, Range	5.5, 4.7–8.3
VAI (years)	Mean \pm STD	33.7 \pm 7.2
	Median, Range	33, 22–60

4.5.5.2 Study Protocol

The study was carried out in the biomedical laboratory of the Signal Processing Group (SPG) at Technische Universität (TU) Darmstadt in December 2017. In total, 42 measurements were taken from 18 different subjects. Three measurements had to be excluded because of bad signal quality resulting from sensor misplacement.

All subjects sat on a chair and were asked to relax and avoid body movement during the measurement. The total duration of one measurement session was about 20 min and the following two-stage experimental procedure was applied for each subject:

In the first stage, three physiological signals (ECG, PPG at the left wrist, and PPG at the left fore finger) were simultaneously acquired for a duration of 2 min using the PowerLab 26T from ADInstruments at a sampling frequency of 1 kHz, see Fig. 4.15. Both PPG sensors, i.e., the infrared (IR) Plethysmograph Finger Clip and the IR Plethysmograph Velcro Strap, use infrared light (950 nm) and are connected to the PowerLab 26T. Unfortunately, the signal quality of the wrist-worn PPG sensors was not sufficiently high and only the PPG signal from the finger clip could be used for further evaluation. To measure the ECG, three electrodes were placed at both subject's wrists and at the left ankle. Motion artifacts in the ECG signal were corrected with the multi-resolution thresholding method by Strasser *et al.* [89]. The detection of R-peaks in the QRS complex of the ECG was performed by applying the algorithm of Pan & Tompkins [90] using the implementation of Sedghamiz [91]. For the removal of high frequency noise caused by the differentiation, we apply an FIR low-pass filter with cut-off frequencies $f_{c_2} = 25$ Hz and 24 filter coefficients for the VPG and $f_{c_3} = 15$ Hz with 40 filter coefficients for the APG, respectively.

In the second stage, the cardiovascular reference parameters were measured with the Mobil-O-Graph PWA[®] which is a clinically approved device by I.E.M. GmbH. The device was validated in the year 2000 and fulfills the criteria of the British Hypertension Society (BHS) protocol, achieving a grade B for systolic blood pressure (SBP) and a grade A for diastolic blood pressure (DBP) [92]. The average differences were -2 ± 8 mmHg for SBP and -2 ± 7 mmHg for DBP. The device therefore also passed the American Association for the Advancement of Medical Instrumentation (AAMI) standard (the average differences have to be within 5 ± 8 mmHg). Ten years later, the device was again validated according to the criteria of the BHS as a twenty-four-hour BP measurement device [93], and achieved grade A for SBP and DBP leading to a final grade A/A. Thus, the device is "very accurate and with no error of clinical relevance" and is recommended for clinical use.



Figure 4.15. A subject during the recording of PPG and ECG signals.



Figure 4.16. A subject during the measurement with the reference device.

The Mobil-O-Graph PWA[®] works similar to an inflatable cuff device for BP, applying a cuff to the subject's upper arm, and exerting pressure onto the upper arm's brachial artery, see Fig. 4.16. It thereby performs a pressure pulse wave analysis (PWA) and measures a variety of cardiovascular parameters from which the DBP and SBP, the PWV, and the VAI serve as reference values for the photoplethysmography-based parameter estimation of the physiological signals. The PWA was conducted three times in a row. The duration of the second stage was about 15 min.

The study was approved by the Ethics Commission of TU Darmstadt on 24 April 2017. The reference number of the approval is EK 09/2017. Informed consent was obtained from all subjects before the experiment.

4.5.5.3 Evaluation Metrics

The median of the three consecutive measurements of the Mobil-O-Graph[®] serves as the reference for SBP, DBP, PWV, and VAI. The mean and STD of the estimation error w.r.t. these reference values are reported. We also evaluate the overall performance of the proposed methods according to the root-mean-squared error (RMSE),

$$\text{RMSE} = \sqrt{\frac{1}{N} \sum_{i=1}^N (\hat{y}_i - y_i^{\text{ref}})^2}, \quad (4.31)$$

the mean absolute error (MAE),

$$\text{MAE} = \frac{1}{N} \sum_{i=1}^N |\hat{y}_i - y_i^{\text{ref}}|, \quad (4.32)$$

and Pearson's correlation coefficient (CC),

$$\rho = \frac{\sum_{i=1}^N (\hat{y}_i - \mu_{\hat{y}})(y_i^{\text{ref}} - \mu_{y_{\text{ref}}})}{\sqrt{\sum_{i=1}^N (\hat{y}_i - \mu_{\hat{y}})^2} \sqrt{\sum_{i=1}^N (y_i^{\text{ref}} - \mu_{y_{\text{ref}}})^2}}, \quad (4.33)$$

where $\mu_{\hat{y}}$ and $\mu_{y_{\text{ref}}}$ are the sample means of \hat{y}_i and y_i^{ref} , respectively.

4.5.5.4 Feature Selection

To obtain the features that have the strongest impact in estimating the cardiovascular parameters, we apply sequential forward selection (SFS) [78], which sequentially adds features to an empty candidate set until the addition of further features does not increase the performance.

For comparison, additionally to the PPG features, we also evaluate features that require measuring an ECG signal. Based on the extracted temporal locations of the R-peaks in the ECG signal and the temporal locations of the characteristic points in the PPG, VPG, and APG signal, we calculate the PAT which is commonly used to estimate the BP [63, 67–71]. We compare several ways to estimate the PAT: using the R-peak and the systolic notch, or the systolic peak determined with each of the *Methods 1–4*, or alternatively, by using the R-peak and the maximum slope peak in the systolic wave from the VPG signal, see Fig. 5. In addition, for comparison, we evaluate meta features, such as the subject’s age, height, weight, and BMI and evaluate their contribution to the estimation of cardiovascular parameters.

Tables 4.4–4.11 summarize the first ten selected features for all physiological parameters. A distinction is made between the PPG only feature set, and the set that includes ECG and meta information on the subjects. We apply a wrapper-based selector and evaluate subsets by their predictive accuracy in terms of the RMSE using the SVR with a Gaussian kernel and a 5-fold cross-validation.

Note that, according to Table 4.4, the VPG features are important for modeling the glsdbp and from the first seven PPG-only features five are extracted from the VPG signal. For the glssbp, the best five features are extracted from the APG signal, see Table 4.5. As expected, the PAT is the overall most significant feature to estimate the glssbp. For the PWV and VAI, the three most significant features are the same and come from the APG signal, as listed in Tables 4.6 and 4.7.

4.5.5.5 Comparison between Feature Extraction Methods

Table 4.3 compares the performance of *Methods 1–4* for extracting features from the PPG waveform using the SVR with a Gaussian kernel and for static parameter estimation, as detailed in the following section. The results in Table 4.3 show that *Method 1* outperforms the others for all cardiovascular parameters and *Method 2* performs second best. The combination of all four methods produces more accurate results compared to using a single method.

Table 4.3. Statistical performance analysis of the proposed methods to extract features with static parameter estimation and only features from the methods

Method	Mean \pm STD	RMSE	MAE	CC
DBP: <i>Method 1</i>	-0.12 \pm 3.49	3.49	2.07	0.95
DBP: <i>Method 2</i>	-0.19 \pm 3.80	3.80	2.24	0.94
DBP: <i>Method 3</i>	-0.44 \pm 4.61	4.63	2.84	0.91
DBP: <i>Method 4</i>	-0.22 \pm 5.58	5.58	3.71	0.86
SBP: <i>Method 1</i>	-0.48 \pm 5.11	5.13	3.12	0.88
SBP: <i>Method 2</i>	-0.70 \pm 5.10	5.15	2.57	0.87
SBP: <i>Method 3</i>	-0.58 \pm 5.26	5.29	3.13	0.87
SBP: <i>Method 4</i>	-0.60 \pm 6.88	6.91	4.42	0.74
PWV: <i>Method 1</i>	0.04 \pm 0.30	0.31	0.14	0.92
PWV: <i>Method 2</i>	0.05 \pm 0.33	0.33	0.14	0.89
PWV: <i>Method 3</i>	0.06 \pm 0.39	0.39	0.16	0.85
PWV: <i>Method 4</i>	0.09 \pm 0.45	0.46	0.25	0.84
VAI: <i>Method 1</i>	0.34 \pm 3.16	3.18	1.51	0.92
VAI: <i>Method 2</i>	0.43 \pm 3.48	3.51	1.49	0.89
VAI: <i>Method 3</i>	0.51 \pm 4.00	4.03	1.78	0.85
VAI: <i>Method 4</i>	0.81 \pm 4.66	4.73	2.74	0.83

4.5.5.6 Static Parameter Estimation

Static parameter estimation refers to estimating the cardiovascular parameters for each heartbeat and then calculating the median over all heartbeat estimates for each measurement. This allows for a comparison to the estimates obtained from the reference device in terms of the evaluation metrics defined in (4.31)–(4.33).

As a benchmark comparison, we report estimates for each cardiovascular parameter that are computed with the linear model

$$\beta_1 \text{PAT} + \beta_0, \quad (4.34)$$

which is widely used to model the BP in a linear relation to the time it takes for a volume of blood to travel from the heart to a peripheral organ, neglecting the change in the arterial thickness and diameter with pressure variations [63]. One critical issue of this conventional method is the frequent calibration as the time delay is subject related and varies with the subject's heart rate. Thus, this regression model is subject specific and

requires individual calibration, which is in contrast to our proposed methods that are based on one regression model for all subjects. A further drawback of the conventional method is that the PAT requires an ECG to be acquired simultaneously.

For all cardiovascular parameters, the PAT using the R-peak in the ECG and the systolic peak in the PPG signal determined with *Method 4* achieved best results in terms of glsrms accuracy and was therefore reported.

The results for the static parameter estimation are listed in Tables 4.12–4.15, which also reports on the feature selection (top five and top ten features) for the proposed SVR with Gaussian kernel (SVR-G).

The linear regression model based estimators, i.e., linear least squares estimation (LSE-Lin), linear joint M-Huber estimation (Joint M-Huber-Lin) and SVR with linear kernel (SVR-Lin), achieve comparable poor results. Our proposed approach using the SVR with Gaussian kernel with only the best five PPG features and the subject-specific linear regression using the PAT already demonstrate reasonable performance (e.g. the STD of BP is less than 5 mmHg). Using the best 10 PPG features or more, the accuracy improves further up to the point of overfitting, see Section 4.5.5.8 for further discussion.

4.5.5.7 Continuous Parameter Estimation

Through matrix completion, we have all features available for all heartbeats and are able to estimate a value for each heartbeat. As an evaluation compared to the static reference values is not appropriate, we show an exemplary course of our DBP estimates in Fig. 4.17 to illustrate the performance of the proposed continuous parameter estimation in a dynamic parameter estimation setting.

Table 4.4. First ten features for DBP - PPG-only

#	Features for SVR Gaussian Kernel
1	Local Minima Slope Time in Systolic (VPG)
2	Maximum Slope Peak Time in Systolic (VPG)
3	b/a Ratio (APG)
4	Heart Rate in BPM
5	Maximum Slope Peak Amplitude in Diastolic (VPG)
6	Maximum Slope Peak Amplitude in Systolic (VPG)
7	Local Minima Slope Amplitude Systolic (VPG)
8	Systolic Peak Time (PPG) - <i>Method 1</i>
9	Systolic Peak Time (PPG) - <i>Method 2</i>
10	Diastolic Wave Shannon Entropy (PPG) - <i>Method 3</i>

Table 4.5. First ten features for SBP - PPG-only

#	Features for SVR Gaussian Kernel
1	Time of Point b (APG)
2	$(b - c - d - e)/a$ Ratio (APG)
3	Time of Point e (APG)
4	Normalized Amplitude of Point e (APG)
5	Normalized Amplitude of Point c (APG)
6	Heartbeat Duration
7	Shannon Entropy (APG)
8	Maximum Slope Peak Time in Systolic (VPG)
9	Systolic Time (PPG) - <i>Method 4</i>
10	Diastolic Wave Shannon Entropy (PPG) - <i>Method 3</i>

4.5.5.8 Training the Regression Model

Note that, in our proposed approach, the regression parameters of the regression models are subject independent, i.e., they are constant over all subjects. In this section, we compare results for different types of training of the model parameters:

- CV_0 (“all data”): the regression parameters are calculated once using all available data, no cross-validation (CV)
- CV_1 (“leave one measurement out”): the regression parameters are calculated

Table 4.6. First ten features for PWV - PPG-only

#	Features for SVR Gaussian Kernel
1	Normalized Amplitude of Point c (APG)
2	Normalized Time of Point e (APG)
3	Kurtosis (APG)
4	Systolic Time (PPG) - <i>Method 4</i>
5	Kurtosis (PPG)
6	Maximum Slope Peak Amplitude in Diastolic (VPG)
7	Maximum Slope Peak Time in Systolic (VPG)
8	Kurtosis (VPG)
9	Shannon Entropy (APG)
10	Diastolic Wave Shannon Entropy (PPG) - <i>Method 3</i>

Table 4.7. First ten features for VAI - PPG-only

#	Features for SVR Gaussian Kernel
1	Normalized Amplitude of Point c (APG)
2	Normalized Time of Point e (APG)
3	Kurtosis (APG)
4	Systolic Time (PPG) - <i>Method 4</i>
5	Maximum Slope Peak Time in Systolic (VPG)
6	Amplitude of Point e (APG)
7	Kurtosis (PPG)
8	Kurtosis (VPG)
9	Heart Rate in BPM
10	Systolic Time (PPG) - <i>Method 1</i>

for a specific measurement using no data from the same measurement but from the same subject and all other subjects.

- CV_2 (“leave one subject out”): the regression parameters are calculated for a specific measurement using no data from the measurement’s subject but from all other subjects.

The results are shown in Table 4.16 for static parameter estimation. All methods, except the benchmark “PAT-only” use SVR with a Gaussian kernel. Clearly, best results are obtained for CV_0 . For CV_1 , the standard deviation is low and results that are comparable to the benchmark method can be obtained. For CV_2 , an accurate

Table 4.8. First ten features for DBP - All Features

#	Features for SVR Gaussian Kernel
1	PAT by Systolic Notch Time (ECG-PPG)
2	Age of Subject
3	Height of Subject
4	Heart Rate in BPM
5	Kurtosis (VPG)
6	BMI of Subject
7	PAT by Systolic Peak Time in VPG (ECG-VPG)
8	Kurtosis (APG)
9	Weight of Subject
10	Diastolic Wave Energy (PPG) - <i>Method 3</i>

Table 4.9. First ten features for SBP - All Features

#	Features for SVR Gaussian Kernel
1	Weight of Subject
2	Height of Subject
3	Kurtosis (APG)
4	Systolic Time (PPG) - <i>Method 4</i>
5	Signal Energy (APG)
6	BMI of Subject
7	Maximum Slope Peak Amplitude in Systolic (VPG)
8	Age of Subject
9	Shannon Entropy (VPG)
10	Amplitude of Point a (APG)

estimation of the cardiovascular parameters is not possible. This can be attributed to the fact that the amount of data is not sufficient, i.e., more than 42 measurements from 18 subjects are required for a fully subject independent training.

4.5.6 Discussion

A strong motivation for our research is to provide an algorithm that accurately estimates cardiovascular parameters subject-independent and without any calibration from a single PPG signal. At this point in time, our estimation results are not yet good enough if no data is available from the respective subject. This is probably due

Table 4.10. First ten features for PWV - All Features

#	Features for SVR Gaussian Kernel
1	Age of Subject
2	Height of Subject
3	Local Minima Slope Time in Systolic (VPG)
4	BMI of Subject
5	PAT by Systolic Peak Time (ECG-PPG) - <i>Method 4</i>
6	Kurtosis (VPG)
7	Weight of Subject
8	Diastolic Wave Energy (PPG) - <i>Method 3</i>
9	Diastolic Wave Shannon Entropy (PPG) - <i>Method 3</i>
10	Systolic Wave Shannon Entropy (PPG) - <i>Method 1</i>

Table 4.11. First ten features for VAI - All Features

#	Features for SVR Gaussian Kernel
1	Age of Subject
2	Height of Subject
3	Local Slope Minima Time in Systolic (VPG)
4	BMI of Subject
5	PAT by Systolic Peak Time (ECG-PPG) - <i>Method 4</i>
6	Kurtosis (VPG)
7	Weight of Subject
8	Diastolic Wave Energy (PPG) - <i>Method 3</i>
9	Diastolic Wave Shannon Entropy (PPG) - <i>Method 3</i>
10	Systolic Wave Shannon Entropy (PPG) - <i>Method 1</i>

to the insufficient amount of training data. However, the estimation of cardiovascular parameters is already satisfying if there is at least one measurement and reference value of a subject available for training the regression model. As soon as all data is used to generate a regression model, however, over-fitting can occur for high-dimensional models, such as, the SVR with Gaussian kernel using a large number of features.

Another aim of our work is to provide an algorithm for permanent monitoring of cardiovascular parameters that can be easily implemented in wearable devices, as many fitness tracker and smartwatches already use the principle of photoplethysmography. In contrast to wearable PAT and ECG-based devices, such as, the Apple Watch Series 4 that has a built-in single-lead ECG sensor that only works by placing the finger on

Table 4.12. Statistical performance analysis of the static parameter estimation for the DBP

Method	Mean \pm STD (mmHg)	RMSE (mmHg)	MAE (mmHg)	CC
LSE-Lin (β_1 PAT + β_0) [63] ^{1,2}	-0.09 \pm 2.88	2.88	2.21	0.97
LSE-Lin (PPG-only)	0.03 \pm 5.78	5.78	4.58	0.85
Joint M-Huber-Lin (PPG-only)	-0.23 \pm 5.72	5.72	4.43	0.85
SVR-Lin (PPG-only)	0.02 \pm 5.79	5.79	4.56	0.85
SVR-G (Top 5 PPG feat.)	0.08 \pm 4.58	4.58	3.06	0.92
SVR-G (Top 10 PPG feat.)	-0.02 \pm 1.78	1.78	1.21	0.99
SVR-G (PPG-only)	-0.01 \pm 0.08	0.08	0.08	1.00

¹ is subject specific (requires individual calibration)

² best result of all PAT estimation methods (*Method 4*)

Table 4.13. Statistical performance analysis of the static parameter estimation for the SBP

Method	Mean \pm STD (mmHg)	RMSE (mmHg)	MAE (mmHg)	CC
LSE-Lin (β_1 PAT + β_0) [63] ^{1,2}	-0.14 \pm 3.48	3.48	2.94	0.94
LSE-Lin (PPG-only)	-0.13 \pm 6.44	6.44	5.04	0.82
Joint M-Huber-Lin (PPG-only)	-0.45 \pm 6.36	6.38	4.77	0.82
SVR-Lin (PPG-only)	-0.13 \pm 6.46	6.46	5.05	0.82
SVR-G (Top 5 PPG feat.)	-0.03 \pm 4.87	4.87	3.56	0.90
SVR-G (Top 10 PPG feat.)	-0.15 \pm 1.69	1.70	1.07	0.99
SVR-G (PPG-only)	0.00 \pm 0.08	0.08	0.08	1.00

¹ is subject specific (requires individual calibration)

² best result of all PAT estimation methods (*Method 4*)

the crown for thirty seconds, our method is potentially applicable for the continuous monitoring of BP, PWV, and VAI without the use of additional sensors. Based on our experiments, the proposed approach seems to be promising, as we could already show satisfactory results with features that were derived from a single PPG signal. However, a large study is necessary to rigorously verify this claim.

Recently, for a PAT-based method, Miao *et al.* [71] stated that linear regression models are preferred over nonlinear ones, because they are only slightly worse in performance, but are less demanding in terms of computational complexity. We have studied this proposal and have shown that SVR estimation with a nonlinear kernel can achieve far better results than its linear regression based counterpart for a single PPG-based

Table 4.14. Statistical performance analysis of the static parameter estimation for the PWV

Method	Mean \pm STD (m/s)	RMSE (m/s)	MAE (m/s)	CC
LSE-Lin (β_1 PAT + β_0) [63] ^{1,2}	0.00 \pm 0.11	0.11	0.09	0.95
LSE-Lin (PPG-only)	0.00 \pm 0.38	0.38	0.26	0.87
Joint M-Huber-Lin (PPG-only)	0.04 \pm 0.40	0.40	0.25	0.86
SVR-Lin (PPG-only)	0.00 \pm 0.38	0.38	0.26	0.87
SVR-G (Top 5 PPG feat.)	0.01 \pm 0.20	0.20	0.13	0.96
SVR-G (Top 10 PPG feat.)	0.01 \pm 0.07	0.07	0.03	1.00
SVR-G (PPG-only)	0.00 \pm 0.01	0.01	0.01	1.00

¹ is subject specific (requires individual calibration)

² best result of all PAT estimation methods (*Method 4*)

Table 4.15. Statistical performance analysis of the static parameter estimation for the VAI

Method	Mean \pm STD (y)	RMSE (y)	MAE (y)	CC
LSE-Lin (β_1 PAT + β_0) [63] ^{1,2}	-0.04 \pm 1.21	1.21	0.92	0.95
LSE-Lin (PPG-only)	0.03 \pm 4.09	4.09	2.86	0.86
Joint M-Huber-Lin (PPG-only)	0.36 \pm 4.26	4.28	2.69	0.85
SVR-Lin (PPG-only)	0.02 \pm 4.10	4.10	2.87	0.86
SVR-G (Top 5 PPG feat.)	0.13 \pm 2.39	2.39	1.59	0.95
SVR-G (Top 10 PPG feat.)	0.08 \pm 0.65	0.65	0.32	1.00
SVR-G (PPG-only)	0.00 \pm 0.05	0.05	0.05	1.00

¹ is subject specific (requires individual calibration)

² best result of all PAT estimation methods (*Method 4*)

method. On the other hand, for PAT-based methods that require an ECG, we also achieved reasonable results using a linear regression model and, hence, confirm the findings of Miao on our dataset.

For the implementation of our proposed algorithm into wearable BP devices, the Institute of Electrical and Electronics Engineers (IEEE) Standards Association has issued a wearable device standard for cuffless BP measuring devices and their corresponding objective performance evaluation in 2014, IEEE 1708-2014 [94]. The standard applies to all types of wearable BP measurement devices, including epidermal and unobtrusive BP devices, but is limited to devices that do not use a cuff during measurement. Although, several organizations have developed protocols for clinical validation of BP

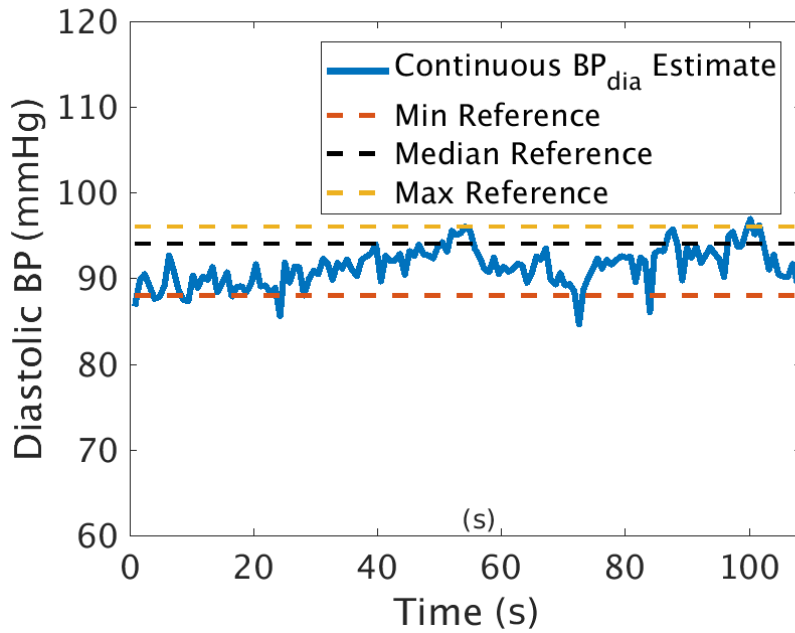


Figure 4.17. Illustration of a continuous estimation of DBP with three subsequently measured static reference values.

measuring devices over the past 30 years [95], including the AAMI, the BHS, the German Hypertension League, or the ESH, there is still no universal standard for the validation of BP measuring devices yet. However, several organizations are currently working on the development of a single universal standard to replace all other existing standards and protocols [96]. To evaluate the applicability of our proposed method or related future approaches, it would be highly useful to base performance evaluation on such a standardized procedure.

Finally, we would like to point out some limitations of our method. Our proposed method is limited in that the reference values were measured *a priori* and not continuously, the reference device has an inbuilt error that has to be considered, the measurements were taken under optimal measurement conditions, where the BP variability is very low, and the sample size of 18 subjects and 42 measurements is too small in order to draw general conclusions.

4.6 Summary and Conclusions

In this chapter, we have presented two different approaches to monitor the cardiovascular health using PPG signals.

Table 4.16. Statistical performance analysis of the different cross-validation methods with static parameter estimation

Method	Mean \pm STD	RMSE	MAE	CC
DBP: CV ₀ & PAT-only ¹	-0.65 \pm 10.50	10.52	7.78	0.19
DBP: CV ₀ & PPG-only	-0.01 \pm 0.08	0.08	0.08	1.00
DBP: CV ₀ & All Features	-0.01 \pm 0.08	0.08	0.08	1.00
DBP: CV ₁ & PAT-only ¹	-0.74 \pm 11.02	11.04	8.17	-0.15
DBP: CV₁ & PPG-only	0.20 \pm 8.98	8.98	6.91	0.58
DBP: CV ₁ & All Features	0.23 \pm 8.53	8.53	6.43	0.65
DBP: CV ₂ & PAT-only ¹	-0.78 \pm 11.66	11.68	8.66	-0.47
DBP: CV ₂ & PPG-only	0.73 \pm 11.38	11.40	8.44	-0.12
DBP: CV ₂ & All Features	0.71 \pm 11.18	11.20	8.04	-0.07
SBP: CV ₀ & PAT-only ¹	-0.58 \pm 10.11	10.13	7.58	0.16
SBP: CV ₀ & PPG-only	0.00 \pm 0.08	0.08	0.08	1.00
SBP: CV ₀ & All Features	0.00 \pm 0.08	0.08	0.07	1.00
SBP: CV ₁ & PAT-only ¹	-0.62 \pm 10.57	10.59	7.94	-0.13
SBP: CV₁ & PPG-only	-0.12 \pm 9.76	9.76	7.49	0.31
SBP: CV ₁ & All Features	-0.19 \pm 9.37	9.38	7.14	0.44
SBP: CV ₂ & PAT-only ¹	-0.57 \pm 10.94	10.95	8.21	-0.30
SBP: CV ₂ & PPG-only	0.75 \pm 11.58	11.60	8.69	-0.43
SBP: CV ₂ & All Features	0.76 \pm 11.48	11.51	8.59	-0.50
PWV: CV ₀ & PAT-only ¹	-0.02 \pm 0.69	0.69	0.45	0.05
PWV: CV ₀ & PPG-only	0.00 \pm 0.01	0.01	0.00	1.00
PWV: CV ₀ & All Features	0.00 \pm 0.01	0.01	0.01	1.00
PWV: CV ₁ & PAT-only ¹	-0.02 \pm 0.72	0.72	0.47	-0.82
PWV: CV₁ & PPG-only	0.12 \pm 0.71	0.72	0.43	-0.10
PWV: CV ₁ & All Features	0.11 \pm 0.68	0.69	0.40	0.23
PWV: CV ₂ & PAT-only ¹	-0.03 \pm 0.73	0.73	0.48	-0.78
PWV: CV ₂ & PPG-only	0.14 \pm 0.74	0.75	0.47	-0.33
PWV: CV ₂ & All Features	0.13 \pm 0.70	0.72	0.44	-0.08
VAI: CV ₀ & PAT-only ¹	-0.16 \pm 7.18	7.19	4.75	0.08
VAI: CV ₀ & PPG-only	0.00 \pm 0.05	0.05	0.05	1.00
VAI: CV ₀ & All Features	0.00 \pm 0.05	0.05	0.05	1.00
VAI: CV ₁ & PAT-only ¹	-0.22 \pm 7.47	7.48	4.96	-0.66
VAI: CV₁ & PPG-only	1.29 \pm 7.43	7.54	4.78	-0.11
VAI: CV ₁ & All Features	1.17 \pm 7.03	7.13	4.29	0.23
VAI: CV ₂ & PAT-only ¹	-0.30 \pm 7.54	7.55	5.05	-0.68
VAI: CV ₂ & PPG-only	1.52 \pm 7.72	7.86	5.26	-0.34
VAI: CV ₂ & All Features	1.38 \pm 7.33	7.46	4.81	-0.07

¹ is not subject specific

First, we have proposed a photoplethysmography-based AF detection algorithm using the video camera of smartphones. The approach combines an enhanced PPG acquisition with a new set of discriminating features and a classification procedure that selects the most significant features and outputs decision equations for the discrimination between AF and NSR. The proposed method achieved perfect classification on a set of 326 measurements that were taken at a clinical pre-study. The low computational complexity allows for a mobile application that could be implemented in future.

Further, we presented a novel approach for estimating BP, PWV, and VAI from a single PPG signal. Detailed information on the feature extraction from a PPG signal and its first and second order difference series, and on the recovery of missing features with matrix completion were given. The proposed estimation of cardiovascular parameters using a nonlinear SVR was compared to different linear regression estimators, including a PAT-based method. Furthermore, a feature selection approach was applied to identify a feature subset and to remove redundant and uninformative features. This allows for easier interpretability and reduces overfitting, which leads to enhanced generalization. The experimental results showed that the proposed method is able to perfectly estimate the cardiovascular parameters if the training data includes reference values of the respective measurement. Furthermore, the proposed method can still estimate the cardiovascular parameters with a sufficient accuracy if the training data includes reference values for the respective subject. In addition to that, we have provided potentially novel insights for the estimation of cardiovascular parameters. The results we obtained in this study are promising and warrant further investigation with a larger sample size to improve the estimation performance of cardiovascular parameters when no reference data of a person is available. For future research, we suggest to validate and further improve the proposed method by using continuous reference measurements of the cardiovascular parameters.

Chapter 5

Conclusions and Future Work

In this thesis, we have proposed photoplethysmography-based methods to solve current biomedical signal processing problems in the area of heart rate estimation during physical activity using multiple PPG signals at the wrist, in the area of atrial fibrillation (AF) detection using a PPG signal recorded from a video camera of a smartphone, and in the area of estimating blood pressure (BP), pulse wave velocity (PWV), and vascular age index (VAI) from a single PPG signal.

In particular, we have presented two computationally efficient approaches to monitor a subject's heart rate in real-time during physical activity using PPG and acceleration signals. The first approach reduces the influence of motion artifacts in the PPG signal with adaptive filters and combines multiple adaptive filter outputs to enhance the spectral quality. The second approach applies correlation-based fundamental frequency indicating functions, spectral combination, and harmonic noise dampening. Both approaches rely on simple frequency-domain trackers and demand low computational cost and memory requirements, but are comparable in terms of accuracy to computationally intensive state-of-the-art methods on a benchmark data set.

In the context of cardiovascular health monitoring, we have presented a photoplethysmography-based approach to detect AF using the video camera of a smartphone. The approach includes a new acquisition method, the extraction of new discriminating features, the application of feature selection and yields simple decision equations for the discrimination between AF and normal sinus rhythm (NSR) that achieved perfect detection of AF at a clinical pre-study. Furthermore, we have presented an approach for estimating BP, PWV, and VAI from a single PPG signal. For this, a large number of features is extracted from the PPG signal and its first and second order difference series, followed by the recovery of missing features using matrix completion. The proposed estimation of cardiovascular parameters using a nonlinear support vector regression (SVR) was thoroughly evaluated and compared a state-of-the-art approach using the electrocardiogram (ECG). The experimental results showed that the proposed method is able to estimate the cardiovascular parameters with sufficient accuracy if the method's calibration includes the respective subject. In addition to that, we have provided potentially novel insights for the estimation of cardiovascular parameters.

In Section 5.1, we summarize our findings and draw conclusions about the problems considered in this thesis. An outlook regarding potential future work is given in Section 5.2.

5.1 Conclusions

5.1.1 Heart Rate Estimation

One of the major research objectives of this thesis has been the development of a heart rate estimation method during physical activity that has high accuracy, low computational complexity, and low memory requirements. Two different approaches that address this research objective have been presented in Chapter 3. The presented methods have been evaluated on a reference data set and show high accuracy compared to other methods. In contrast to many other published methods, which have been described in such a way that reproduction is either impossible or very difficult, the presented approaches in this thesis are based only on simple signal processing functions and are therefore easy to understand, reproduce, and implement, which promotes further research in this area. Since the accuracy of the most accurate published algorithms on the data set of the IEEE Signal Processing Cup 2015 now lies at a sufficiently good level around one beat per minute (BPM), our methods have made a contribution to the development of a simple and computational efficient algorithm to estimate the heart rate during physical activity.

5.1.2 Cardiovascular Health Monitoring

Another major research aim of this thesis has been the detection of AF using the PPG signal recorded from a video camera of a smartphone with high reliability and low computational complexity. The proposed approach that addresses this research objective has been presented in Chapter 4.4. The evaluation on a clinical pre-study showed that AF and NSR could perfectly be classified by only using two of the presented features. As the proposed method includes many more features, it has the potential to perform well on a larger clinical study.

A further major research aim of this thesis has been the estimation of BP, PWV, and VAI from a single PPG signal. The proposed approach that addresses this research objective has been presented in Chapter 4.5. The experimental results showed that the

proposed method is able to estimate the cardiovascular parameters, and the obtained results are promising and warrant further investigation with a larger sample size to improve the estimation performance of cardiovascular parameters when no reference data of a person is available.

5.2 Challenges and Future Work

5.2.1 Heart Rate Estimation

Especially important for the future improvement and extension of algorithms for estimating the heart rate during physical activity is the expansion to a universal test data set that is much larger and more meaningful than the data set currently used as a reference data set by Zhangs *et al.* [15]. In general, more measurements from several different physical activities should be taken by a much larger total number of subjects, so that less subject-specific methods can be developed and evaluated for different activities. Ideally, a benchmark data set should also include measurements that are taken with different wavelengths and number of PPG channels to assess the impact of such parameters on the estimation accuracy. This expanded data set with a large number of physical activities would then also make it interesting to develop an automatic recognition system for physical activities, which is already available for many commercially available devices, but which has so far only been studied to a limited extent in academic research. Furthermore, future research could also focus more on the assessment of the signal quality of a PPG signal and develop standards for signal quality metrics that would be supportive for further development of PPG algorithms. In general, it would be desirable to create a universally accepted framework for performance evaluation in order to be able to compare not only the accuracy but also the execution speed and complexity of photoplethysmography-based heart rate estimation methods independently of the platform.

Motion artifacts, especially impulsive noise, that occur during sports with non-periodic movements, such as yoga or martial arts, and racket sports, such as tennis or badminton, are particularly difficult to model, remove, or attenuate from a PPG signal. In these cases, the signal-to-noise ratio (SNR) is consistently very low and removing the noise without damage to the desired signal components is critical so that a reliable estimation of the heart rate is only possible to a limited extent and requires further research. A possible alternative could be additional PPG sensors at a location of the

body where the movements are less impulsive or the body part has higher blood circulation, e.g. the racket player could put an additional wearable sensor around the ankle or upper arm rather than at the wrist where he holds the racket. The additional wearable sensor could then be connected to the actual wearable via Bluetooth or ANT. Challenging artifacts also occur during water sports, as water can penetrate between the sensor and the skin, resulting in a drastic decline of the SNR.

5.2.2 Cardiovascular Health Monitoring

A topic of large current interest to manufacturers of photoplethysmography-based wearables is the development of trackers for heart rate variability (HRV) and HRV related parameters. With the help of HRV and derived features, cardiac arrhythmias could be detected or at least the wearer could be advised to consult a physician if the device is certain to have detected abnormal heartbeat patterns. Even in developing countries, where the detection rates of abnormal heartbeat patterns are much lower than in industrial countries, simple medical devices are imaginable thanks to the technology of photoplethysmography. Since the costs for an ECG are more expensive, cheap PPG sensors could help people in developing countries to monitor their health and identify risks, whether with a wearable or a smartphone, as we presented in Chapter 4.4 using an AF detection algorithm.

A further important future research direction is to detect and to distinguish other forms of cardiac arrhythmia, such as, premature atrial contractions (PACs), premature ventricular contractions (PVCs), or atrial flutter. The difficulty in performing such research lies in acquiring ground truth, i.e., expert labeled data sets for these rather rare cardiac arrhythmia. This is especially difficult because doctors who are able to detect such arrhythmia, e.g., based on a synchronously acquired ECG, are extremely busy, and the use of such personal data is strictly regulated.

A rather practical challenge is the variety of different camera systems in smartphones. Since the arrangement of the flash and the video cameras as well as their size, resolution, and quality differ from smartphone manufacturers, it is recommended to extend the measurements to a larger set of different smartphones in order to ensure a device-independent design of the algorithms.

One challenge with the calculation of the VAI is that manufacturers of commercially available measurement devices, such as the Mobil-O-Graph from I.E.M. GmbH, do not provide any details about their calculation of this value. Therefore, a general model

based on the waveform of the PPG signal should be defined for the VAI. Furthermore, the measurements for BP, PWV, and VAI were taken under optimal measurement conditions at rest, where the variability is very low and movement-related signal distortions are hardly present. A performance analysis for sub-optimal conditions would help for a reliability evaluation of the results. For this, a general standard for the signal quality of a PPG signal would be beneficial.

Based on our experiments in Chapter 4.5.5, the proposed approach to estimate BP, PWV, and VAI seems to be promising, as we could already show satisfactory results with features that were derived from a single PPG signal. However, a large study is necessary to rigorously verify this claim. For future research, we suggest to validate and further improve the proposed method by using continuous reference measurements of the cardiovascular parameters.

In terms of future methods, we suggest to explore nonlinear sparse and robust regression based methods, and to combine them with robust matrix completion. In this way, it may be possible to accurately estimate cardiovascular parameters, even for lower quality signals, such as the ones measured at the wrist, which we currently excluded in our study. Furthermore, when combined with signal quality information, a quality dependent monitoring of cardiovascular parameters could be implemented that outputs an estimate as soon as a sufficient number of high-quality heart beats has been observed.

In general, it is imaginable that in the future, new wearables will be able to measure BP, vascular stiffness, or other cardiovascular parameters in addition to the heart rate and HRV in order to provide the user with more information about current health conditions. However, such algorithms should first be intensively evaluated so that a user does not draw the wrong conclusions if the device shows, for example, an erroneously extremely high or low blood pressure. For non-clinical service providers, the risk of user complaints is therefore high and the proper handling and legal limits for these devices should be clearly defined.

Appendix

A.1 Summaries of Other Publications

This chapter summarizes the publications that have been produced during the period of doctoral candidacy on topics other than photoplethysmography.

A.1.1 Robust Nonlinear Causality Analysis

This section summarizes the publication

- T. Schäck, M. Muma, M. Feng, C. Guan and A. M. Zoubir, “Robust Nonlinear Causality Analysis of Nonstationary Multivariate Physiological Time Series”, *IEEE Transactions on Biomedical Engineering*, vol. 65, no. 6, pp. 1213–1225, June 2018.

An important research area in biomedical signal processing is that of quantifying the relationship between simultaneously observed time series and to reveal interactions between the signals, for example in the case of non-invasive brain activity measurements, such as electroencephalography (EEG) or functional magnetic resonance imaging (fMRI), where the neural connectivity is characterized [97–106]. Also in cardiological studies one is interested, for example, in the relation between cardiovascular and cardiorespiratory data [107–111]. Since biomedical signals are potentially non-stationary and the measurements may contain outliers and artifacts, we introduce a robust time-varying generalized partial directed coherence (rTV-gPDC) function in [112] based on a robust estimator of the time-varying autoregressive (TVAR) and time-varying moving-average (TVMA) parameters, which is capable of revealing directed interactions between signals.

A.1.1.1 State of the Art

A traditional approach to analyze the relation between multivariate biomedical signals is to use the coherence function [113], the partial coherence [114], or approaches based

on time-varying extensions of the coherence function [111,115]. However, the coherence function is not a directional measure, i.e., it does not provide the direction of the information flow. Therefore, several techniques based on linear multivariate autoregressive (MVAR) models have been proposed to quantify causality in the frequency domain. One of the most frequently applied methods is the directed transfer function (DTF), that was introduced by Kaminski and Blinowska [116] as a multivariate measure of the intensity of activity flow in brain structures.

A further multivariate approach for the estimation of causality between time series is the directed coherence (DC) [98,117]. The partial directed coherence (PDC) and the re-examined definition of the generalized partial directed coherence (gPDC) were introduced by Baccalá *et al.* [118,119]. The PDC is a conceptual generalization of the DC, whereas the gPDC is a natural generalized definition of the PDC. It allows to perform a multivariate analysis that is capable of detecting the interactions between two signals after removing the contribution of all the other signals. gPDC also has the advantage of being scale invariant and more accurate for short time series as compared to the PDC. Thus, the gPDC is able to distinguish between direct and indirect connections.

To overcome the limitation of stationarity, Milde *et al.* [120] presented a technique to estimate high-dimensional TVAR models for interaction analysis of simulated data and high-dimensional multi-trial laser-evoked brain potentials (LEP). Systematic investigations on the approach to use a Kalman filter for the estimation of the TVAR models were performed by Leistriz *et al.* [121]. A mathematical derivation of the asymptotic behaviour of the gPDC has been presented by Baccalá *et al.* [122]. Omidvarnia *et al.* [123] modified the time-varying generalized partial directed coherence (TV-gPDC) method by orthogonalization of the strictly causal multivariate autoregressive model coefficients. The generalized orthogonalized partial directed coherence (gOPDC) minimizes the effect of mutual sources and was applied on event-related directional information flow from flash-evoked responses in neonatal EEG. All the above-mentioned multivariate measures rely on the concept of Granger causality between time series [124] and can be interpreted as frequency-domain representations of this very popular concept of causality.

However, a severe challenge in estimating the parameters of MVAR models is the sensitivity of classical estimators towards artifacts or outliers in the measurements [85,89,101,125–130]. The presence of artifacts or outliers was frequently reported, e.g., in fMRI [131] or ECG [89] measurements. Researchers often must exclude contaminated signal parts [101,125,126,128–130] which can lead to a significant loss of data. Finally, since MVAR models are bound to describe linear relations between time series, they

fail to detect nonlinear causalities, which have been reported for a variety of biomedical signals [132–134].

A.1.1.2 Contributions

Our contributions are as follows:

- We propose a new directed coherence measure called the robust time-varying generalized partial directed coherence (rTV-gPDC). The parameters of the generalized partial directed coherence (gPDC) are estimated using a Kalman filter. In this way, the assumption of stationarity is dropped.
- Based on robust statistics [85,135,136], we introduce a computationally attractive one-step reweighting algorithm that is incorporated into the Kalman filter to handle artifacts.
- We adapt a method by Chowdhury [137] to approximate the often unknown nonlinear function with the help of a family of piece-wise linear functions using a TVMA model that captures causalities that cannot be explained by the TVAR model, i.e., are nonlinear. With this TVMA model, we extend the gPDC to nonlinear causality patterns to reveal nonlinear relations between multivariate time series.
- We evaluate our method numerically both in terms of accuracy and robustness, and compare it to an existing method [138]. Furthermore, we apply our method to clinically collected traumatic brain injury (TBI) data and display the interactions between intracranial pressure (ICP), arterial blood pressure (ABP), and brain tissue oxygenation level (PtiO₂) signals.

A.1.2 Eyelid Localization in Videokeratoscopic Images

This section summarizes the publication

- T. Schäck, M. Muma, W. Alkhalidi and A. M. Zoubir, “A Procedure to Locate the Eyelid Position in Noisy Videokeratoscopic Images”, *EURASIP Journal on Advances in Signal Processing: Nonlinear Signal and Image Processing - A Special Issue in Honour of Giovanni L. Sicuranza on his Seventy-Fifth Birthday*, vol. 2016, no. 1, pp. 136 (13 pages), Dez. 2016.

A keratoscope is an ophthalmological instrument that allows for non-invasive imaging of the topography of the human cornea, which is the outer surface of the eye [139]. The cornea is the largest contributor to the eye's refractive power and its topography is of critical importance when determining the quality of vision and corneal health. For example, astigmatism may occur if the cornea has an irregular or toric curvature. Videokeratoscopy allows for studying the dynamics of the corneal topography [140–143].

Another important application of videokeratoscopy is the analysis of tear film stability in the inter-blink interval (IBI). Ocular discomfort can be caused by dry spots which occur if the tear film is destabilized. The tear film build-up and break-up times can be estimated from videokeratoscopic images if the data acquisition rate is sufficiently high [144–147]. Videokeratoscopy is also involved in the study of the dynamic response of the corneal anterior surface to mechanical forces. These mechanical forces are exerted by the eyelids during horizontal eye movements in downward gaze. More information on the applications of high-speed videokeratoscopy (HSV) can be found in [148].

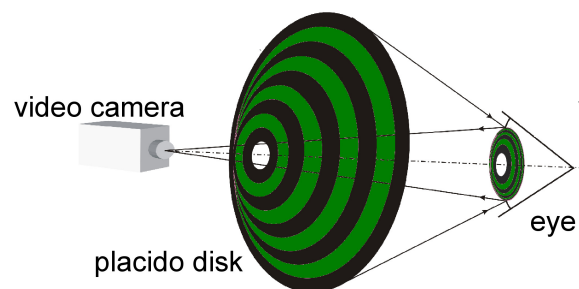


Figure 1. Principle of videokeratoscopy [149]. Illuminated rings of pre-defined geometry are projected onto the cornea.

Figure 1 displays the principle of videokeratoscopy. Concentric rings are projected by a Placido disk onto the cornea which is covered by a tear-film. The reflection of the ring pattern is recorded by a video camera and analyzed to produce contour maps and 3D reconstruction of the corneal surface. Equally-spaced symmetric reflections from the corneal surface would indicate perfect vision, while distortions in the ring pattern represent aberrations.

One of the first high-speed videotopographic methods could record four images per second [150]. The Contact Lens and Visual Optics Laboratory (CLVOL) at the School of Optometry, Queensland University of Technology in Brisbane, Australia, has developed a high-speed videokeratoscope which can operate at sampling frequency of 50 Hz due to a combination of a commercially available videokeratoscope and an additional



Figure 2. A videokeratoscopic image.

dynamic image acquisition system [148]. Only at this high sampling rate it is possible to reasonably study the period of tear film behavior immediately before and after a blink. All videokeratoscopic data used in this paper was recorded at CLVOL. An example of a videokeratoscopic image is given in Fig. 2.

A.1.2.1 State of the Art

Eyelid localization in images is an active area of research, and important applications are, for example, iris recognition systems, and drowsiness detection [151–154]. To the best of our knowledge, the case of videokeratoscopic images is still an open research question. In fact, even today, the very time-consuming manual selection of candidate pixels followed by a parametric fit of a parabola in the least squares sense is still the routine operation.

In videokeratography, the contrast of the images is low and edges are potentially blurred, which makes edge detection [155, 156] inapplicable. Furthermore, severe occlusions especially by the upper eyelashes and their shadows may occur, and the Placido disk ring pattern produces strong gradients in all directions. Additionally, it is evident that the upper eyelid edge is much more difficult to detect than the lower eyelid because it is severely affected by eyelashes and their shadows.

In addition to the difficulty of localizing the image's region of interest, videokeratography for eye research imposes strong requirements concerning the accuracy of the model of the eyelid edge. The conventional approach to fit a parabola does not always provide

a sufficiently accurate approximation to the real curvature. In some images, a non-symmetrical model may be necessary to describe the entire eyelid including the parts covering the sclera.

A.1.2.2 Contributions

Our contributions are as follows:

- We propose a complete framework to automatically and robustly determine the eyelid position in high-speed videokeratoscopic images. This methodology allows for automatic localization of the eyelid edges and is applicable to replace the currently used time-consuming manual labeling approach, while maintaining its accuracy.
- We propose a nonlinear filter method to remove eyelashes from videokeratoscopic images based on the gradient direction variance (GDV) and a wavelet-based method which adapts the procedure of [153] to videokeratoscopic images.
- Based on morphological operations and active contours, we introduce an image segmentation approach to detect eyelid edge pixels in videokeratoscopic images. Subsequently, a verification procedure reduces this set of pixels to those pixels that are likely to contribute to an accurate fit of the eyelid edge.
- We propose and evaluate new linear and nonlinear eyelid curvature models as an alternative to the conventional parabola.
- Based on M-estimation [85, 135, 136], we introduce a robust algorithm to fit a parametric model to a set of eyelid edge candidate pixels. In this way, we account for outliers in the set of candidate pixels. These are present due to the very low contrast of videokeratoscopic images and because of occlusions caused by eyelashes. Alternatively, we discuss a robust fit of a parabola by the Hough transform.
- We evaluate the complete framework by providing a real-world data performance analysis on high-speed videokeratoscopic images.

A.1.3 Signal Processing Projects at TU Darmstadt

This section summarizes the publication

- T. Schäck, M. Muma and A. M. Zoubir, “Signal Processing Projects at Technische Universität Darmstadt: How to Engage Undergraduate Students in Signal Processing Practice”, *IEEE Signal Processing Magazine*, vol. 34, no. 1, pp. 16–30, Jan. 2017.

Hands-on education in signal processing has a long-standing tradition (e.g., [157–161]), and its importance, given the complexity of today’s engineering problems, is undisputed. We share our experience on integrating hands-on practice into formal engineering education at Technische Universität (TU) Darmstadt, where we believe that it is essential to provide undergraduate students with hands-on signal processing opportunities right from the starting-point of their studies until graduation.

A.1.3.1 Contributions

Our contributions are as follows:

- We share our experience on integrating signal processing hands-on into formal engineering education at TU Darmstadt, hope to inspire our colleagues, and perhaps trigger new hands-on projects by sharing our insights.
- We illustrate how we involve students in interdisciplinary research by an example of a cooperation between the Signal Processing Group (SPG) and the Department of Psychology.
- We present our diverse signal processing laboratories and the opportunities they offer for our students.
- We illustrate how we utilize student competitions, such as the IEEE Signal Processing Cup, to stimulate innovation and collaboration between graduate and undergraduate students.
- We give practical remarks on some fundamental aspects that we have found to be important for successful design projects.

List of Acronyms

AAE	average absolute error
AAEP	average absolute error percentage
AAMI	American Association for the Advancement of Medical Instrumentation
ABP	arterial blood pressure
AD	adaptive filter
AF	atrial fibrillation
APG	acceleration plethysmogram
AS-LMS	adaptive step-size last mean squares
AUC	area under curve
BHS	British Hypertension Society
BImp	bioimpedance
BMI	body mass index
BP	blood pressure
BPM	beats per minute
CC	Pearson's correlation coefficient
CE	computationally efficient
CLVOL	Contact Lens and Visual Optics Laboratory

CV	cross-validation
CVD	cardiovascular disease
DBP	diastolic blood pressure
DC	directed coherence
DTF	directed transfer function
ECG	electrocardiogram
EEG	electroencephalography
EEMD	ensemble empirical mode decomposition
ESH	European Society of Hypertension
FFT	fast Fourier transform
FIR	finite impulse response
fMRI	functional magnetic resonance imaging
fps	frames per second
GDV	gradient direction variance
GMM	Gaussian mixture model
gOPDC	generalized orthogonalized partial directed coherence
gPDC	generalized partial directed coherence
HF	high frequency
HRV	heart rate variability
HSV	high-speed videokeratotomy

IBI	inter-blink interval
ICA	independent component analysis
ICP	intracranial pressure
IEEE	Institute of Electrical and Electronics Engineers
IHT-SVD	iterative hard-thresholded singular value decomposition
IR	infrared
JOSS	joint sparse spectrum reconstruction
LED	light-emitting diode
LEP	laser-evoked brain potentials
LF	low frequency
LMS	least mean squares
LSE	least squares estimator
MAD	mean absolute deviation
MAE	mean absolute error
mPRH	median of peak rise height
MRI	magnetic resonance imaging
MSE	mean squared error
MVAR	multivariate autoregressive
NLMS	normalized least mean squares
nRMSSD	normalized root mean square of successive differences

NSR	normal sinus rhythm
OLS	ordinary least squares
OLVG	Onze Lieve Vrouwe Gasthuis
PAC	premature atrial contraction
PAT	pulse arrival time
PCA	principal component analysis
PD	photodetector
PDC	partial directed coherence
PEP	pre-ejection period
PPG	photoplethysmographic
PPI	peak-to-peak intervals
PRH	peak rise height
PtiO₂	brain tissue oxygenation level
PTT	pulse transit time
PVC	premature ventricular contraction
PWA	pulse wave analysis
PWV	pulse wave velocity
RBF	radial basis function
RLS	recursive least squares
RMSE	root-mean-squared error

RMSSD	root mean square of successive differences
ROC	receiver operating characteristic
rTV-gPDC	robust time-varying generalized partial directed coherence
SBP	systolic blood pressure
SFS	sequential forward selection
ShE	Shannon entropy
SMR	signal-to-motion artifact ratio
SNR	signal-to-noise ratio
SPG	Signal Processing Group
SpO₂	arterial blood oxygen saturation
SSA	singular spectrum analysis
STD	standard deviation
STFT	short-term Fourier transform
SVD	singular value decomposition
SVM	support vector machine
SVR	support vector regression
SVR-Lin	SVR with linear kernel
SVR-G	SVR with Gaussian kernel
TBI	traumatic brain injury
TROIKA	signal decompositIon for denoising, sparse signal RecOnstructIon for high-resolution spectrum estimation, and spectral peaK trAcking with verification

TU	Technische Universität
TV-gPDC	time-varying generalized partial directed coherence
TVAR	time-varying autoregressive
TVMA	time-varying moving-average
UV	ultraviolet
VAI	vascular age index
Vib	vibration
VLF	very low frequency
VPG	velocity of PPG

List of Symbols

The following list contains the most important symbols in the dissertation in alphabetical order. The remaining symbols are introduced where they are used.

a	characteristic point in the APG signal
$\mathbf{a}(n)$	vector containing the measured non-stationary accelerometer information
b	characteristic point in the APG signal
b_{bias}	bias term
c	characteristic point in the APG signal
c_{tune}	tuning parameter that trades off robustness and efficiency
C	cost of misclassifying
CV_i	i -th type of regression parameter training
d	characteristic point in the APG signal
D	downsampling factor
\in	element of
e	characteristic point in the APG signal
$e(n)$	non-stationary error signal
E_n	signal energy of the n -th heartbeat
f	discrete frequency value
f_c	cut-off frequency
f_s	sampling frequency
$f_{\text{HR}}(n)$	original heart rate
$\hat{f}_{\text{HR}}(n)$	estimated heart rate
$\hat{f}_{\text{HR}}^{\text{pred}}(n)$	estimated predicted heart rate
$\mathcal{F}\{\cdot\}$	Fourier transformation operator
$\mathbf{h}(n, \alpha_{\text{acc}})$	non-stationary impulse response dependent on time and acceleration
$\hat{\mathbf{h}}(n, \alpha_{\text{acc}})$	estimated non-stationary impulse response
$\mathbf{h}(n, \alpha_{\text{acc}}, \omega, \psi)$	non-stationary impulse response dependent on time, acceleration, angular velocity for rotational movements and actual position of the PPG sensor
k	pixel index
$K(\cdot, \cdot)$	kernel function
l	discrete peak value
l_n	number of samples in heartbeat n

$L_{\text{hub}}(\boldsymbol{\beta}, \sigma)$	Huber's criterion
m	discrete segment index
m_n	slope between the n -th and $(n + 1)$ -th systolic notch
$m(n)$	non-stationary motion artifact signal
$\hat{m}(n)$	estimated non-stationary motion artifact signal
M_{seg}	number of segments
$M(\mathbf{x})$	masking operator applied to the vectorized feature matrix \mathbf{x}
$\max\{f(x)\}$	returns the maximal value of $f(x)$
N	number of estimates
N_{beat}	number of heartbeats
N_{bin}	number of normalized histogram bins
N_{diff}	number of adjacent peak differences
N_{feat}	number of features
N_{init}	number of initialization pixels
N_{ppg}	number of samples in the PPG signal
N_{obs}	number of observations (heartbeats)
N_{seg}	number of samples in a segment
N_{var}	number of most variant pixels
n	discrete time index
$\mathcal{O}(\cdot)$	order of the function
$p(n)$	measured PPG signal
$p^i(n)$	i -th measured PPG signal
$p_n(i)$	n -th heartbeat of the PPG signal
\mathbf{p}	vector containing the samples of the PPG signal
$p_m^{\text{seg}}(i)$	i -th sample of the m -th segment of the PPG signal
$\mathbf{p}_m^{\text{seg}}$	vector containing the samples of the m -th segment of the PPG signal
\mathbf{p}_n	vector containing the samples of the n -th heartbeat of the PPG signal
$p'_n(i)$	i -th sample of the first order difference series of the n -th heartbeat of the PPG signal
\mathbf{p}'_n	vector containing the first order difference series of the n -th heartbeat of the PPG signal
$p''_n(i)$	i -th sample of the second order difference series of the n -th heartbeat of the PPG signal
\mathbf{p}''_n	vector containing the second order difference series of the n -th heartbeat of the PPG signal

$P(f_i, m)$	Fourier transform of the vector containing the samples of the m -th segment of the PPG signal
$r_{p_i p_j}(\kappa)$	sample correlation function of $p_i(n)$ and $p_j(n)$
$r_{p_i p_j}^{\text{norm}}(\kappa)$	normalized sample correlation function of $p_i(n)$ and $p_j(n)$
$\mathbf{r}_{p_i p_j}^{\text{norm}}$	vector containing the normalized sample correlation function of $p_i(n)$ and $p_j(n)$
$\text{rank}(\cdot)$	rank of a matrix
$s(n)$	original non-stationary PPG signal without motion artifacts
$\hat{s}(n)$	estimate of the original non-stationary PPG signal without motion artifacts
$\hat{s}_i(n)$	estimate of the i -th original non-stationary PPG signal without motion artifacts
$\hat{S}_i(n, f)$	spectrogram of the i -th estimated original non-stationary PPG signal without motion artifacts
$\hat{S}_{\text{com}}(n, f)$	combined spectrogram of the estimated original non-stationary PPG signal without motion artifacts
$\hat{S}_{\text{sum}}(n, f)$	summed spectrogram of the squared estimated original non-stationary PPG signals without motion artifacts
T	threshold parameter
$v(n)$	sensor and amplifier noise signal
\mathbf{v}	model uncertainty vector
$w_{\text{acc}}(n, f)$	window function of Gaussian bandstop filter to suppress acceleration noise
\mathbf{w}	normal vector to a hyperplane
x_i	i -th feature values
\mathbf{x}_i	vector containing the i -th feature values
\mathbf{x}	vector containing the vectorized standardized feature matrix \mathbf{X}
$\tilde{\mathbf{x}}$	vector containing the successfully extracted features
\mathbf{X}	standardized feature matrix
y_i^{cl}	i -th class label
\hat{y}_i	i -th cardiovascular parameter estimate
y_i^{ref}	reference value of the i -th cardiovascular parameter estimate
\mathbf{y}_i	cardiovascular parameter vector (dependent variables)
α	scaling factor to obtain Fisher consistency
α_j	Lagrangian multiplier
α_{acc}	acceleration that acts on the PPG sensor
β_i	i -th regression parameter

β	vector containing the regression parameters
$\hat{\beta}_{\text{LSE}}$	vector containing parameters estimated by the LSE
δ	practical value for numerical stability
Δ_l	difference of the l -th and $(l+1)$ -th peak location in the PPG signal
$\tilde{\Delta}_i$	peak differences sequence interpolated to a regular grid using an equidistant grid interval
$\tilde{\Delta}$	vector containing the interpolated peak differences sequence $\tilde{\Delta}_i$
$\tilde{\Delta}(f_j)$	Fourier transform of the vector containing the interpolated peak differences $\tilde{\Delta}$
Δf_k	frequency range of $\pm k$ BPM of the preceding heart rate estimate
ε	deviation threshold parameter
μ	step-size of the NLMS filter
ξ_i	slack variable for the i -th feature vector
ρ	Pearson's correlation coefficient
ρ_{hub}	Huber's convex and differentiable loss function
σ_k^2	variance of the non-stationary k -th pixel value $b_k(n)$
σ_K	kernel scale
$\phi(\cdot)$	mapping function
ψ	actual position of the PPG sensor
ω	angular velocity for rotational movements of the PPG sensor

Bibliography

- [1] D. Neitzke. (2018) Statistiken zu Wearables. [Online]. Available: <https://de.statista.com/themen/3471/wearables/>
- [2] M. Elgendi, “On the analysis of fingertip photoplethysmogram signals,” *Current Cardiology Reviews*, vol. 8, no. 1, pp. 14–25, 2012.
- [3] T. Tamura, Y. Maeda, M. Sekine, and M. Yoshida, “Wearable photoplethysmographic sensors – past and present,” *Electronics*, vol. 3, no. 2, pp. 282–302, 2014.
- [4] M. Elgendi, Y. Liang, and R. Ward, “Toward generating more diagnostic features from photoplethysmogram waveforms,” *Diseases*, vol. 6, no. 1, p. 20, 2018.
- [5] J. Allen, “Photoplethysmography and its application in clinical physiological measurement,” *Physiological Measurement*, vol. 28, no. 3, pp. R1–R39, 2007.
- [6] J. G. Webster, *Design of pulse oximeters*. CRC Press, 1997.
- [7] J. Lee, B. A. Reyes, D. D. McManus, O. Mathias, and K. H. Chon, “Atrial fibrillation detection using a smart phone,” in *Proceedings of the 34th Annual International Conference of the IEEE Engineering in Medicine and Biology Society (EMBC)*, Aug./Sep. 2012, pp. 1177–1180.
- [8] D. D. McManus, J. Lee, O. Maitas, N. Esa, R. Pidikiti, A. Carlucci, J. Harrington, E. Mick, and K. H. Chon, “A novel application for the detection of an irregular pulse using an iPhone 4S in patients with atrial fibrillation,” *Heart Rhythm*, vol. 10, no. 3, pp. 315–319, 2013.
- [9] J. W. Chong, N. Esa, D. D. McManus, and K. H. Chon, “Arrhythmia discrimination using a smart phone,” *IEEE Journal of Biomedical and Health Informatics*, vol. 19, no. 3, pp. 815–824, 2015.
- [10] R.-C. Peng, X.-L. Zhou, W.-H. Lin, and Y.-T. Zhang, “Extraction of heart rate variability from smartphone photoplethysmograms,” *Computational and Mathematical Methods in Medicine*, vol. 2015, no. 516826, pp. 1–11, 2015.
- [11] D. D. McManus, J. W. Chong, A. Soni, J. S. Saczynski, N. Esa, C. Napolitano, C. E. Darling, E. Boyer, R. K. Rosen, K. C. Floyd, and K. H. Chon, “Pulse-smart: Pulse-based arrhythmia discrimination using a novel smartphone application,” *Journal of Cardiovascular Electrophysiology*, vol. 27, no. 1, pp. 51–57, 2016.
- [12] Happitech. (2018) Happitech SDK allows for measuring of vitals signs like Heart Rate, Heart Rate Variability using the sensors on your smartphone to detect stress, fitness levels and heart disorders. [Online]. Available: <https://www.happitech.com/>
- [13] R. R. Anderson and J. A. Parrish, “The optics of human skin,” *Journal of Investigative Dermatology*, vol. 77, no. 1, pp. 13–19, 1981.

- [14] J. Lee, K. Matsumura, K. Yamakoshi, P. Rolfe, S. Tanaka, and T. Yamakoshi, "Comparison between red, green and blue light reflection photoplethysmography for heart rate monitoring during motion," in *Proceedings of the 35th Annual International Conference of the IEEE Engineering in Medicine and Biology Society (EMBC)*, July 2013, pp. 1724–1727.
- [15] Z. Zhang, Z. Pi, and B. Liu, "TROIKA: A general framework for heart rate monitoring using wrist-type photoplethysmographic signals during intensive physical exercise," *IEEE Transactions on Biomedical Engineering*, vol. 62, no. 2, pp. 522–531, Feb. 2015.
- [16] T. Schäck, C. Sledz, M. Muma, and A. M. Zoubir, "A new method for heart rate monitoring during physical exercise using photoplethysmographic signals," in *Proceedings of the 23rd European Signal Processing Conference (EUSIPCO)*. IEEE, 2015, pp. 2666–2670.
- [17] T. Schäck, M. Muma, and A. M. Zoubir, "Computationally efficient heart rate estimation during physical exercise using photoplethysmographic signals," in *Proceedings of the 25th European Signal Processing Conference (EUSIPCO)*, Aug 2017, pp. 2478–2481.
- [18] 2010 ICON Health & Fitness. (2018) Cardiodfrequenzimetro Polar T34. [Online]. Available: <https://www.proformfitness.it/cardiodfrequenzimetro-polar-t34.html>
- [19] Garmin Ltd. (2018) vivosmart[®] HR. [Online]. Available: <https://buy.garmin.com/de-DE/DE/p/531166>
- [20] J. Yao and S. Warren, "A short study to assess the potential of independent component analysis for motion artifact separation in wearable pulse oximeter signals," in *Proceedings of the 27th Annual International Conference of the IEEE Engineering in Medicine and Biology Society (EMBC)*, 2005, pp. 3585–3588.
- [21] B. S. Kim and S. K. Yoo, "Motion artifact reduction in photoplethysmography using independent component analysis," *IEEE Transactions on Biomedical Engineering*, vol. 53, no. 3, pp. 566–568, Mar. 2006.
- [22] S. H. Kim, D. W. Ryoo, and C. Bae, "Adaptive noise cancellation using accelerometers for the PPG signal from forehead," in *Proceedings of the 29th Annual International Conference of the IEEE Engineering in Medicine and Biology Society (EMBC)*. IEEE, 2007, pp. 2564–2567.
- [23] L. B. Wood and H. H. Asada, "Noise cancellation model validation for reduced motion artifact wearable PPG sensors using MEMS accelerometers," in *Proceedings of the 28th Annual International Conference of the IEEE Engineering in Medicine and Biology Society (EMBC)*. IEEE, 2006, pp. 3525–3528.
- [24] R. Krishnan, B. Natarajan, and S. Warren, "Two-stage approach for detection and reduction of motion artifacts in photoplethysmographic data," *IEEE Transactions on Biomedical Engineering*, vol. 57, no. 8, pp. 1867–1876, Aug. 2010.

- [25] B. Lee, J. Han, H. J. Baek, J. H. Shin, K. S. Park, and W. J. Yi, "Improved elimination of motion artifacts from a photoplethysmographic signal using a Kalman smoother with simultaneous accelerometry," *Physiological Measurement*, vol. 31, no. 12, pp. 1585–1603, 2010.
- [26] M. R. Ram, K. V. Madhav, E. H. Krishna, K. N. Reddy, and K. A. Reddy, "A novel approach for motion artifact reduction in PPG signals based on AS-LMS adaptive filter," *IEEE Transactions on Instrumentation and Measurement*, vol. 61, no. 5, pp. 1445–1457, May 2012.
- [27] R. Yousefi, M. Nourani, S. Ostadabbas, and I. Panahi, "A motion-tolerant adaptive algorithm for wearable photoplethysmographic biosensors," *IEEE Journal of Biomedical and Health Informatics*, vol. 18, no. 2, pp. 670–681, Mar. 2014.
- [28] M. R. Ram, K. V. Madhav, E. H. Krishna, K. N. Reddy, and K. A. Reddy, "On the performance of AS-LMS based adaptive filter for reduction of motion artifacts from PPG signals," in *Proceedings of the 28th IEEE International Instrumentation and Measurement Technology Conference (I2MTC)*, Binjiang, China, 2011, pp. 1536–1539.
- [29] K.-M. Lam, C. O. S. Sorzano, Z. Zhang, and P. Campisi, "Undergraduate students compete in the IEEE Signal Processing Cup: Part 1 [SP Education]," *IEEE Signal Processing Magazine*, vol. 32, no. 4, pp. 123–125, 2015.
- [30] Z. Zhang, "Undergraduate students compete in the IEEE Signal Processing Cup: Part 3 [SP Education]," *IEEE Signal Processing Magazine*, vol. 32, no. 6, pp. 113–116, 2015.
- [31] —, "Photoplethysmography-based heart rate monitoring in physical activities via joint sparse spectrum reconstruction," *IEEE Transactions on Biomedical Engineering*, vol. 62, no. 8, pp. 1902–1910, 2015.
- [32] E. Khan, F. Al Hossain, S. Z. Uddin, S. K. Alam, and M. K. Hasan, "A robust heart rate monitoring scheme using photoplethysmographic signals corrupted by intense motion artifacts," *IEEE Transactions on Biomedical Engineering*, vol. 63, no. 3, pp. 550–562, 2016.
- [33] Y. Ye, Y. Cheng, W. He, M. Hou, and Z. Zhang, "Combining nonlinear adaptive filtering and signal decomposition for motion artifact removal in wearable photoplethysmography," *IEEE Sensors Journal*, vol. 16, no. 19, pp. 7133–7141, 2016.
- [34] Y. Ye, W. He, Y. Cheng, W. Huang, and Z. Zhang, "A robust random forest-based approach for heart rate monitoring using photoplethysmography signal contaminated by intense motion artifacts," *Sensors*, vol. 17, no. 2, p. 385, 2017.
- [35] V. Periyasamy, M. Pramanik, and P. K. Ghosh, "Review on heart-rate estimation from photoplethysmography and accelerometer signals during physical exercise," *Journal of the Indian Institute of Science*, vol. 97, no. 3, pp. 313–324, 2017.

- [36] R. E. Kalman *et al.*, “A new approach to linear filtering and prediction problems,” *Journal of Basic Engineering*, vol. 82, no. 1, pp. 35–45, 1960.
- [37] E. Hänsler, *Statistische Signale: Grundlagen und Anwendungen*, 3rd ed. Berlin Heidelberg, Germany: Springer, 2001.
- [38] S. Salehizadeh, D. Dao, J. Bolkhovskiy, C. Cho, Y. Mendelson, and K. H. Chon, “A novel time-varying spectral filtering algorithm for reconstruction of motion artifact corrupted heart rate signals during intense physical activities using a wearable photoplethysmogram sensor,” *Sensors*, vol. 16, no. 1, p. 10, 2015.
- [39] J. Xiong, L. Cai, D. Jiang, H. Song, and X. He, “Spectral matrix decomposition-based motion artifacts removal in multi-channel PPG sensor signals.” *IEEE Access*, vol. 4, pp. 3076–3086, 2016.
- [40] A. Temko, “Accurate wearable heart rate monitoring during physical exercises using PPG,” *IEEE Transactions on Biomedical Engineering*, vol. 64, no. 9, pp. 2016–2024, Sept 2017.
- [41] S. F. Cotter, B. D. Rao, K. Engan, and K. Kreutz-Delgado, “Sparse solutions to linear inverse problems with multiple measurement vectors,” *IEEE Transactions on Signal Processing*, vol. 53, no. 7, pp. 2477–2488, 2005.
- [42] Z. Zhang. (2011) Matlab Codes. [Online]. Available: <https://sites.google.com/site/researchbyzhang/software>
- [43] T. Schäck, Y. S. Harb, M. Muma, and A. M. Zoubir, “Computationally efficient algorithm for photoplethysmography-based atrial fibrillation detection using smartphones,” in *Proceedings of the 39th Annual International Conference of the IEEE Engineering in Medicine and Biology Society (EMBC)*, July 2017, pp. 104–108.
- [44] T. Schäck, M. Muma, and A. M. Zoubir, “Estimation of blood pressure, pulse wave velocity and vascular age index from a single photoplethysmographic signal,” *submitted to IEEE Journal of Biomedical and Health Informatics*, October 2018.
- [45] World Health Organization, *World Health Statistics 2015*. World Health Organization, 2015.
- [46] P. Kirchhof, S. Benussi, D. Kotecha, A. Ahlsson, D. Atar, B. Casadei, M. Castella, H. C. Diener, H. Heidbuchel, J. Hendriks *et al.*, “2016 ESC guidelines for the management of atrial fibrillation developed in collaboration with EACTS,” *European Heart Journal*, vol. 37, no. 38, 2016.
- [47] S. S. Chugh, R. Havmoeller, K. Narayanan, D. Singh, M. Rienstra, E. J. Benjamin, R. F. Gillum, Y.-H. Kim, J. H. McAnulty, Z.-J. Zheng, M. H. Forouzanfar, M. Naghavi, G. A. Mensah, M. Ezzati, and C. J. L. Murray, “Worldwide epidemiology of atrial fibrillation: A global burden of disease 2010 study,” *Circulation*, 2013.

- [48] J. Heeringa, D. A. van der Kuip, A. Hofman, J. A. Kors, G. van Herpen, B. H. C. Stricker, T. Stijnen, G. Y. Lip, and J. C. Witteman, "Prevalence, incidence and lifetime risk of atrial fibrillation: the Rotterdam study," *European Heart Journal*, vol. 27, no. 8, pp. 949–953, 2006.
- [49] R. C. Davis, F. R. Hobbs, J. E. Kenkre, A. K. Roalfe, R. Iles, G. Y. Lip, and M. K. Davies, "Prevalence of atrial fibrillation in the general population and in high-risk groups: the ECHOES study," *Europace*, vol. 14, no. 11, pp. 1553–1559, 2012.
- [50] S. Lewington, R. Clarke, N. Qizilbash, R. Peto, R. Collins, and Prospective Studies Collaboration, "Age-specific relevance of usual blood pressure to vascular mortality: a meta-analysis of individual data for one million adults in 61 prospective studies," *The Lancet*, vol. 360, no. 9349, pp. 1903–1913, 2002.
- [51] B. Spronck, M. H. Heusinkveld, F. H. Vanmolkot, J. Op't Roodt, E. Hermeling, T. Delhaas, A. A. Kroon, and K. D. Reesink, "Pressure-dependence of arterial stiffness: potential clinical implications," *Journal of Hypertension*, vol. 33, no. 2, pp. 330–338, 2015.
- [52] R. R. Townsend, "Arterial stiffness: recommendations and standardization," *Pulse*, vol. 4, no. Suppl. 1, pp. 3–7, 2016.
- [53] S. Laurent, J. Cockcroft, L. Van Bortel, P. Boutouyrie, C. Giannattasio, D. Hayoz, B. Pannier, C. Vlachopoulos, I. Wilkinson, and H. Struijker-Boudier, "Expert consensus document on arterial stiffness: methodological issues and clinical applications," *European Heart Journal*, vol. 27, no. 21, pp. 2588–2605, 2006.
- [54] A. Moens, "Die Pulscurve," *EJ Brill: Leiden*, 1878.
- [55] G. Mancia, R. Fagard, K. Narkiewicz, J. Redon, A. Zanchetti, M. Böhm, T. Christiaens, R. Cifkova, G. De Backer *et al.*, "2013 ESH/ESC Guidelines for the management of arterial hypertension: The Task Force for the management of arterial hypertension of the European Society of Hypertension (ESH) and of the European Society of Cardiology (ESC)," *Journal of Hypertension*, vol. 31, no. 7, pp. 1281–1357, 2013.
- [56] P. Nilsson, "Vascular age: How can it be determined? What are its clinical applications?" *Medicographia*, vol. 37, p. 454, 2015.
- [57] E. Jonathan and M. Leahy, "Investigating a smartphone imaging unit for photoplethysmography," *Physiological Measurement*, vol. 31, no. 11, p. N79, 2010.
- [58] D. Grimaldi, Y. Kurylyak, F. Lamonaca, and A. Nastro, "Photoplethysmography detection by smartphone's videocamera," in *Proceedings of the 6th IEEE International Conference on Intelligent Data Acquisition and Advanced Computing Systems: Technology and Applications (IDAACS)*, vol. 1. IEEE, 2011, pp. 488–491.

- [59] C. G. Scully, J. Lee, J. Meyer, A. M. Gorbach, D. Granquist-Fraser, Y. Mendelson, and K. H. Chon, "Physiological parameter monitoring from optical recordings with a mobile phone," *IEEE Transactions on Biomedical Engineering*, vol. 59, no. 2, pp. 303–306, 2012.
- [60] M. Forouzanfar, H. R. Dajani, V. Z. Groza, M. Bolic, S. Rajan, and I. Batkin, "Oscillometric blood pressure estimation: past, present, and future," *IEEE Reviews in Biomedical Engineering*, vol. 8, pp. 44–63, 2015.
- [61] T. Sato, M. Nishinaga, A. Kawamoto, T. Ozawa, and H. Takatsuji, "Accuracy of a continuous blood pressure monitor based on arterial tonometry," *Hypertension*, vol. 21, no. 6, Pt 1, pp. 866–874, 1993.
- [62] K. Wesseling, B. De Wit, G. Van der Hoeven, J. Van Goudoever, and J. Settels, "Physiocal, calibrating finger vascular physiology for Finapres," *Homeostasis*, vol. 36, no. 2–3, pp. 67–82, 1995.
- [63] M. Sharma, K. Barbosa, V. Ho, D. Griggs, T. Ghirmai, S. K. Krishnan, T. K. Hsiai, J.-C. Chiao, and H. Cao, "Cuff-less and continuous blood pressure monitoring: A methodological review," *Technologies*, vol. 5, no. 2, p. 21, 2017.
- [64] D. Buxi, J.-M. Redouté, and M. R. Yuce, "Blood pressure estimation using pulse transit time from bioimpedance and continuous wave radar," *IEEE Transactions on Biomedical Engineering*, vol. 64, no. 4, pp. 917–927, 2017.
- [65] T. Pereira, C. Correia, and J. Cardoso, "Novel methods for pulse wave velocity measurement," *Journal of Medical and Biological Engineering*, vol. 35, no. 5, pp. 555–565, 2015.
- [66] M. W. Rajzer, W. Wojciechowska, M. Klocek, I. Palka, M. Brzozowska-Kiszka, and K. Kawecka-Jaszcz, "Comparison of aortic pulse wave velocity measured by three techniques: Complior, Sphygmocor and Arteriograph," *Journal of Hypertension*, vol. 26, no. 10, pp. 2001–2007, 2008.
- [67] J. Lass, I. Meigas, D. Karai, R. Kattai, J. Kaik, and M. Rossmann, "Continuous blood pressure monitoring during exercise using pulse wave transit time measurement," in *Proceedings of the 26th Annual International Conference of the IEEE Engineering in Medicine and Biology Society (EMBC)*, Sep. 2004, pp. 2239–2242.
- [68] C. Poon and Y. Zhang, "Cuff-less and noninvasive measurements of arterial blood pressure by pulse transit time," in *Proceedings of the 28th Annual International Conference of the IEEE Engineering in Medicine and Biology Society (EMBC)*, Jan. 2006, pp. 5877–5880.
- [69] S. Ahmad, S. Chen, K. Soueidan, I. Batkin, M. Bolic, H. Dajani, and V. Groza, "Electrocardiogram-assisted blood pressure estimation," *IEEE Transactions on Biomedical Engineering*, vol. 59, no. 3, pp. 608–618, 2012.
- [70] D. Buxi, J.-M. Redouté, and M. R. Yuce, "A survey on signals and systems in ambulatory blood pressure monitoring using pulse transit time," *Physiological Measurement*, vol. 36, no. 3, pp. R1–R26, 2015.

- [71] F. Miao, N. Fu, Y.-T. Zhang, X.-R. Ding, X. Hong, Q. He, and Y. Li, “A novel continuous blood pressure estimation approach based on data mining techniques,” *IEEE Journal of Biomedical and Health Informatics*, vol. 21, no. 6, pp. 1730–1740, 2017.
- [72] R. He, Z.-P. Huang, L.-Y. Ji, J.-K. Wu, H. Li, and Z.-Q. Zhang, “Beat-to-beat ambulatory blood pressure estimation based on random forest,” in *Proceedings of the 13th IEEE International Conference on Wearable and Implantable Body Sensor Networks (BNS)*. IEEE, 2016, pp. 194–198.
- [73] X.-R. Ding, Y.-T. Zhang, J. Liu, W.-X. Dai, and H. K. Tsang, “Continuous cuffless blood pressure estimation using pulse transit time and photoplethysmogram intensity ratio,” *IEEE Transactions on Biomedical Engineering*, vol. 63, no. 5, pp. 964–972, 2016.
- [74] V. Chandrasekaran, R. Dantu, S. Jonnada, S. Thiyagaraja, and K. P. Subbu, “Cuffless differential blood pressure estimation using smart phones,” *IEEE Transactions on Biomedical Engineering*, vol. 60, no. 4, pp. 1080–1089, 2013.
- [75] L. Krivoshei, S. Weber, T. Burkard, A. Maseli, N. Brasier, M. Kühne, D. Conen, T. Huebner, A. Seeck, and J. Eckstein, “Smart detection of atrial fibrillation,” *Europace*, p. euw125, 2016.
- [76] G. Ernst, *Heart rate variability*. Springer, 2013.
- [77] W. Karlen, K. Kobayashi, J. Ansermino, and G. Dumont, “Photoplethysmogram signal quality estimation using repeated Gaussian filters and cross-correlation,” *Physiological Measurement*, vol. 33, no. 10, p. 1617, 2012.
- [78] H. Liu and H. Motoda, *Feature selection for knowledge discovery and data mining*. Springer Science & Business Media, 2012, vol. 454.
- [79] I. Steinwart and A. Christmann, *Support vector machines*. Springer Science & Business Media, 2008.
- [80] C.-C. Chang and C.-J. Lin, “LIBSVM: A library for support vector machines,” *ACM Transactions on Intelligent Systems and Technology*, vol. 2, pp. 27:1–27:27, 2011, software available at <http://www.csie.ntu.edu.tw/~cjlin/libsvm>.
- [81] E. J. Candès and B. Recht, “Exact matrix completion via convex optimization,” *Foundations of Computational Mathematics*, vol. 9, no. 6, pp. 717–772, 2009.
- [82] E. J. Candès and S. Becker. (2011) Singular Value Thresholding. [Online]. Available: <http://svt.stanford.edu/code.html>
- [83] Å. Björck, *Numerical methods for least squares problems*. Philadelphia, PA: SIAM, 1996.
- [84] P. J. Huber, *Robust statistics*. John Wiley & Sons, New Jersey, 2009.
- [85] A. M. Zoubir, V. Koivunen, Y. Chakhchoukh, and M. Muma, “Robust estimation in signal processing: A tutorial-style treatment of fundamental concepts,” *IEEE Signal Processing Magazine*, vol. 29, no. 4, pp. 61–80, 2012.

- [86] A. M. Zoubir, V. Koivunen, E. Ollila, and M. Muma, *Robust Statistics for Signal Processing*. Cambridge, U.K.: Cambridge University Press, 2018.
- [87] V. Vapnik, *The nature of statistical learning theory*. Springer Science & Business Media, 2013.
- [88] A. J. Smola and B. Schölkopf, “A tutorial on support vector regression,” *Statistics and Computing*, vol. 14, no. 3, pp. 199–222, 2004.
- [89] F. Strasser, M. Muma, and A. M. Zoubir, “Motion artifact removal in ECG signals using multi-resolution thresholding,” in *Proceedings of the 20th European Signal Processing Conference (EUSIPCO)*, Aug 2012, pp. 899–903.
- [90] J. Pan and W. J. Tompkins, “A real-time QRS detection algorithm,” *IEEE Transactions on Biomedical Engineering*, no. 3, pp. 230–236, 1985.
- [91] H. Sedghamiz. (2014) Matlab Implementation of Pan Tompkins ECG QRS detector. [Online]. Available: <https://www.researchgate.net/publication/313673153>
- [92] C. R. Jones, K. Taylor, P. Chowienczyk, L. Poston, and A. H. Shennan, “A validation of the Mobil-O-Graph (version 12) ambulatory blood pressure monitor,” *Blood Pressure Monitoring*, vol. 5, no. 4, pp. 233–238, 2000.
- [93] W. Wei, M. Tölle, W. Zidek, and M. van der Giet, “Validation of the Mobil-O-Graph: 24 h-blood pressure measurement device,” *Blood Pressure Monitoring*, vol. 15, no. 4, pp. 225–228, 2010.
- [94] IEEE Standards Association, “IEEE Standard for Wearable Cuffless Blood Pressure Measuring Devices,” *IEEE Standard 1708-2014*, pp. 1–38, Aug 2014.
- [95] E. O’Brien and G. S. Stergiou, “The pursuit of accurate blood pressure measurement: A 35-year travail,” *Journal of Clinical Hypertension*, vol. 19, no. 8, pp. 746–752, 2017.
- [96] G. S. Stergiou, B. Alpert, S. Mieke, R. Asmar, N. Atkins, S. Eckert, G. Frick, B. Friedman, T. Graßl, T. Ichikawa *et al.*, “A universal standard for the validation of blood pressure measuring devices: Association for the Advancement of Medical Instrumentation/European Society of Hypertension/International Organization for Standardization (AAMI/ESH/ISO) Collaboration Statement,” *Hypertension*, vol. 36, no. 3, pp. 472–478, March 2018.
- [97] J. P. Kaipio and P. A. Karjalainen, “Estimation of event-related synchronization changes by a new TVAR method,” *IEEE Transactions on Biomedical Engineering*, vol. 44, no. 8, pp. 649–656, Aug 1997.
- [98] L. A. Baccalá, K. Sameshima, G. Ballester, A. Do Valle, and C. Timo-Iaria, “Studying the interaction between brain structures via directed coherence and Granger causality,” *Applied Signal Processing*, vol. 5, no. 1, pp. 40–48, 1998.

- [99] J. R. Sato, D. Y. Takahashi, S. M. Arcuri, K. Sameshima, P. A. Morettin, and L. A. Baccalá, “Frequency domain connectivity identification: An application of partial directed coherence in fMRI,” *Human Brain Mapping*, vol. 30, no. 2, pp. 452–461, 2009.
- [100] Z. G. Zhang, Y. S. Hung, and S. C. Chan, “Local polynomial modeling of time-varying autoregressive models with application to time-frequency analysis of event-related EEG,” *IEEE Transactions on Biomedical Engineering*, vol. 58, no. 3, pp. 557–566, March 2011.
- [101] G. Varotto, E. Visani, L. Canafoglia, S. Franceschetti, G. Avanzini, and F. Panzica, “Enhanced frontocentral EEG connectivity in photosensitive generalized epilepsies: A partial directed coherence study,” *Epilepsia*, vol. 53, no. 2, pp. 359–367, 2012.
- [102] M. Orini, P. Laguna, L. T. Mainardi, and R. Bailón, “Assessment of the dynamic interactions between heart rate and arterial pressure by the cross time-frequency analysis,” *Physiological Measurement*, vol. 33, no. 3, pp. 315–331, 2012.
- [103] M. Orini, R. Bailón, P. Laguna, L. T. Mainardi, and R. Barbieri, “A multivariate time-frequency method to characterize the influence of respiration over heart period and arterial pressure,” *EURASIP Journal on Advances in Signal Processing*, vol. 2012, no. 1, pp. 1–17, 2012.
- [104] M. D. Peláez-Coca, M. Orini, J. Lázaro, R. Bailón, and E. Gil, “Cross time-frequency analysis for combining information of several sources: Application to estimation of spontaneous respiratory rate from photoplethysmography,” *Computational and Mathematical Methods in Medicine*, vol. 2013, 2013.
- [105] B. Boashash, G. Azemi, and J. M. O’Toole, “Time-frequency processing of non-stationary signals: Advanced TFD design to aid diagnosis with highlights from medical applications,” *IEEE Signal Processing Magazine*, vol. 30, no. 6, pp. 108–119, Nov 2013.
- [106] Y. Höller, A. Thomschewski, J. Bergmann, M. Kronbichler, J. S. Crone, E. V. Schmid, K. Butz, P. Höller, R. Nardone, and E. Trinka, “Connectivity biomarkers can differentiate patients with different levels of consciousness,” *Clinical Neurophysiology*, vol. 125, no. 8, pp. 1545–1555, 2014.
- [107] L. Faes, A. Porta, R. Cucino, S. Cerutti, R. Antolini, and G. Nollo, “Causal transfer function analysis to describe closed loop interactions between cardiovascular and cardiorespiratory variability signals,” *Biological Cybernetics*, vol. 90, no. 6, pp. 390–399, 2004.
- [108] L. Faes, L. Widesott, M. Del Greco, R. Antolini, and G. Nollo, “Causal cross-spectral analysis of heart rate and blood pressure variability for describing the impairment of the cardiovascular control in neurally mediated syncope,” *IEEE Transactions on Biomedical Engineering*, vol. 53, no. 1, pp. 65–73, Jan. 2006.

- [109] L. Faes and G. Nollo, "Extended causal modeling to assess partial directed coherence in multiple time series with significant instantaneous interactions," *Biological Cybernetics*, vol. 103, no. 5, pp. 387–400, 2010.
- [110] L. Faes, S. Erla, and G. Nollo, "Measuring connectivity in linear multivariate processes: Definitions, interpretation, and practical analysis," *Computational and Mathematical Methods in Medicine*, vol. 2012, p. 140513, 2012.
- [111] M. Orini, R. Bailón, L. T. Mainardi, P. Laguna, and P. Flandrin, "Characterization of dynamic interactions between cardiovascular signals by time-frequency coherence," *IEEE Transactions on Biomedical Engineering*, vol. 59, no. 3, pp. 663–673, 2012.
- [112] T. Schäck, M. Muma, M. Feng, C. Guan, and A. M. Zoubir, "Robust nonlinear causality analysis of nonstationary multivariate physiological time series," *IEEE Transactions on Biomedical Engineering*, vol. 65, no. 6, pp. 1213–1225, June 2018.
- [113] G. C. Carter, "Coherence and time delay estimation," *Proceedings of the IEEE*, vol. 75, no. 2, pp. 236–255, Feb. 1987.
- [114] J. S. Bendat and A. G. Piersol, *Random data: Analysis and measurement procedures*. John Wiley & Sons, 2011, vol. 729.
- [115] M. Muma, D. R. Iskander, and M. J. Collins, "The role of cardiopulmonary signals in the dynamics of the eye's wavefront aberrations," *IEEE Transactions on Biomedical Engineering*, vol. 57, no. 2, pp. 373–383, Feb. 2010.
- [116] M. Kaminski and K. Blinowska, "A new method of the description of the information flow in the brain structures," *Biological Cybernetics*, vol. 65, no. 3, pp. 203–210, 1991.
- [117] Y. Saito and H. Harashima, "Tracking of information within multichannel EEG record: Causal analysis in EEG," in *Recent Advances in EEG and EMG Data Processing*, N. Yamaguchi and K. Fujisawa, Eds. New York: Elsevier, 1981, pp. 133–146.
- [118] L. A. Baccalá and K. Sameshima, "Partial directed coherence: A new concept in neural structure determination," *Biological Cybernetics*, vol. 84, no. 6, pp. 463–474, 2001.
- [119] L. A. Baccalá, K. Sameshima, and D. Y. Takahashi, "Generalized partial directed coherence," in *Proceedings of the 15th International Conference on Digital Signal Processing (ICDSP)*, 2007, pp. 163–166.
- [120] T. Milde, L. Leistritz, L. Astolfi, W. H. Miltner, T. Weiss, F. Babiloni, and H. Witte, "A new kalman filter approach for the estimation of high-dimensional time-variant multivariate AR models and its application in analysis of laser-evoked brain potentials," *Neuroimage*, vol. 50, no. 3, pp. 960–969, 2010.

- [121] L. Leistriz, B. Pester, A. Doering, K. Schiecke, F. Babiloni, L. Astolfi, and H. Witte, “Time-variant partial directed coherence for analysing connectivity: A methodological study,” *Philosophical Transactions of the Royal Society A*, vol. 371, no. 1997, 2013.
- [122] L. A. Baccalá, C. S. N. de Brito, D. Y. Takahashi, and K. Sameshima, “Unified asymptotic theory for all partial directed coherence forms,” *Philosophical Transactions of the Royal Society A*, vol. 371, no. 1997, 2013.
- [123] A. Omidvarnia, G. Azemi, B. Boashash, J. M. O’Toole, P. B. Colditz, and S. Vanhatalo, “Measuring time-varying information flow in scalp EEG signals: Orthogonalized partial directed coherence,” *IEEE Transactions on Biomedical Engineering*, vol. 61, no. 3, pp. 680–693, 2014.
- [124] C. W. J. Granger, “Investigating causal relations by econometric models and cross-spectral methods,” *Econometrica*, vol. 37, pp. 424–438, 1969.
- [125] E. Möller, B. Schack, N. Vath, and H. Witte, “Fitting of one ARMA model to multiple trials increases the time resolution of instantaneous coherence,” *Biological Cybernetics*, vol. 89, no. 4, pp. 303–312, 2003.
- [126] G. A. Giannakakis and K. S. Nikita, “Estimation of time-varying causal connectivity on EEG signals with the use of adaptive autoregressive parameters,” in *Proceedings of the 30th Annual International Conference of the IEEE Engineering in Medicine and Biology Society (EMBC)*, 2008, pp. 3512–3515.
- [127] S. Heritier, E. Cantoni, S. Copt, and M.-P. Victoria-Feser, *Robust Methods in Biostatistics*, D. J. Balding, N. A. C. Cressie, G. M. Fitzmarice, I. M. Johnstone, G. Molengerghs, D. W. Scott, A. F. M. Smitz, R. S. Tsay, S. Weisenberg, and H. Goldstein, Eds. Wiley, 2009.
- [128] P. van Mierlo, E. Carrette, H. Hallez, K. Vonck, D. Van Roost, P. Boon, and S. Staelens, “Accurate epileptogenic focus localization through time-variant functional connectivity analysis of intracranial electroencephalographic signals,” *Neuroimage*, vol. 56, no. 3, pp. 1122–1133, 2011.
- [129] L. Faes, A. Porta, and G. Nollo, “Testing frequency domain causality in multivariate time series,” *IEEE Transactions on Biomedical Engineering*, vol. 57, no. 8, pp. 1897–1906, Aug. 2010.
- [130] N. Nicolaou, S. Hourris, P. Alexandrou, and J. Georgiou, “EEG-based automatic classification of ‘awake’ versus ‘anesthetized’ state in general anesthesia using Granger causality,” *PLoS ONE*, vol. 7, no. 3, p. e33869, Mar. 2012.
- [131] S. L. Bressler and A. K. Seth, “Wiener–Granger causality: A well established methodology,” *Neuroimage*, vol. 58, no. 2, pp. 323–329, 2011.
- [132] E. Pereda, R. Q. Quiroga, and J. Bhattacharya, “Nonlinear multivariate analysis of neurophysiological signals,” *Progress in Neurobiology*, vol. 77, no. 1, pp. 1–37, 2005.

- [133] D. Marinazzo, W. Liao, H. Chen, and S. Stramaglia, “Nonlinear connectivity by Granger causality,” *Neuroimage*, vol. 58, no. 2, pp. 330–338, 2011.
- [134] F. He, S. A. Billings, H.-L. Wei, and P. G. Sarrigiannis, “A nonlinear causality measure in the frequency domain: Nonlinear partial directed coherence with applications to EEG,” *Journal of Neuroscience Methods*, vol. 225, pp. 71–80, 2014.
- [135] P. J. Huber and E. Ronchetti, *Robust Statistics*, 2nd ed. New York, NY, USA: Wiley, 2009.
- [136] R. A. Maronna, D. R. Martin, and V. J. Yohai, *Robust Statistics: Theory and Methods*, ser. Wiley Series in Probability and Statistics. Hoboken, NJ: Wiley, 2006.
- [137] F. Chowdhury, “Input-output modeling of nonlinear systems with time-varying linear models,” *IEEE Transactions on Automatic Control*, vol. 45, no. 7, pp. 1355–1358, Jul. 2000.
- [138] A. Omidvarnia, M. Mesbah, M. Khelif, J. O’Toole, P. Colditz, and B. Boashash, “Kalman filter-based time-varying cortical connectivity analysis of newborn EEG,” in *Proceedings of the 33rd Annual International Conference of the IEEE Engineering in Medicine and Biology Society (EMBC)*, 2011, pp. 1423–1426.
- [139] A. Reynolds, *Corneal topography: measuring and modifying the cornea*, D. Schanzlin and J. Robin, Eds. New York: Springer, 1992.
- [140] W. Alkhalidi, D. R. Iskander, A. M. Zoubir, and M. J. Collins, “Enhancing the standard operating range of a placido disk videokeratoscope for corneal surface estimation,” *IEEE Transactions on Biomedical Engineering*, vol. 56, no. 3, pp. 800–809, March 2009.
- [141] W. Alkhalidi, D. R. Iskander, and A. M. Zoubir, “Model-order selection in zernike polynomial expansion of corneal surfaces using the efficient detection criterion,” *IEEE Transactions on Biomedical Engineering*, vol. 57, no. 10, pp. 2429–2437, Oct 2010.
- [142] W. Alkhalidi, “Statistical signal and image processing techniques in corneal modeling,” Ph.D. dissertation, Technische Universität Darmstadt, Germany, 2010.
- [143] M. Muma and A. M. Zoubir, “Robust model order selection for corneal height data based on τ estimation,” in *Proceedings of the 36th IEEE International Conference on Acoustics, Speech and Signal Processing (ICASSP)*, 2011, pp. 4096–4099.
- [144] D. R. Iskander, M. Collins, and B. Davis, “Evaluating tear film stability in the human eye with high-speed videokeratoscopy,” *IEEE Transactions on Biomedical Engineering*, vol. 52, no. 11, pp. 1939–1949, Nov 2005.
- [145] D. Alonso-Caneiro, J. Turuwhenua, D. R. Iskander, and M. J. Collins, “Diagnosing dry eye with dynamic-area high-speed videokeratoscopy,” *Journal of Biomedical Optics*, vol. 16, no. 7, p. 076012, 2011.

- [146] D. H. Szczesna-Iskander and D. R. Iskander, "Future directions in non-invasive measurements of tear film surface kinetics," *Optometry and Vision Science*, vol. 89, no. 5, pp. 749–759, 2012.
- [147] D. H. Szczesna-Iskander, D. Alonso-Caneiro, and D. R. Iskander, "Objective measures of pre-lens tear film dynamics versus visual responses," *Optometry and Vision Science*, May 2016.
- [148] D. R. Iskander and M. Collins, "Applications of high-speed videokeratoscopy," *Clinical and Experimental Optometry*, vol. 88, no. 4, pp. 223–231, Jul 2005.
- [149] M. Muma, "Robust estimation and model order selection for signal processing," Ph.D. dissertation, Technische Universität Darmstadt, Germany, January 2014.
- [150] J. Nemeth, B. Erdelyi, B. Csakany, P. Gaspar, A. Soumelidis, F. Kahlesz, and Z. Lang, "High-speed videotopographic measurement of tear film build-up time," *Investigative Ophthalmology and Visual Science*, vol. 43, no. 6, pp. 1783–1790, Jun 2002.
- [151] Y. K. Jang, B. J. Kang, and K. R. Park, "A study on eyelid localization considering image focus for iris recognition," *Pattern Recognition Letters*, vol. 29, no. 11, pp. 1698–1704, Aug 2008.
- [152] X. Liu, P. Li, and Q. Song, "Eyelid localization in iris images captured in less constrained environment," in *Proceedings of the 3rd International Conference on Advances in Biometrics (ICB '09)*, ser. Lectures Notes in Computer Science, vol. 5558, Alghero, Italy, June 2009, pp. 1140–1149.
- [153] M. J. Aligholizadeh, S. H. Javadi, R. Sabbaghi-Nadooshan, and K. Kangarloo, "An effective method for eyelashes segmentation using wavelet transform," in *Proceedings of the International Conference on Biometrics and Kansei Engineering (ICBAKE)*, Sep 2011, pp. 185–188.
- [154] F. Bernard, C. E. Deuter, P. Gemmar, and H. Schachinger, "Eyelid contour detection and tracking for startle research related eye-blink measurements from high-speed video records," *Computer Methods and Programs in Biomedicine*, vol. 112, no. 1, pp. 22–37, 2013.
- [155] J. F. Canny, "A computational approach to edge detection," *IEEE Transactions on Pattern Analysis and Machine Intelligence*, vol. 8, no. 6, pp. 679–698, Nov 1986.
- [156] G. Sicuranza, *Nonlinear image processing*, G. Sicuranza and S. Mitra, Eds. San Diego, USA: Academic Press, 2000.
- [157] G. C. Orsak and D. M. Etter, "Collaborative SP education using the internet and Matlab," *IEEE Signal Processing Magazine*, vol. 12, no. 6, pp. 23–32, 1995.
- [158] D. M. Etter, G. C. Orsak, and D. H. Johnson, "Distance teaming experiments in undergraduate DSP," in *Proceedings of the 21st IEEE International Conference on Acoustics, Speech and Signal Processing (ICASSP)*, vol. 2. IEEE, 1996, pp. 1109–1112.

- [159] J. H. McClellan, R. W. Shafer, and M. A. Yoder, *DSP first: A multimedia approach*. Prentice Hall PTR, 1997.
- [160] J. E. Greenberg, B. Delgutte, and M. L. Gray, “Hands-on learning in biomedical signal processing,” *IEEE Engineering in Medicine and Biology Magazine*, vol. 22, no. 4, pp. 71–79, 2003.
- [161] H.-T. Wu, P.-C. Hsu, C.-Y. Lee, H.-J. Wang, and C.-K. Sun, “The impact of supplementary hands-on practice on learning in introductory computer science course for freshmen,” *Computers & Education*, vol. 70, pp. 1–8, 2014.

Curriculum Vitae

Name: Tim Schäck
Date of birth: 19.11.1986
Place of birth: Offenbach am Main, Germany
Family status: single

Education

08/2010 - 05/2011 Study abroad in Electrical and Computer Engineering
University of Illinois at Urbana-Champaign, USA

10/2006 - 03/2013 Diplom-Ingenieur (Dipl.-Ing.)
Electrical Engineering and Information Technology
Technische Universität Darmstadt, Germany

Diploma Thesis (Diplomarbeit):
“Parameter Estimation for Psychophysiological Signals
in Presence of Artifacts”

08/1997 - 06/2006 High School Degree (Abitur)
Adolf-Reichwein-Gymnasium, Heusenstamm, Germany

Work experience

05/2013 - 05/2018 Research Associate
Signal Processing Group
Technische Universität Darmstadt, Germany

03/2012 - 06/2012 Professional Internship
Robert Bosch GmbH, Hildesheim, Germany

08/2011 - 09/2011 Professional Internship
Siemens Audiologische Technik, Erlangen, Germany

Erklärungen laut Promotionsordnung

§8 Abs. 1 lit. c PromO

Ich versichere hiermit, dass die elektronische Version meiner Dissertation mit der schriftlichen Version übereinstimmt.

§8 Abs. 1 lit. d PromO

Ich versichere hiermit, dass zu einem vorherigen Zeitpunkt noch keine Promotion versucht wurde. In diesem Fall sind nähere Angaben über Zeitpunkt, Hochschule, Dissertationsthema und Ergebnis dieses Versuchs mitzuteilen.

§9 Abs. 1 PromO

Ich versichere hiermit, dass die vorliegende Dissertation selbstständig und nur unter Verwendung der angegebenen Quellen verfasst wurde.

§9 Abs. 2 PromO

Die Arbeit hat bisher noch nicht zu Prüfungszwecken gedient.

Datum und Unterschrift

